Title
Building Chemical Architectures for a Better Future

Author
Lee, Chain

Publication Date
2016

Peer reviewed|Thesis/dissertation

UNIVERSITY OF CALIFORNIA

Los Angeles

Building Chemical Architectures for a Better Future:

Synthesis, Applications, and Control of Covalent Triazine Frameworks for Gas Storage, Thin Film Devices, and Electrochemistry

A dissertation submitted in partial satisfaction of the requirements for the degree Doctor of Philosophy in Chemistry

by

Chain Lee

2016

ABSTRACT OF DISSERTATION

Building Chemical Architectures for a Better Future:

Synthesis, Applications, and Control of Covalent Triazine Frameworks

for Gas Storage, Thin Film Devices, and Electrochemistry

by

Chain Lee

Doctor of Philosophy in Chemistry

University of California, Los Angeles 2016

Professor Xiangfeng Duan, Chair

Covalent Triazine Frameworks (CTFs) are highly porous materials with two-dimensional or three-dimensional architectures, which can be synthesized with tunable porosity and a variety of functionalities. Their synthesis and characterization has been studied extensively in many prior works. However, ionic functionalities built into CTFs are new and have not been investigated, especially those containing an imidazolium ring and capable of being deprotonated into an active N-heterocyclic carbene. Chapter 1 introduces different chemical architectures developed by chemists, highlighting one of the most investigated topics being Covalent Organic Frameworks. The theory of absorption of gases on porous solids is also discussed. Chapter 2 outlines the detailed synthesis and characterization of a unique CTF with Reuleaux Triangle shaped pores, which forms by harnessing the geometry of the N-heterocyclic carbene. Aside from nitrogen uptake, we studied absorption of carbon dioxide on an ionically charged framework. Chapter 3 illustrates a method of exfoliating two-dimensional CTFs. Most

CTFs are two dimensionally stacked, which have full conjugation, and π-π stacking similar to that of graphite. Yet, their thin film characteristics have never been studied. Here we developed a method to peel these stacked layers apart, characterize the sheets, and produced thin-film devices along with conductivity measurements. Due to CTFs exceptional stability, and intrinsic nitrogen doping, their electrochemical applications are just beginning to be explored. The electrochemical reduction of oxygen, a very important reaction, is one of the main limiting factors to widespread use of fuel cells. In Chapter 4 we create oxygen reduction catalysts using super-acid derived CTF polymers and cobalt salts as precursors. The CTF polymers readily absorb cobalt from solution and are then annealed at 900 °C. The resultant porous catalyst reduces oxygen to water with performance comparable to the industrial standard platinum. Chapter 5 discusses molecular control of porous carbons. We have developed a new pathway by designing molecular precursors to tune the porosity of CTF-derived porous carbon materials. Using CTFs as precursors, while controlling their monomeric length results in a high degree of pore size control. In this process, by choosing using different ratios of long and short monomers we can be tune the size of the CTFs. The resultant framework is heated to desired temperatures of 700 to 900 °C to yield porous carbon materials. The incremental pore size and volumes from molecular tuning these frameworks remains consistent from both pre annealing to post annealing, though some pore expansions can exist. This is the first demonstration of molecular tuning the pore size of porous carbons, and a powerful way of bringing a certain degree of order to traditionally disordered carbon materials. We apply these characteristics of molecular tuning to investigate capacitive related performance as well as oxygen reduction reaction. Through pore tuning, we create

different porous carbons with surface areas ranging from 450 m^2 g^{-1} all the way to 2400 m^2 g^{-1} while controlling pore sizes within a few nanometers of each other. Capacitive values rise over ten fold from 14 F g^{-1} to 180 F g^{-1}. When different size frameworks are loaded with cobalt and used for oxygen reduction, we observe five-fold increases in kinetic current density, and reach overpotentials of 38 mV less than that of platinum on carbon. These electrocatalysis experiments demonstrate the significance of ample reactant delivery to the catalyst.

The dissertation of Chain Lee is approved.

Jennifer M. Murphy

Richard B. Kaner

Xiangfeng Duan, Committee Chair

University of California, Los Angeles

2016

TABLE OF CONTENTS

LIST OF FIGURES

Figure 5.14 Additional molecular tuning pore size measurements using DFT calculations from BET measurements.

LIST OF TABLES

LIST OF SCHEMES

ACKNOWLEDGEMENTS

First and foremost this dissertation would not be possible without the guidance, support, and radical candor of Professor Xiangfeng Duan. Your insatiable appetite towards perfection drives us students to grow and develop far beyond our known limits. You've forced me to push past my comfort zones and develop into the person I am today. The honest criticism was always harsh tasting medicine, but certainly the patient (me) certainly needed it. Looking back a great deal of important life lessons I have been learned while being in your lab.

I must also acknowledge all Duan and Huang group members, past and present, which have generously shared their knowledge and time. To name a few in no particular order: Zhaoyang Lin, Mengning Ding, Gongming Wang, Zipeng Zhao, Johnathan Shaw, Udayabugya Halim, Ben Papandrea, Hailong Zhou, Lingyan Ruan, Yu Chen, Huilong Fei, Yongjia Li, Dan Bauman, Xu Xu, Yiliu Wang Hyeseung December Eun. You've all helped me graciously, especially those in the beginning when I needed it the most.

I'd like to also acknowledge Professor Richard B. Kaner for being on my committee and allowing my usage of many of his labs resources, as well as the many members of the Kaner group. To Michael 'Saint Tyrone' Yeung, none of my CTF syntheses would ever be possible have you not been there to loan me your blowtorch and the countless quartz tubes throughout the years. Moreover, for the endless advice and selflessness you've given me I am indebted to you. I'd also like to thank Brian McVerry for the collaborative work, experiences and knowledge.

My beginning as a scientist would not have been possible with the initial investment made by my undergraduate advisor Professor Omar M. Yaghi and my

graduate student mentor David K. Britt. I was handed the opportunity of a lifetime to work in MOF chemistry as an undergrad, alongside David who is one of the most influential people of my lifetime. Moreover, while at the group, many members also instilled me with great knowledge. Hiroyasu Furukawa, the adsorption theory you gave me on our many late night discussions I use until this day. Prof. Fernando Uribe-Romo, and Prof. Qiaowei Li donated endless advice and time.

A portion of ability to cope with the struggles of graduate school came from observing the mental fortitude of Dr. Selma Galeb Duhovic. You never give up seagull, and I wish you all the best.

To Dr. Tetsuo Otsuki, and the Occidental College Summer program, whom taught gave me my first experience with organic chemistry, I give great thanks. Dr. O may you rest in peace.

Most of all I would like to thank my parents who always believed in me. Throughout my entire life they have been my support foundation, and even in my hardest times they never lost faith.

Vita

Education

2005-2009	B.S. Biochemistry University of California, Los Angeles
2007-2009	Research Assistant, Yaghi Lab University of California, Los Angeles
2009-2010	Production Chemist, Materia Inc Pasadena, California
2011-2016	Teaching Assistant University of California, Los Angeles
2011-2016	Research Assistant, Duan Lab University of California, Los Angeles

Publications and Presentations

"Enhancing Pore Performance of Cobalt-Catalyzed Oxygen Reduction by Molecular Tuning of Covalent Triazine Frameworks" **Chain Lee**, Xiangfeng Duan, MOF 2016 5th annual conference, Long Beach, California, September 11-15 2016.

"A rational biomimetic approach to structure defect generation in colloidal nanocrystals" Ruan, L.; Ramezani-Dakhel, H.; **Lee, C**.; Li, Y.; Duan, X.; Heinz, H.; Huang, Y. *ACS Nano* **2014**, *8* (7), 6934.

"High Surface Area Tunnels in Hexagonal WO3" Sun, W.; Yeung, M. T.; Lech, A. T.; Lin, C. W.; **Lee, C**.; Li, T.; Duan, X.; Zhou, J.; Kaner, R. B. *Nano Lett*. **2015**.

"Mechanically Shaped 2-Dimensional Covalent Organic Frameworks Reveal Crystallographic Alignment and Fast Li-Ion Conductivity " Vazquez-Molina, D. A.; Mohammad-Pour, G. S.; **Lee, C**.; Logan, M. W.; Duan, X.; Harper, J. K.; Uribe-Romo, F. J. *J. Am. Chem. Soc*. **2016**, *138* (31), 9767.

"Solution Processable Holey Graphene Oxide and Its Derived Macrostructures for High-Performance Supercapacitors" Xu, Y.; Chen, C.-Y.; Zhao, Z.; Lin, Z.; **Lee, C**.; Xu, X.; Wang, C.; Huang, Y.; Shakir, M. I.; Duan, X. *Nano Lett*. **2015**, *15* (7), 4605.

"Synthesis of Stable Shape-Controlled Catalytically Active β-Palladium Hydride" Zhao, Z.; Huang, X.; Li, M.; Wang, G.; **Lee, C**.; Zhu, E.; Duan, X.; Huang, Y. *J. Am. Chem. Soc*. **2015**, *137* (50), 15672.

"Metal insertion in a microporous metal-organic framework lined with 2,2-bipyridine" Bloch, E. D.; Britt, D.; **Lee, C**.; Doonan, C. J.; Uribe-Romo, F. J.; Furukawa, H.; Long, J. R.; Yaghi, O. M. *J. Am. Chem. Soc*. **2010**, *132* (41), 14382.

"Ring-opening reactions within porous metal-organic frameworks" Britt, D.; **Lee, C**.; Uribe-Romo, F. J.; Furukawa, H.; Yaghi, O. M. *Inorg. Chem*. **2010**, *49* (14), 6387.

"Novel epoxide formation in the reaction of 2-bromo-3-methyl-1,4-naphthoquinone with 1,3-propanedithiol" Lam, T. M.; **Lee, C**.; Katardjieff, K.; Otsuki, T. *Bioorg. Med. Chem. Lett*. **2010**, *20* (24), 7226.

Chapter 1

Introduction

1.1 Different Chemical Architectures

Mother nature assembles complex structures and organisms with precision to the atomic level. Chemists have taken these beautiful constructions into inspiration to not just mimic but further advance these architectures by building materials from zero dimensional (0D) to 1D, 2D, and 3D outlined in Figure 1.1. Of these elaborate materials, open frameworks such as Metal Organic Frameworks (MOFs) and Covalent Organic Frameworks (COFs) have received tremendous interest since they combine features of high surface area, chemical functionality, pore tunablity, and crystalline order. This discovery was very different, since many porous materials such are carbons and zeolites lack a high degree of order.

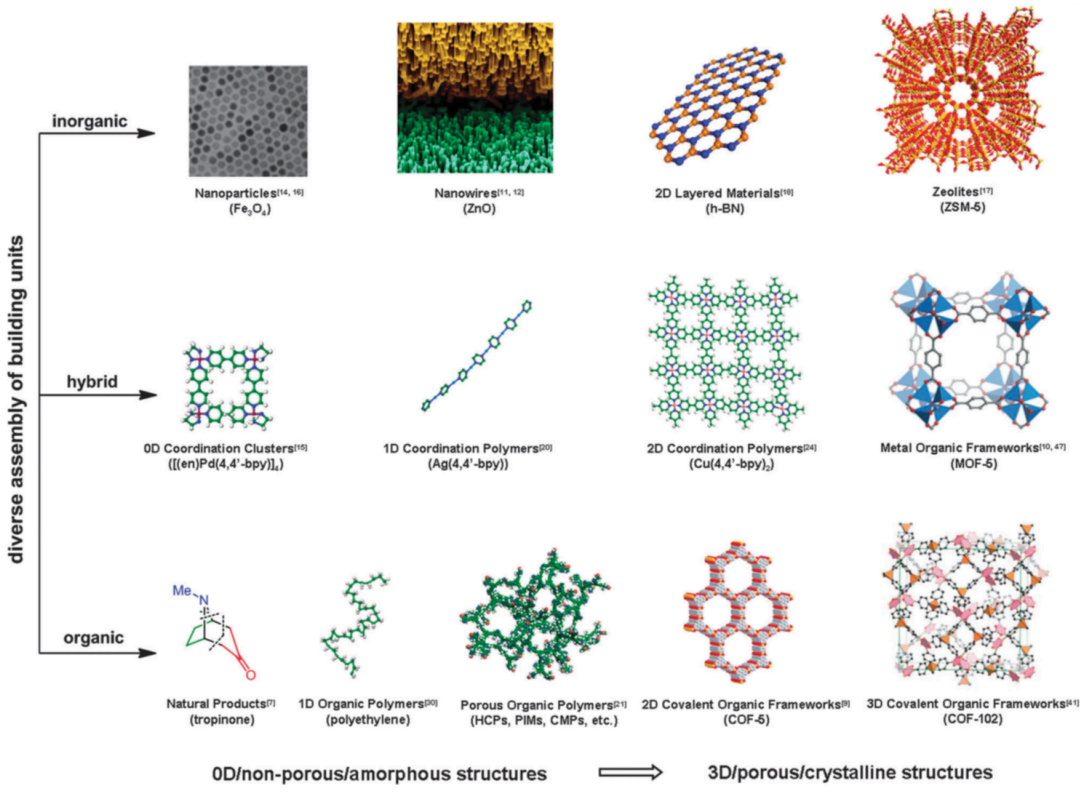

Figure 1.1. Diverse examples of the different architectures chemist can build from 0D all the way to 3D materials with either crystalline, quasi-cyrstalline, or amorphous order[1].

1.2 The development of MOFs and COFs

MOFs are generally assembled through coordination of organic ligands and metal clusters. They differ from coordination polymers, in that their construction intends to produce pores, which can be evacuated[2]. In pursuit of highly stable materials, a long standing strategy for building molecular assemblies come from utilizing covalent organic bonding throughout the structure in what are called Covalent Organic Frameworks (COFs), discovered by Yaghi et al 2005[3]. COFs take full advantage of the directionality and geometry from which covalent bonds build into extensive ordered structure. The use of fully organic linkers and struts omits the need for metal cluster linkages, possibly making the overall weight of the material lighter. Moreover, the types of covalent bonds are important. Generally slightly reversible covalent bonds are employed to help facilitate the crystalline COF structures because they are 'self-correcting from thermodynamically unstable products[4]. The types of bonding can be visualized in Figure 1.2. They range from the homo dehydration of boronic acid or with catechols to form boranate esters as shown in reactions A and B. Silanol can be incorporated as a bonding element along with boronic acids in reaction C. Cyclotrimerization, where three nitrile groups are form a triazine ring are a very new a unique method for creating strong bonds. Imine and hydrozone bondings have also been exploited as shown in reactions E and F.

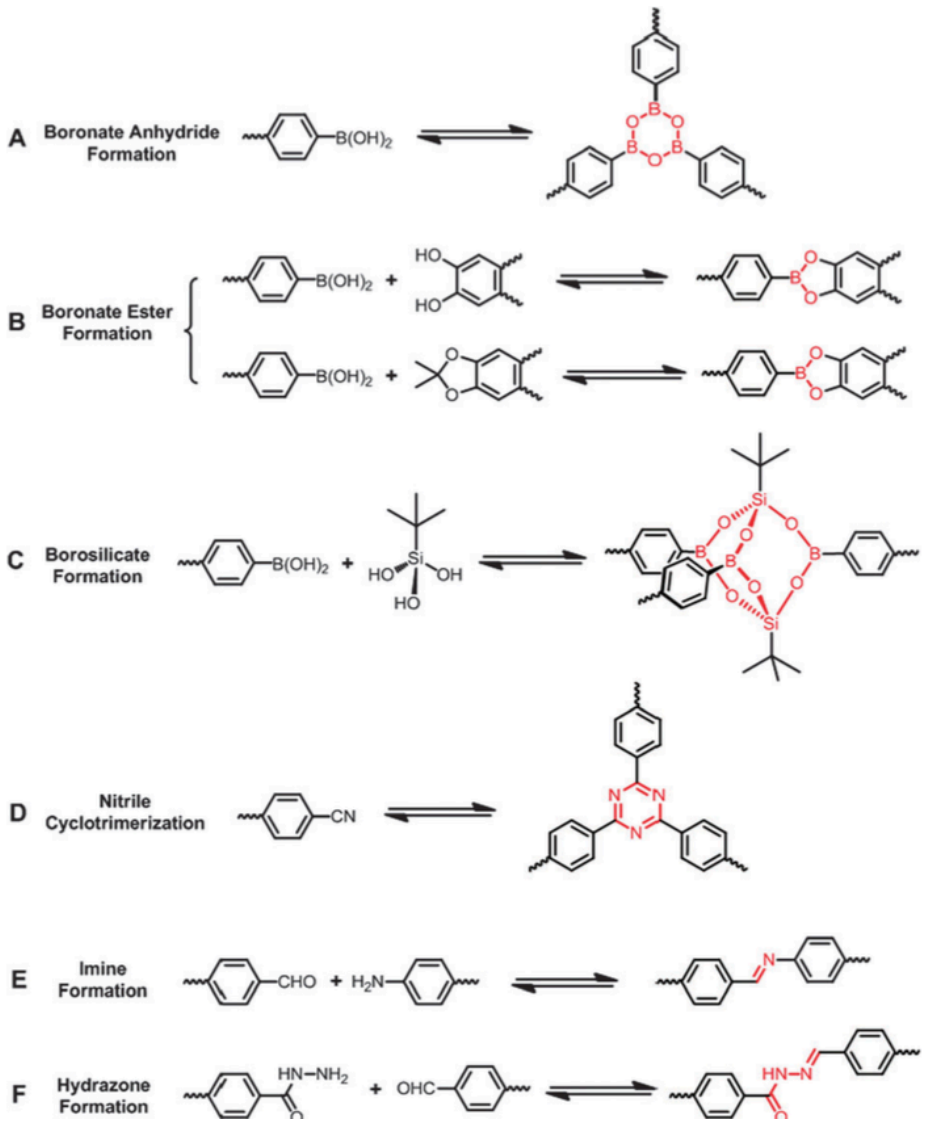

Figure 1.2. The different reversible bonding that has produced successful COF syntheses. The bond formations are highlighted in red.[1]

1.3 The Trimerization of Nitriles

Of the many coordinations and different molecular bonds that can be formed, the triazine ring formation from nitriles (Figure 1.2D reaction D) is particularly interesting for many. This in impart because triazine rings are exceptionally robust to both caustic and highly acidic conditions, unlike many other bonding moieties. In 2008, Kuhn et al.

took 1,4-dicyanobenzene, while using molten zinc chloride ($ZnCl_2$) as both solvent and catalyst[5]. The reaction produced the first Covalent Triazine Framework (CTF), a type of COF, in which a multiple benzene rings and triazine rings were linked together in a two dimensional (2D) fashion, stacked in an eclipsed AAA style just like graphite. The first CTF structure is analogous to the original COFs synthesized by Yaghi et al 2005. Moreover, they contain ordered 1D pores which go through the basal plane of the sheet like material. The ring formation could be tracked with IR spectroscopy and furthermore its crystalline structure using power X-Ray diffraction. The general monomers, trimerization reaction, and IR spectroscopy characterization from Kuhns paper can be observed in Figure 1.3.

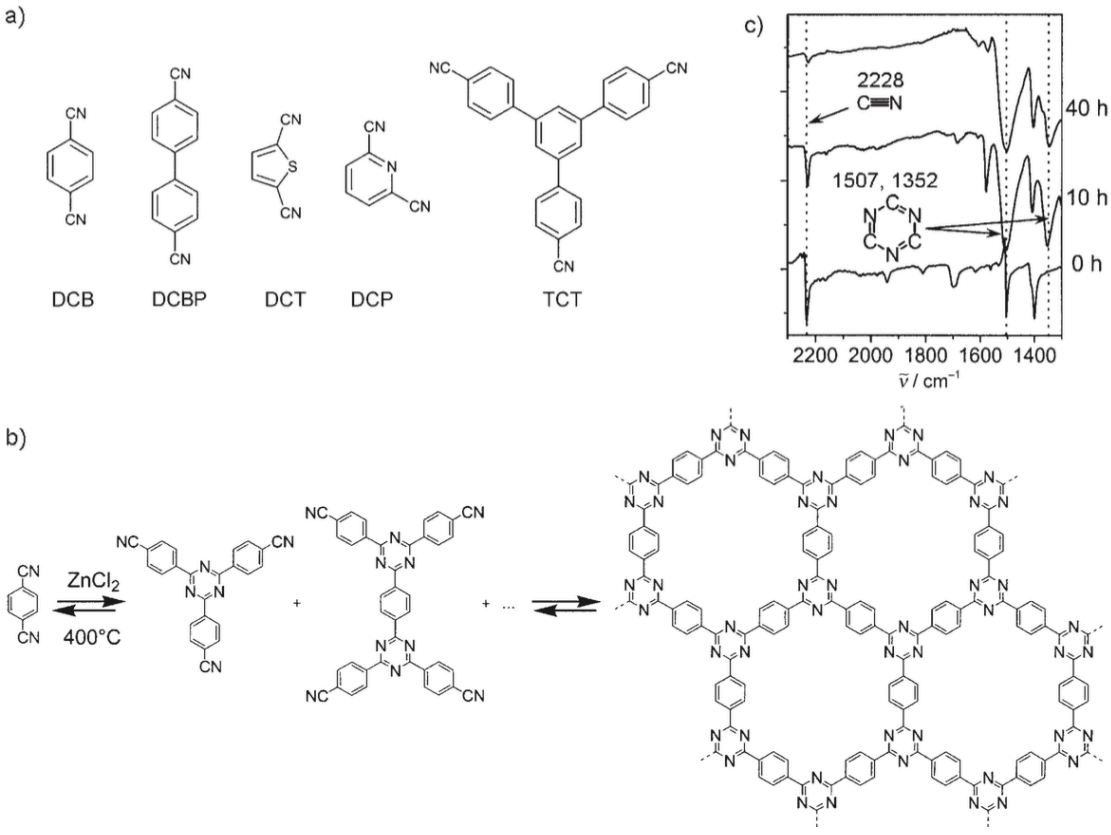

Figure 1.3. Different nitrile starting monomers of CTFs listed in (a). The general reaction scheme of nitrile trimerization and ultimately polymerization into CTF and drawn in (b). IR spectroscopy tracking of nitrile bond and triazine ring formation is displayed in (c)[5]

The BET specific surface areas of CTFs made from monomers in Figure 1.3a range from 584-2475 m^2/g. This is an important factor, which begins to correlate the starting length of the monomer influences both surface area and pore diameter.

1.4 Dicyanopyridine as a Unique Monomer

Of the many monomer units to build CTFs from, 2,6-dicyanopyridine (DCP) is particularly interesting. The presence of a pyridine functionality on the dicyano containing monomer, produces bipyiridine binding sites upon polymerization. These sites are especially useful for the chelation of metal ion as demonstrated by Schuth et al.[6] In this work, a CTF was built using DCP as the starting material, reaching 1061 m^2/g in surface area. Though the overall structure was amorphous, BET gas sorption analysis reealed a 1.4 nm average micropore diameter. Post synthesis and washing the framework was introduced to K_2PtCl_4 metal in solution at which point the framework chelated the platinum ions. The synthesis scheme and proposed CTF structure is outlined in Figure 1.4. This metal binding was confirmed though X-ray Photoelectron Spectroscopy (XPS) and Energy Dispersive X-ray Spectroscopy (EDX) mapping.

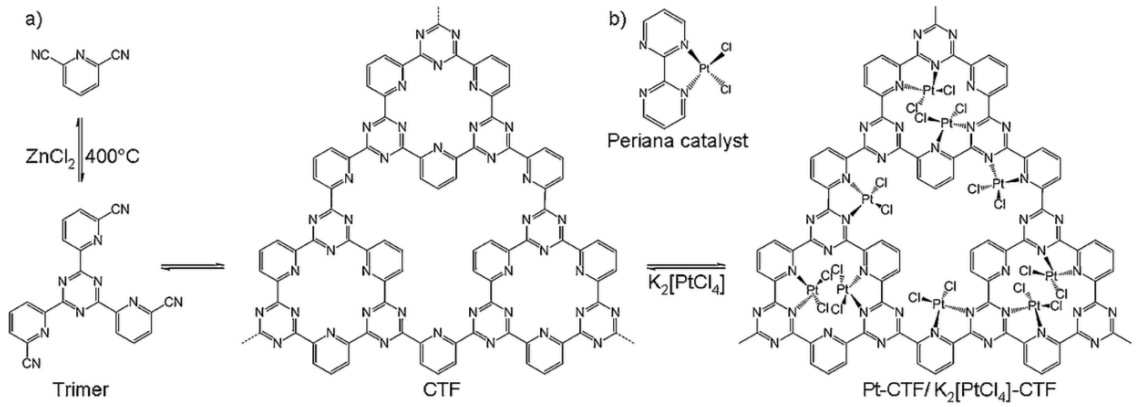

Figure 1.4. The 2,6-dicyanopyridine monomer unit is displayed in (a). Upon heating in molten $ZnCl_2$ a trimered unit is displayed along with its proposed structure. The resemblance of Periana's catalyst to Pt loaded CTF is shown in (b).

Subsequent to Pt binding, Schuth and coworkers demonstrated the catalytic potential as well as robustness of CTFs. The Pt loaded CTF was used as a heterogenous catalyst for methane to methanol conversion. This involves heating the CTF in oleum, otherwise known as concentrated H_2SO_4, a very corrosive acid. The catalysis was successful as well as recyclability of the reaction using the same material. This work exhibited many key desirable properties of CTFs: metal binding, exceptional stability, and heterogeneous catalyst activity.

1.5 The N-Heterocyclic Carbene

N-heterocyclic carbene-metal complexes have been increasingly replacing traditional phosphine and amine-type ligands.[7] This has been due to their ability to add reactivity at the same time stability to NHC-metal complexes.[8] This discovery has loaned

to the huge application of NHCs in organometallic synthesis and catalysis. These desirable properties of NHCs stem from their strong σ –donorship to the metal center and π -acceptor function. During which NHC to metal σ-donation creates a near permanent chelation, as well as metal to NHC back-donation into the π * orbital and NHC to metal π to d donation.[7] The result is highly stable metal-complexes which have been well proven to a variety of usages.

1.6 Adsorption Theory

Adsorption studies will be conducted to measure the free surface area of the material (CTFs) as well as total gas uptake. In our case, we will use volumetric analysis to obtain our data. The basis of surface area analysis stems from when a given amount of adsorptive gas is adsorbed; a pressure change should be observed. The amount of gas being adsorbed can be calculated if the void volume of adsorbent is known. Assuming a characteristic area per molecule adsorbed on the surface of a solid, the surface area of the solid can be calculated. Surface area calculations involve the Brunaur-Emmett-Teller (BET) method, which follows the equation[9]:

$$\frac{1}{W[(P_0/P) - 1]} = \frac{1}{W_m C} + \frac{(C - 1)}{W_m C} \frac{P}{P_0}$$

From the equation, W and W_m are absorbed and monolayer weights respectively. C is the BET constant, which depends on the heat of absorption of the first and second layer of absorbent. The constant will justify magnitude of interaction between the material and its absorbent.

Estimation of enthalpy of absortion (Qst) can be calculated using the Clapeyron Equation:

$$\ln\left(\frac{P_1}{P_2}\right) = \frac{\Delta H_{vap}}{R}\left(\frac{1}{T_2} - \frac{1}{T_1}\right)$$

The sample is measured at two different temperatures, to yield two different pressures, and hence the **Δ**H enthalpy of absorption can be calculated by solving for **Δ**H in the Claperyron equation. By solving for the enthalpy of absorption, we may calculate the binding energy of our material for a specific gas, in our case carbon dioxide.

References

(1) Wang, W. *Chem Soc Rev.* **2013**, *42*, 548.

(2) Batten, S. R.; Champness, N. R.; Chen, X.-M.; Garcia-Martinez, J.; Kitagawa, S.; Öhrström, L.; O'Keeffe, M.; Paik Suh, M.; Reedijk, J. *Pure Appl. Chem.* **2013**, *85* (8), 1715.

(3) Cote, A. P. *Science (80-.).* **2005**, *310* (5751), 1166.

(4) Rowan, S. J.; Cantrill, S. J.; Cousins, G. R. L.; Sanders, J. K. M.; Stoddart, J. F. *Dynamic covalent chemistry.*; 2002; Vol. 41.

(5) Kuhn, P.; Antonietti, M.; Thomas, A. *Angew. Chemie - Int. Ed.* **2008**, *47* (18), 3450.

(6) Palkovits, R.; Antonietti, M.; Kuhn, P.; Thomas, A.; Schuth, F. *Angew. Chem Int. Ed.* **2009**, *48* (37), 6909.

(7) H. D. Valazquez, F. Verpoort, *Chem. Soc. Rev.,* 2012, **41**, 7032-7060

(8) A. Kumar and P.K. Ahluwalia, *Eur. Phys. J.* 2012 **85**, 186

(9) S. Brunauer, H. Emmet, E. Teller. J. Am. Chem. Soc. 1938, **60,** 309

Chapter 2

N-Heterocyclic Covalent Triazine Frameworks

2.1 Introduction

Our approach is to develop advanced sorbents to sequester CO_2. Current technologies utilize aqueous alkanolamines to capture CO_2 in flue gas. The problem is, these amines though very selective towards CO_2 bind too strongly through their chemisorptive properties. An actual chemical bond is formed, which results in tremendous energy require to regenerate the alkanoamine. Utilizing phyisorption to capture carbon would be significantly more efficient. Metal-Organic-Frameworks and Zeolites have shown promising results in this area.[14-16] Their performance though strong, is still in their infancy and there is still great room for improvement. CTFs with their high chemical and thermal stability may prove to be a potentially interesting material for CO_2 sequestration. Covalent Triazine Frameworks (CTFs) are a new class of crystalline organic polymers. These CTF materials possess a 2-dimensional (2D), highly porous structures, with surface areas ranging from 500-3000 m^2/g.[1] Moreover, CTFs are stable under highly acidic and basic conditions, and can withstand high temperatures above 450 ^oC without decomposition. CTFs, are made of cheap, earth abundant materials, making them a suitable material to be used a permanent sorbent in underground geological reserves for CO_2. The extended networks of benzene and triazine rings in CTFs are linked in a completely conjugated planar array resembling the recently discovered graphene; but with greater physical access to the π-system through the high porosity. This may result in interesting electronic properties. Therefore, CTFs represent a versatile new material with significant potential for diverse applications. We hypothesize the strong dipole moment of the NHC-carbene chelated metal center can be used to enhance CO_2 absorption, and tune the electronic properties of the resulting CTFs. Furthermore, with

unique tunable structures and electronic attributes, CTFs may prove to be an invaluable material for electronic device fabrication.[3]

In this study, we demonstrate how to synthesize a new CTF, which contains the NHC functional group with high crystallinity. Since reversibility is the most essential condition for producing materials with good crystalline orientation, we utilize a slow cooling process to maximize reversibility. The NHC functionality will allow us to chemically modify the CTFs porous structure post-synthetically, in other words, after the framework has been constructed. We hope incorporation of functional groups, not only by the imidazolium ring, but also its variable counter-ion to allow a great deal of flexibility and allow us to tune various properties. Furthermore, we see the 2D-fully conjugated structures of CTFs as a suitable material for device fabrication. We plan on using exfoliation techniques to produce single or thin-layers and study its electron transport properties.

2.2 Materials and Methods

Reagent grade 4-aminobenzoic acid, glyoxal (40% aqueous solution), paraformaldehyde, and Zinc Chloride (anhydrous) were purchased from Sigma-Aldrich and used without further purification. Unless stated otherwise, all reactions were done in air without the use of inert gas atmosphere. ^{1}H NMR spectra were recorded on Bruker Avance spectrometers (400, 500 MHz) and are reported relative to their deuterated solvent signals. The data for ^{1}H NMR spectra are reported as follows: chemical shift (δppm), coupling constant (Hz) and integration. PXRD measurements were performed on

a Bruker D8 Discover Diffractometer, Absorption measurements were performed on a Micromeritics Tristar II porisometer at their respected temperatures and pressures.

Synthesis of 1,3-Bis(4-cyanophenyl)imidazolium Chloride. (NHC-CTF Monomer) The successful synthesis of the starting monomer for our proposed NHC-CTF is outlined in Scheme 1, using a modified procedure from Sen et. al.[4] The reaction took place in a round bottom flask capped with septum, under reduced pressure and minimal exposure to air. Anhydrous solvents were used to increase yield. The reaction involves the condensation of 4-amino-benzonitrile with glyoxal in methanol to produce the intermediate. The intermediate is recovered through filtration, washed with cold methanol, and then dried in air. Lastly, the intermediate is reacted with paraformaldehyde, which adds the final apical carbon of the imidazole ring. H-NMR and ESI-Mass Spectrometry characterization confirmed our proposed product, NHC-CTF Monomer. Purification of the monomer was performed by recrystallization, using acetonitrile at room temperature.

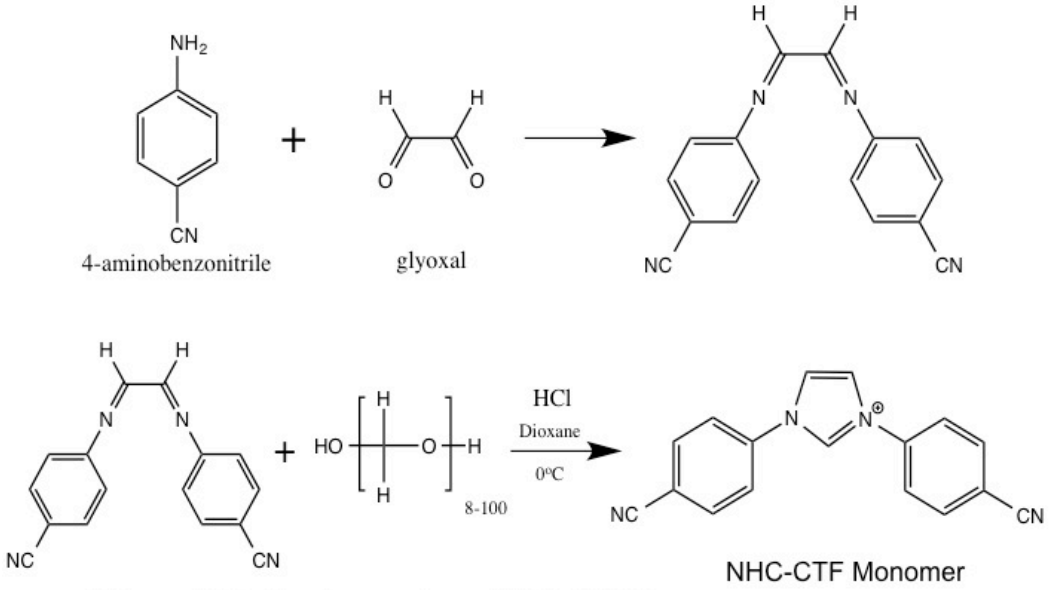

Scheme 1. Synthesis procedure of NHC-CTF Monomer

NHC-CTF Synthesis. A 1:10 molar ratio of NHC-CTF Monomer : $ZnCl_2$ was packed into a quartz tube under inert atmosphere. The tube was flame sealed en vacuo and placed into a tube furnace at 400 ^{o}C for 40 hrs. The chemical reaction is outlined in Scheme 2. The material was then slow cooled to room temperature at 3 ^{o}C per hr, and subsequently washed with copious amounts of 3M HCl, THF, and Acetone to yield NHC-CTF. The remaining black powder was collected by filtration then dried in vacuum (10^{-3} torr) for 4 hrs. For de-solvation, the material is heated to 120^{o}C under high vacuum (10^{-6} torr) overnight. Yield is roughly 90%.

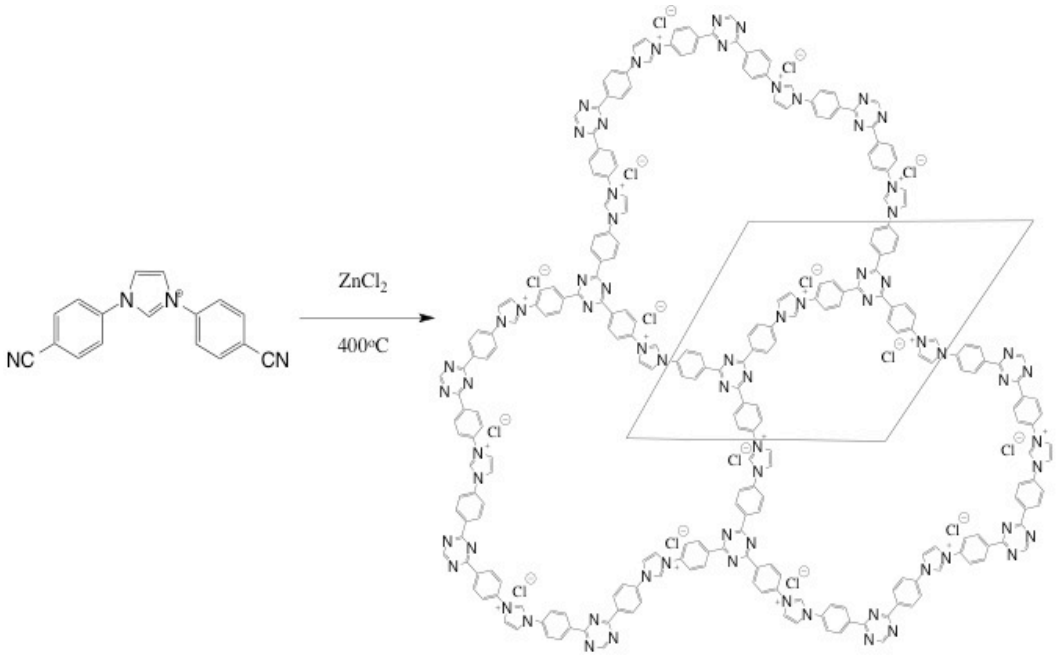

Scheme 2.2. Polymerization of monomer into NHC-CTF. Three cages

Solvent exfoliations of NHC-CTF were obtained using solvents Acetonitrile, DMF, or IPA in combination with 10 hrs of bath sonication. All the solvents provided similar samples, which are roughly 1000 nm in length and 400 nm in height. Mechanical exfoliations of NHC-CTF were carried out using an agate mortar and pestle. 50mg of CTF were placed into a 3-inch mortar, with 1-2 drops of methanol added, and the sample was ground for at room temperature for 30 mins. The resulting solid was re-suspended in 100 mL of methanol, and centrifuge at 8000 rpm for 5 mins, obtaining a clear solution. For TEM imaging, samples were drop coated onto carbon coated copper grid and dried at room temperature.

2.3 Results and Discussion

^{1}H-NMR confirms the identity of our starting monomer. All protons are aromatic and found in the proper sp^2 aromatic region of the spectrum. Furthermore, integrations confirm the proper ratio between imidazolium protons (ImH) and aromatic ring protons (ArH) as shown in Figure 2.1. ^{1}H NMR (400 MHz, DMSO-d6, 25^{o}C : a 10.8 (s, 1H, ImH), b 8.74 (d, 2H, ImH), c 8.26 (d, 4H, ArH), d 8.2 (d, 4H, ArH).

ESI-MS confirms the molecular weight of our desired product in Figure 2.2. ESI-MS (m/z): 271.1 (100%) Fragmentation products are consistent with our proposed molecule. The spectrum was acquired in the positive region, giving further evidence our starting monomer is positively charged. An anion scan was performed on the monomer through elemental analysis confirming Cl^- as the counterion to the monomer.

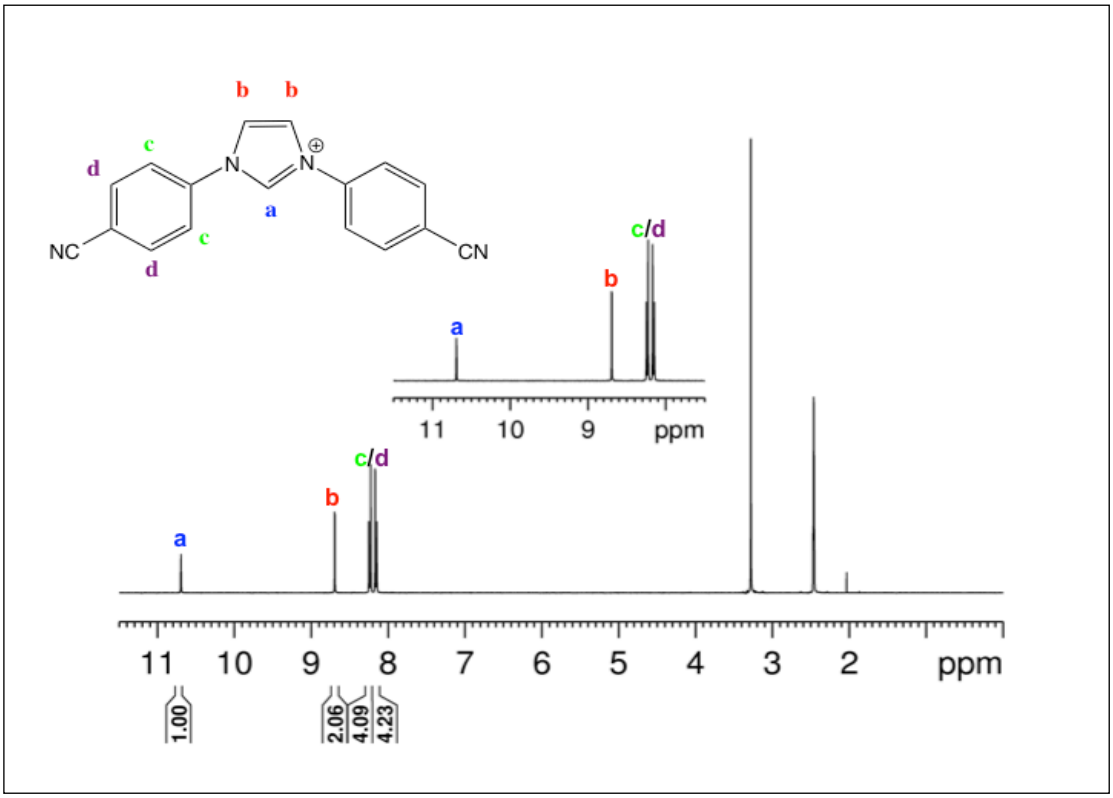

Figure 2.1. ^{1}H-NMR of NHC-CTF Monomer.

Though the synthetic procedure produces monomer in high purity, we observed a direct correlation between crystalline quality of the CTF and the crystallinity of the starting material. To help ensure the highest purity of monomer and pre-align the molecules, we performed recrystallizations in acetonitrile. Higher surface areas, uniform grown, and fewer defects were observed when pre-crystallizing the monomer powder.

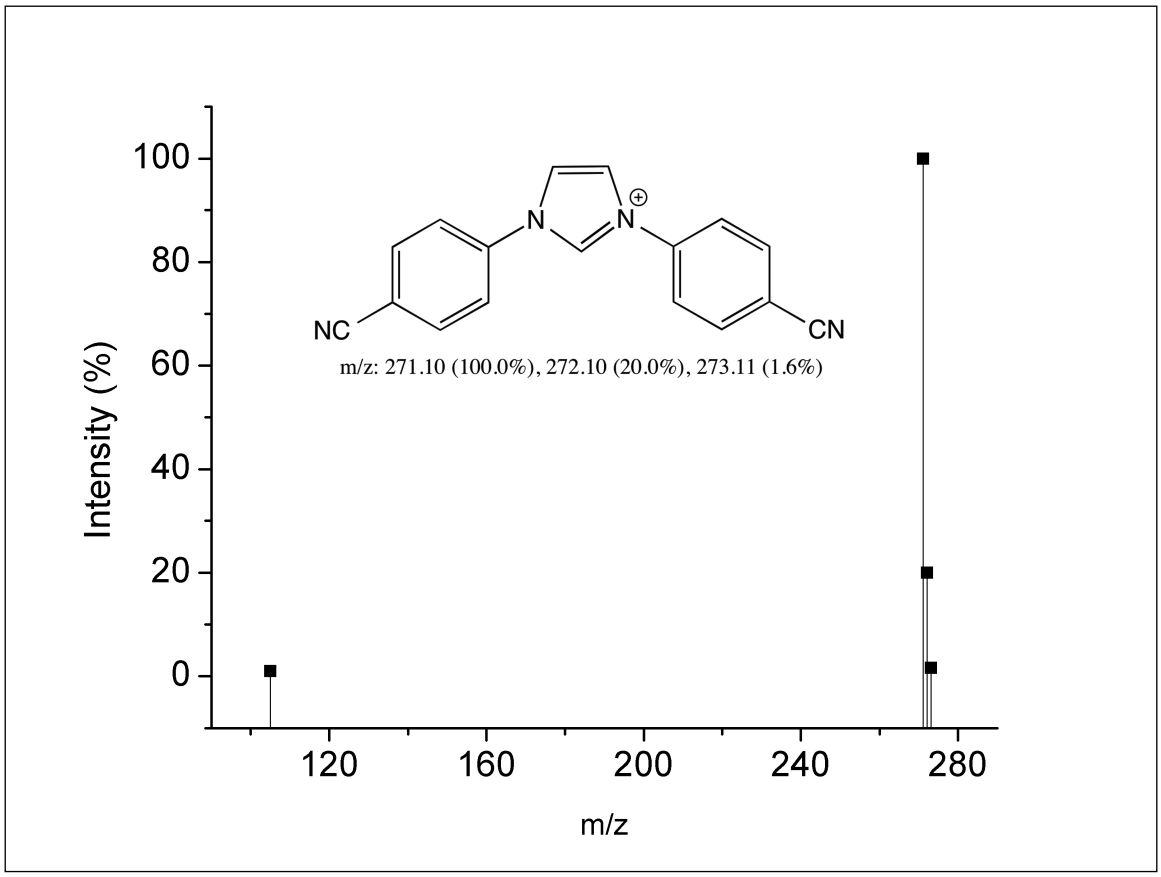

Figure 2.2. ESI-MS of NHC-CTF Monomer, positive spectrum

Powder X-ray Diffraction (PXRD) displays two main reflection peaks at 2**θ** = 4.6°, and 26.2 °. Several 2D confirmations were investigated including AAA stacking, ABAB stacking. Best-fit simulations using Materials Studio v4.3.0.0 are shown in Figure 2.3 to reveal peaks corresponding to [100] and [001] reflections in an eclipsed AAA stacking structure. Unit cell parameters used for simulation were a = b = 25.4 Å and c = 3. 4 Å, corresponding to anticipated pore size and pi-pi interlayer stacking respectively. Peak broadening simulations were also used to account for limited long-range crystalline order in the structure. While it is possible to grow large single crystals with appropriate flux ratios and temperature profiles, we will get much higher surface area and pore access

with smaller grain sizes. Our theoretical predictions match well with the calculated d-spacings of the [100] and [001] peaks. The intensities of the simulated pattern versus the experimental differ greatly, with the [001] interlayer-stacking peak overwhelming the [100] pore peak. This suggests that the crystal preferentially grows along the C-axis instead of along the AB-plane. While this is unusual for a layered structure, this could be a result of the $ZnCl_2$ flux. As the CTF is assembled, the $ZnCl_2$ would be trapped within the pores from chelation with the lone pairs of the nitrogen. This in turn creates a localized abundance of catalyst in a columnar motif, and any further assembly will occur vertically along this column. Another possibility lies with some graphitization from overheating (which would also explain the small peak at 40, corresponding to the graphite [100] peak). However, the presence of a strong [001] pore peak precludes significant graphitization: pores of the CTF cannot coexists with the unporous graphite. From the powder pattern a crystal structure is simulated with a single pore of NHC-CTF being comprised of four unit cells. The NHC-CTF with its Realeaux triangle pore shape has a smallest expected pore size of 13.9 Å and largest expected pore size of 25.5 Å as obtained through software measurements. A crystal structure representation is shown in Figure 2.4. The blue atoms represent nitrogens, and the gray atom represent carbons. Hydrogen atoms and chlorine counter ions have been omitted for clarity. Although the quality of the diffraction pattern does not allow us to perform a meaningful full structure Rietvelt refinement, the observed peaks do correspond to the largest d-spacings and their expected $2\boldsymbol{\theta}$ positions. Analysis using SAED help provide further evidence of our proposed structure.

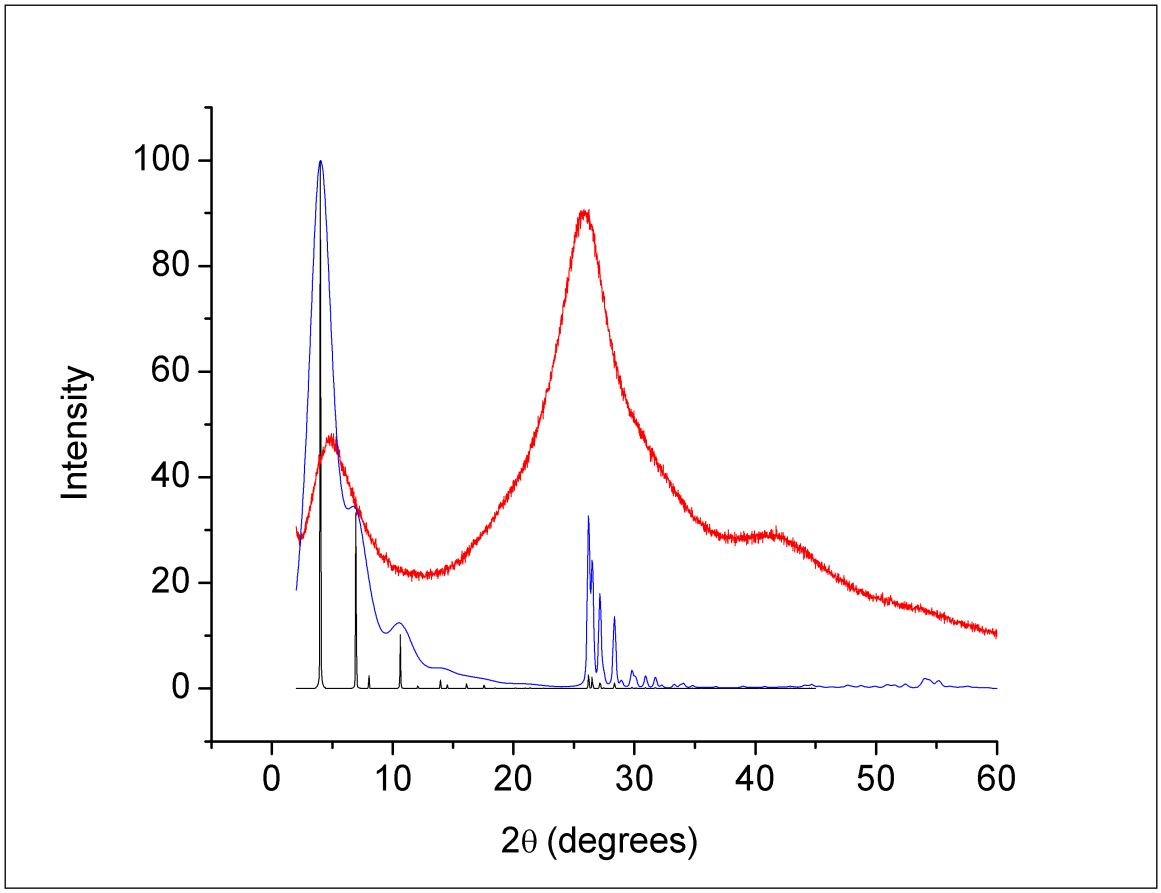

Figure 2.3. Powder X-Ray Diffraction of NHC-CTF. Experimental represented in red, optimal crystal growth simulations in black, and line-broadening simulations blue.

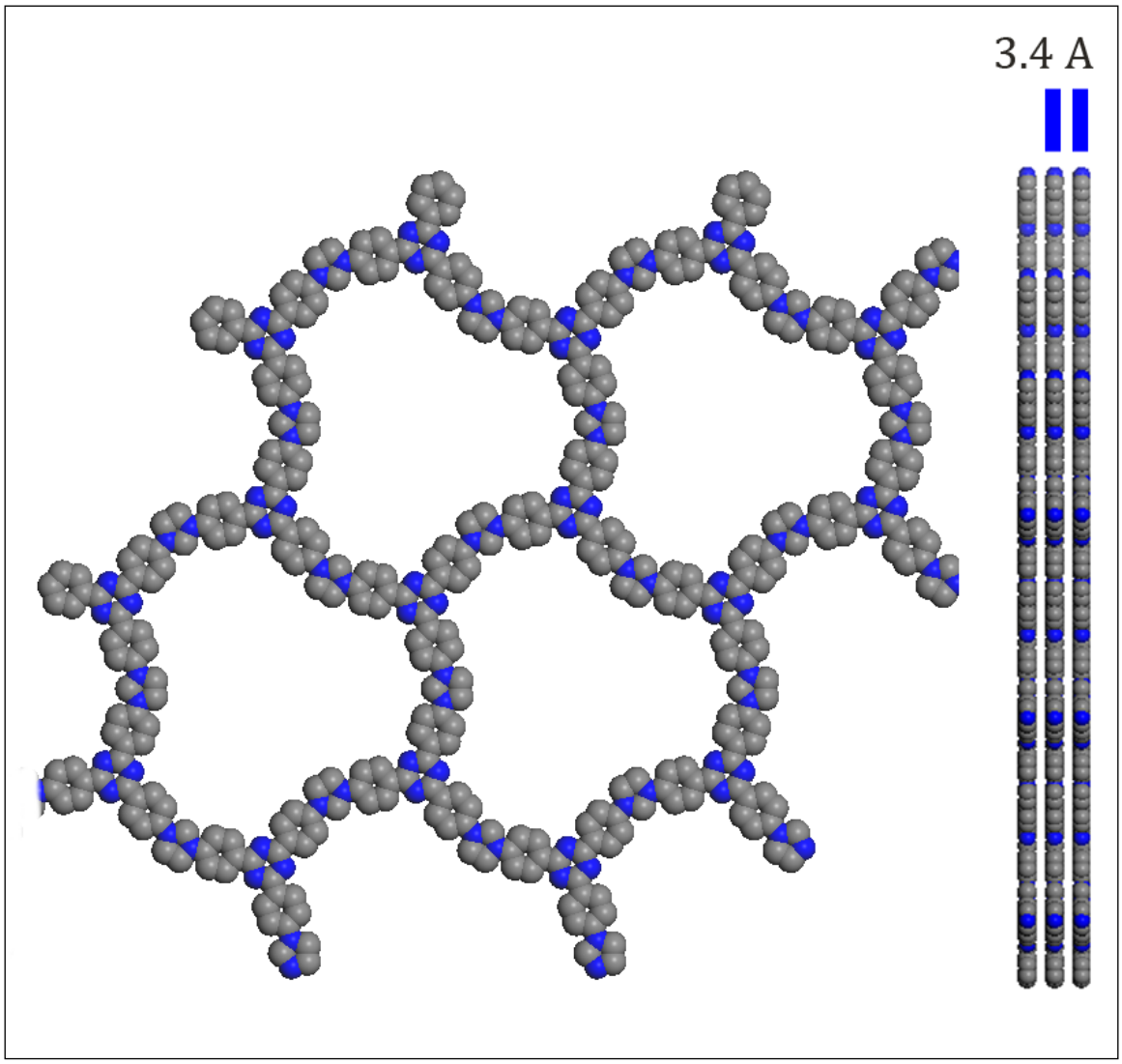

Figure 2.4. Four cages of the NHC-CTF displaying a Realeaux triangle pore shape, and stacking orientation. Each cage shares edges with six others. The nitrogen atoms are represented in blue, and carbon atoms are represented in gray. The interlayer d-spacing is calculated to be 3.4 Å

The bent nature of our starting monomer potentially creates a defect-prone building block, as seen in Figure 2.5. Three possible conformers may occur from each trimerization unit. Isomer A is threefold symmetric, with B and C being non-threefold symmetric resulting in defect units not beneficial towards CTF crystallization. This may

also be a major contributing factor to our peak broadness and limited long-range order in our PXRD patterns.

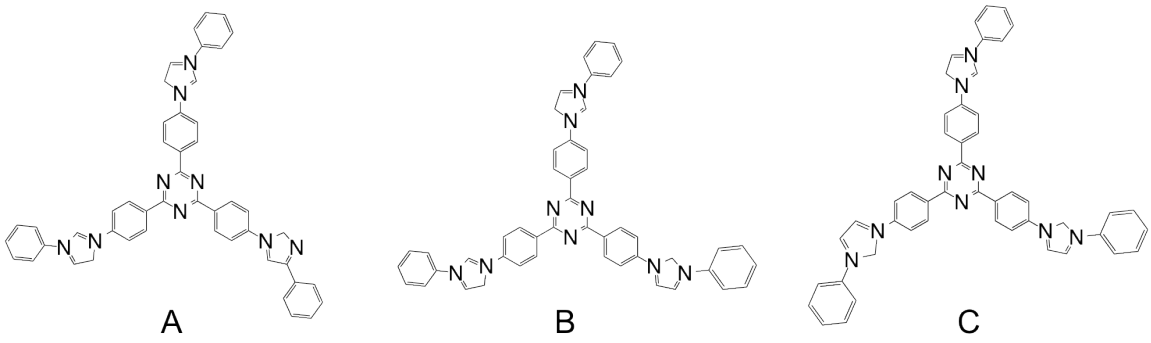

Figure 5. Three conformers are possible from the trimerization of three monomer units.

The NHC-CTF was exfoliated in DMF to produce thin samples suitable for HR-TEM analysis. Examination of the material by HR-TEM reveals clear hexagonal growth plates with regular porosity in Figure 2.6a and 2.6c. SAED pattern in Figure 2.6b show clear diffraction rings, an observation which endorses the crystalline nature of our NHC-CTF. Calculation of the rings' d-spacing correspond well to peaks: [700], [900], [10 00], [880], [990], [10 10 0] respectively. As well, the 2.5 nm pores of the CTF are somewhat visible in the HR-TEM image especially through Figure 2.6d, confirming the AAA stacking. In terms of CTFs, this is not only the first case of hexagonal growth plates being observed, but also the usage of SAED to characterize its structure.

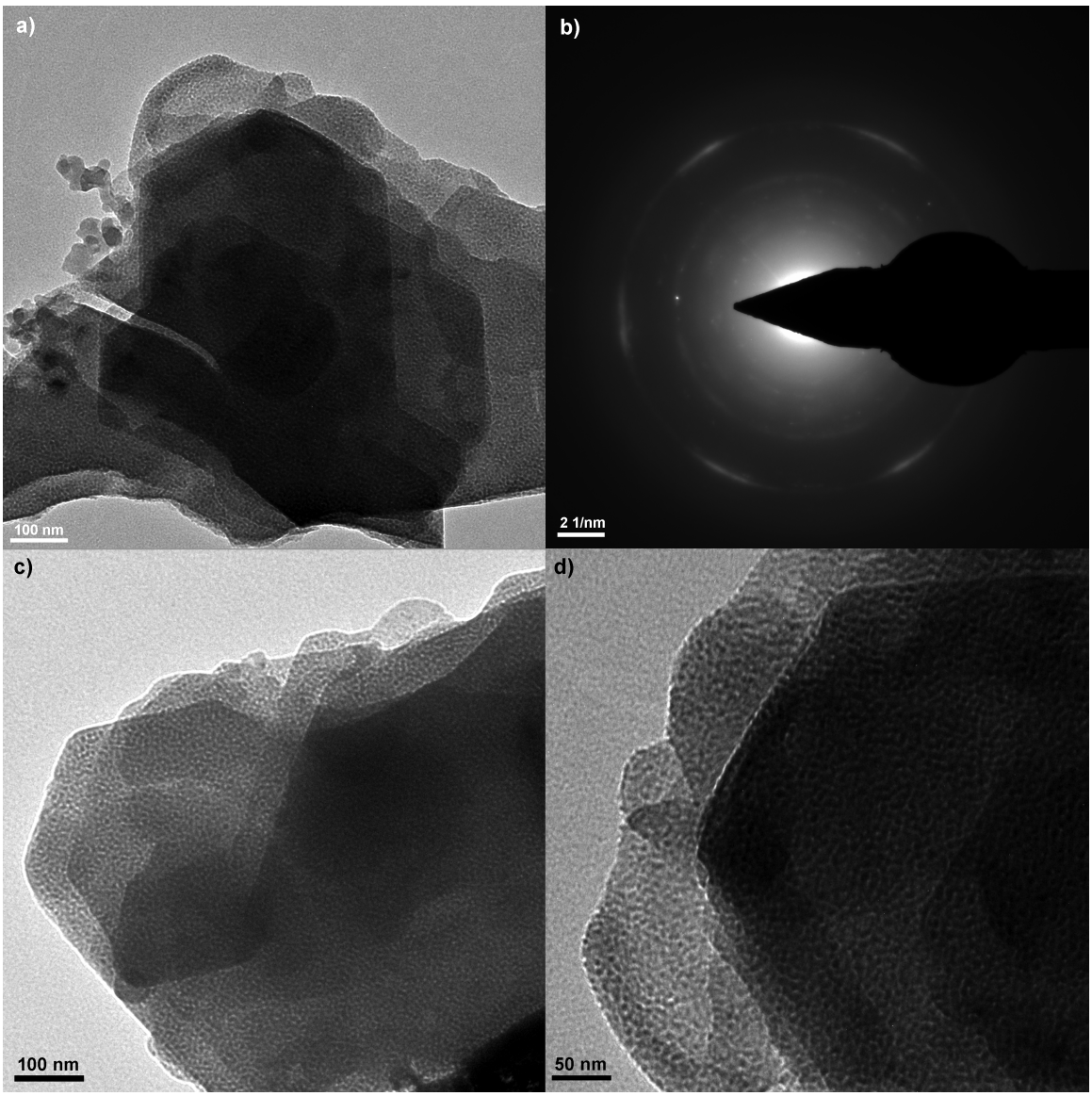

Figure 2.6. HR-TEM images of roughly 400nm thick films of NHC-CTF. SAED measurements displayed in part b. Vertically oriented pores can be observed in c and d.

Further structural evidence of covalent bonding is given through ^{13}C CP-MAS solid-state NMR (Figure 2.7). No peaks of residual cyano groups (~85 ppm) could be detected in the spectrum, confirming the compete trimerization of the starting monomer. A simulation on the NHC-CTF unit cell was conducted to show the locations of the possible sp^2 carbons in the NMR spectra. These peaks lie within the proper range of our

spectrum between δ = 110-150 ppm. As it is well known that high resolutions for solid-state NMR are difficult to obtain, our multiple aromatic carbon atoms with similar peak shifts may account for the spectrums broadness.

With the generation of our CTF-metal complex significant chemical shifts should be observed in the apical carbon of the imidazole ring. These would be attributed to the strong sigma-donarship of electrons from the carbene to the metal center, as well as pi-backbonding of electrons from the metal-center to the carbene ring.

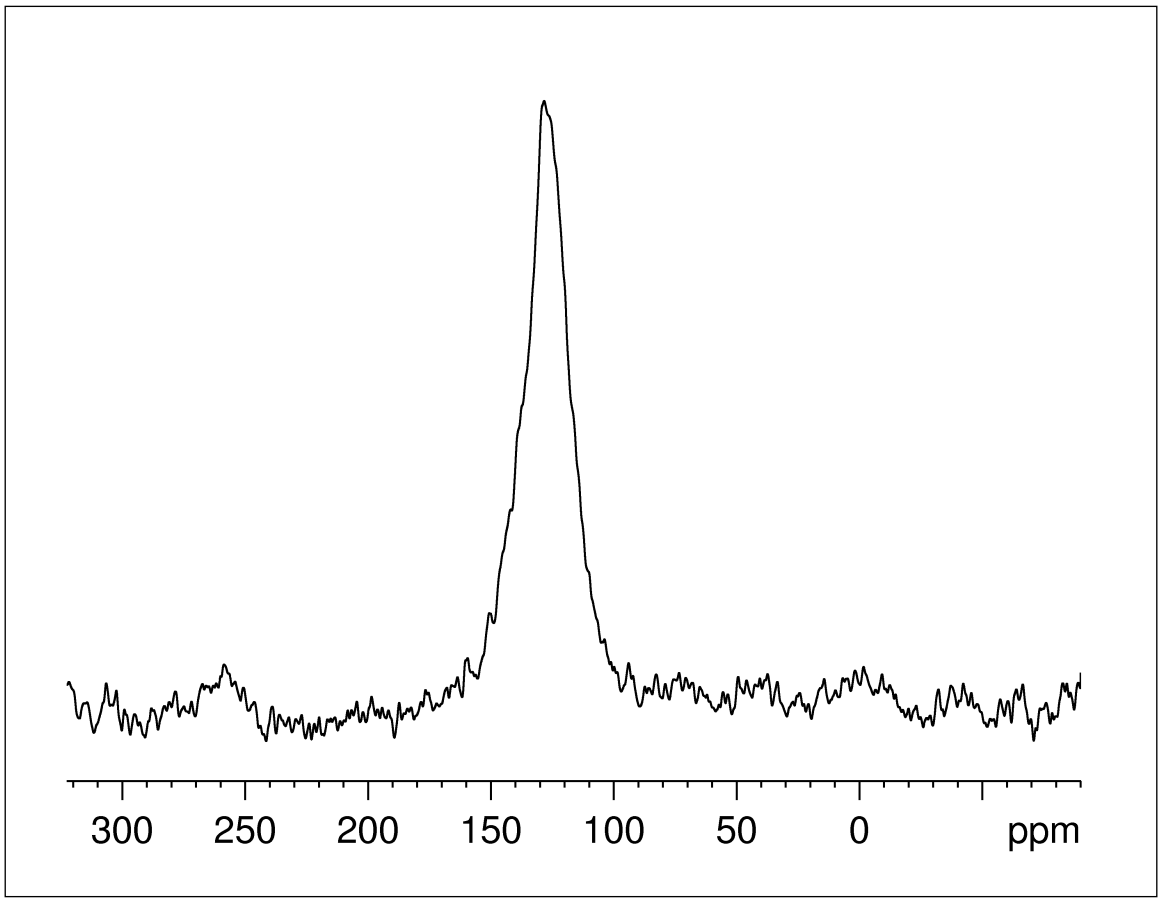

Figure 2.7. ^{13}C CP-MAS solid-state NMR, a single broad peak is observed

It should be noted the monomer to zinc salt ratio and reaction cooling rate are crucial to producing our CTF material with crystallinity. The ratio of 1:10 monomer to

zinc salt produced materials with highest surface area as observed by Kuhn et al.[1] Coupling these ratios with a cooling rate of 1.5 ^{o}C per hr, produced well-defined crystalline compounds when comparing to other organic porous materials. These synthesis conditions were found to be optimal, with deviations from monomer to zinc ration resulting in a loss of surface area, sometimes as low as 350 m^2/g. A comparison is shown in Figure 2.8. Under non-optimized synthesis procedures the CTFs grow with heavy defects, lower crystallinity, and surface area. Their physical appearance can clearly be noted as well. The roughness of the surface of a non-optimal growth CTF in comparison to the shiny metallic-like optimized CTF on the right. It is well known materials with black, shiny appearances tend to have conductive behaviors, and we see the same correlation with our material. Upon optimized growth conditions, the sheet resistance is reduced over two orders of magnitude from roughly 25 MΩ to 0.15 MΩ. Rapid cooling of the material; post the 40 hr 400 ^{o}C synthesis gave amorphous powders with lower surface areas. Elemental analysis of the optimal reaction condition showed just a small deviation from the theoretical C/H/N values. This variation may be due to slight material carbonization of the triazine rings, which as been previously observed in these types of materials. However, the overall material is proven to be robust even after extended heating times of 80 hr at 400 ^{o}C.

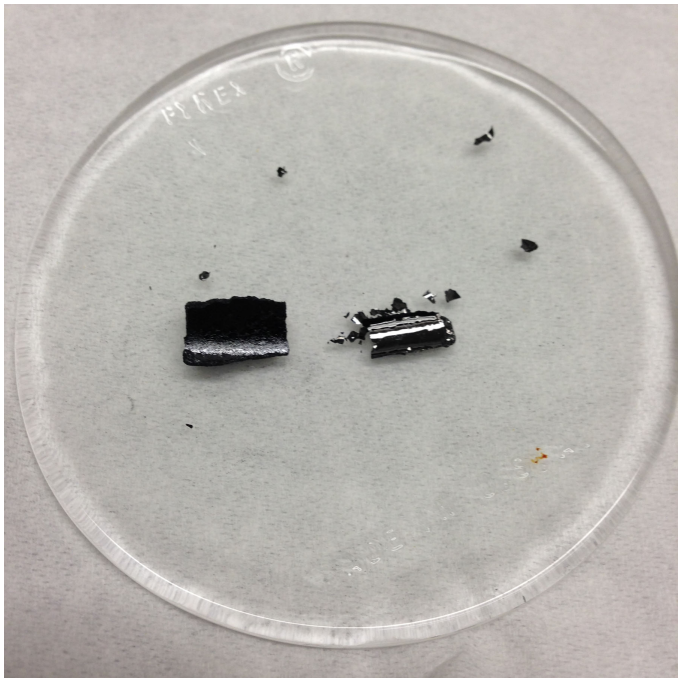

Figure 8. Photo comparison of non-optimally synthesized NHC-CTF on the left, and optimized synthesis on the right.

Further bonding studies were conducted on our CTF by utilizing Attenuated-Total-Reflectance IR Spectroscopy (ATR-IR), Figure 2.9. Our starting monomer is displayed in black, over-laid with two different samples of NHC-CTF in red and blue. The red spectrum displays our optimal CTF, with the absence of a nitrile peak ~2218, indicating successful the trimerization of our monomer. It should be mentioned it is extremely difficult to obtain clear IR spectrums from carbonaceous and carbon like materials, due to the high extinction coefficients and substantial transmission losses due to absorbance.[23-24] Consequently, our current IR spectrums are not conclusive in identifying the presence of the imidazole nitrogen for post-synthesized CTFs. A strong carbonyl peak (~1680) can be seen in our partially oxidized CTF sample. This may have been due to a small leak in the quartz tube during material synthesis.

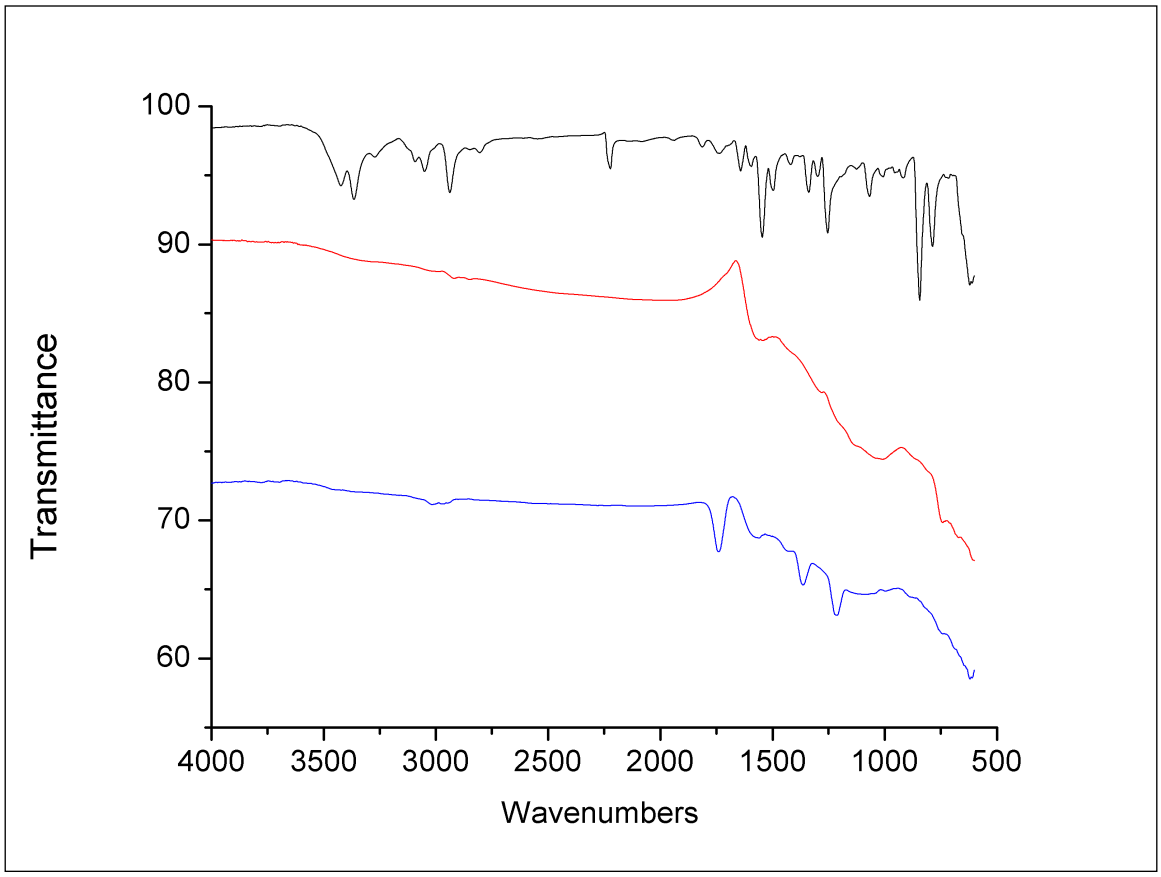

Figure 2.9. ATR-IR of NHC-Monomer (black), NHC-CTF (red) and NHC-CTF presence of defects and oxidation (blue)

Raman spectroscopy measurements (RSMs) were conducted using 514nm excitation to help identify the electronic structure of our CTF, as well as structural periodicity. We compared our spectra of CTF to that of graphite (Figure 2.10). The G peak corresponds to the doubly degenerated zone center E2g mode, which correlates to the motion of atoms in the 2D honeycomb structure. The D peak, is typically an inactive for perfect graphite, and is activated by disorder in the 2D structure. Therefore the D

band is associated with defects. This could attributed to the stress from the high-temperature synthesis, as well as formation of different conformers as outlined in Figure 2.5. Our 2D peak at ~2700 is historically called the G' peak. Comparison of the D:G preak intensity ratio suggests our CTF has a much shorter 2-dimensional ordered structure. The existence of a G peak our CTF does help confirm the formation of a 2D honeycomb structure made up of stacked triazine and benzene rings.

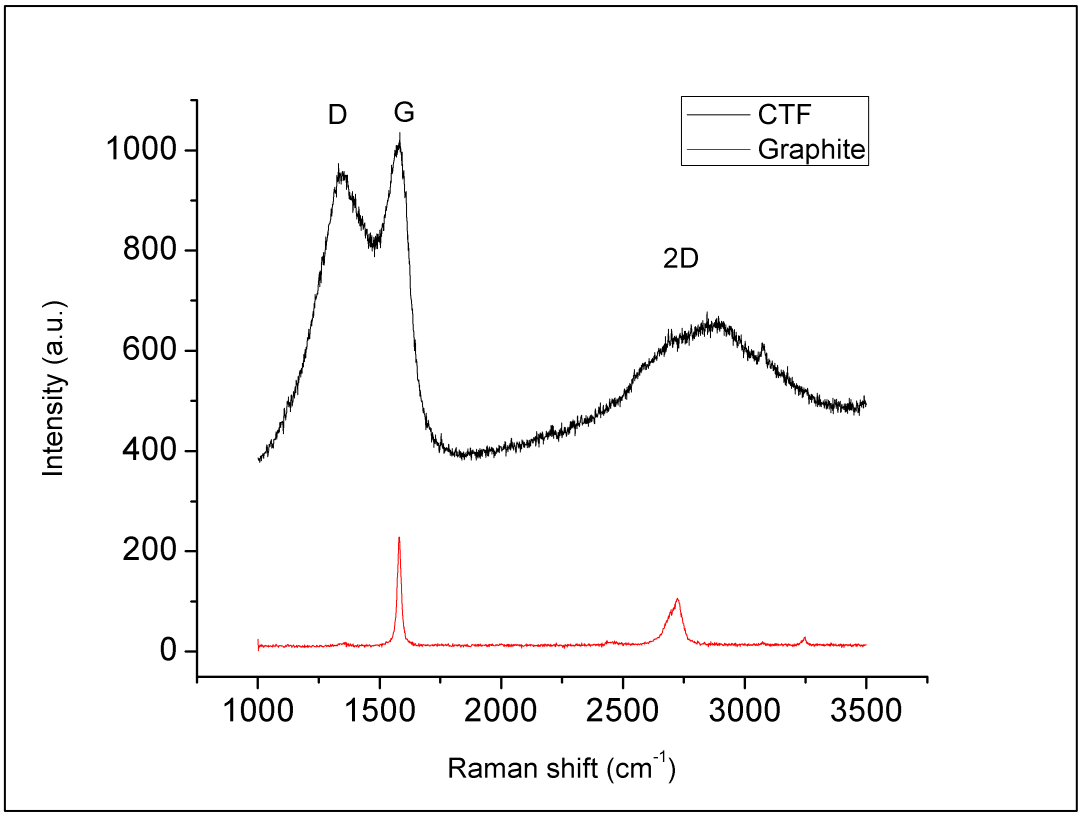

Figure 2.10. Raman spectrum of NHC-CTF and graphite.

To investigate the porosity of the NHC-CTF material, N_2 adsorption isotherms were performed on the de-solvated materials shown in Figure 2.11a. Measurements reveal a porosity of 850 m^2/g at 760 torr and 77K using BET analysis fits. The values are

in line with expected theoretical calculations of ~920 m^2/g and other 2D mesoporous COFs.[5] These measurements reveal a true Type I isotherm with no hysteresis. The absence of a mesoporous filling in the N_2 isotherm may be attributed to the unique Realeaux Triangle shape of NHC-CTF. Though total pore cavity is near 2.5 nm, three steric sites create a pinch. The result divides each mesopore into four micropore regions. Three micropore regions are located on the edges of the triangle, one located on the center, as can be more clearly seen in Figure 2.4.

In terms of absolute uptakes, NHC-CTF adsorbs 1.1wt% of H_2 at STP as seen in Figure 2.11b. This is in the moderate range of CTF type materials.[6] The absence of open metal sites for strong interactions and density of a hexagonal structure contributes to the non-optimal H_2 uptake.

NHC-CTF adsorbs 68 cm^3/g of CO_2 at 760mmHg (1atm) at 273K as shown in Fig 2.11c. This converts to 13.33 w.t%, with the highest recorded uptake of CO_2 in a CTF absorbing at 15.7 wt%.[7] Though NHC-CTF nearly approaches the best range of uptake for organic polymers, further improvements are possible. The binding of metal centers has been known to increase gas uptake abilities in various porous materials.[8] This strategy of decorating the internal framework with strong dipoles may be utilized in the future for enhancing NHC-CTFs CO_2 uptake.

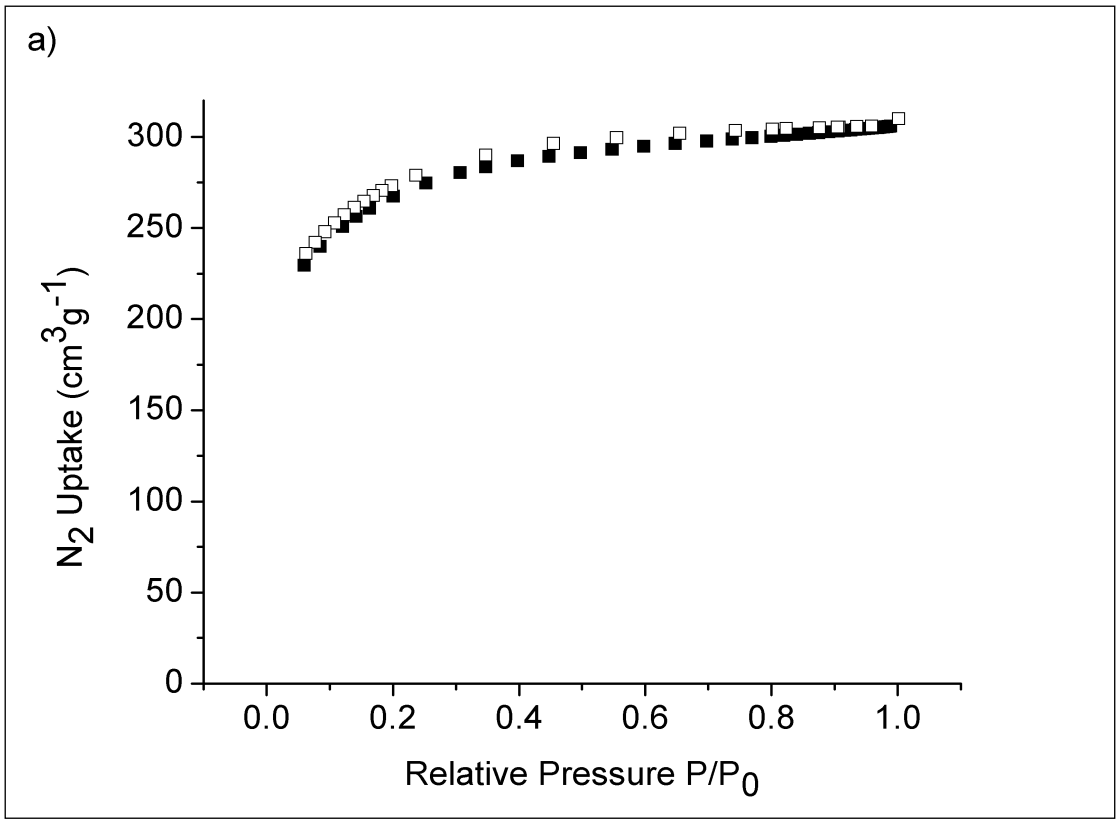
a)
300
250
200
150
100
50
0
N_2 Uptake (cm^3g^{-1})
0.0
0.2
0.4
0.6
0.8
1.0
Relative Pressure P/P_0

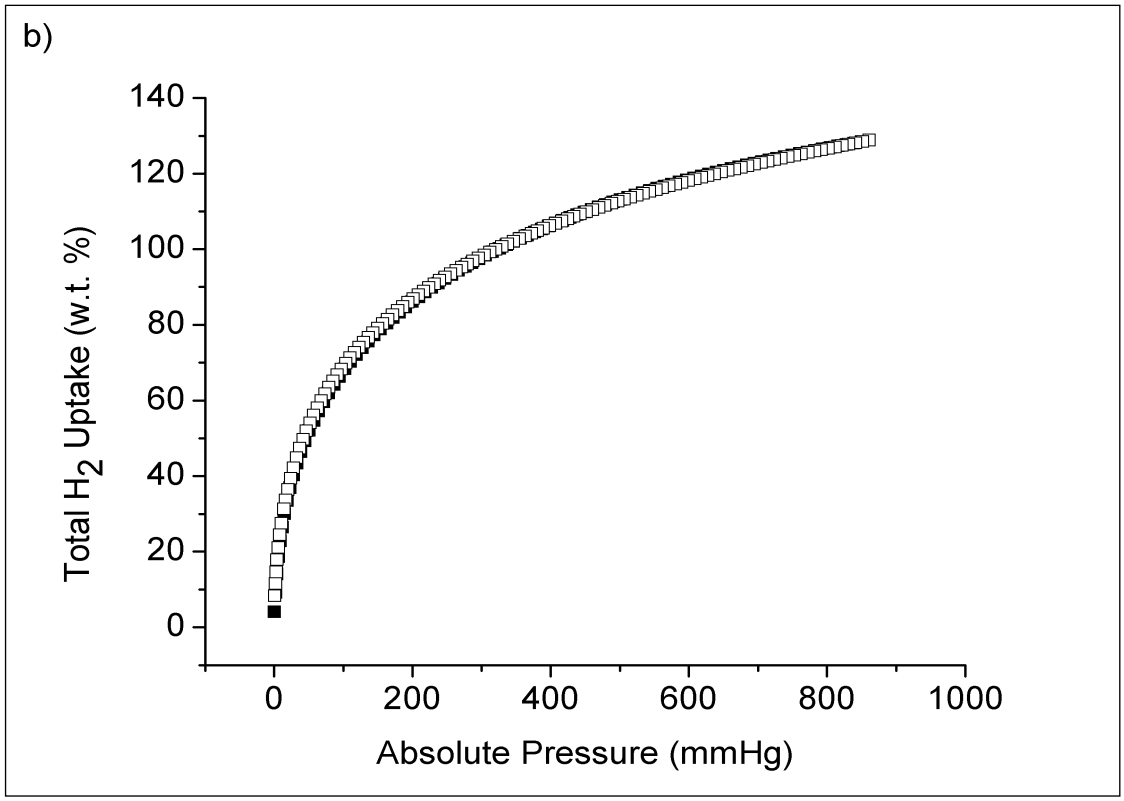
b)
140
120
100
80
60
40
20
0
Total H_2 Uptake (w.t. %)
0
200
400
600
800
1000
Absolute Pressure (mmHg)

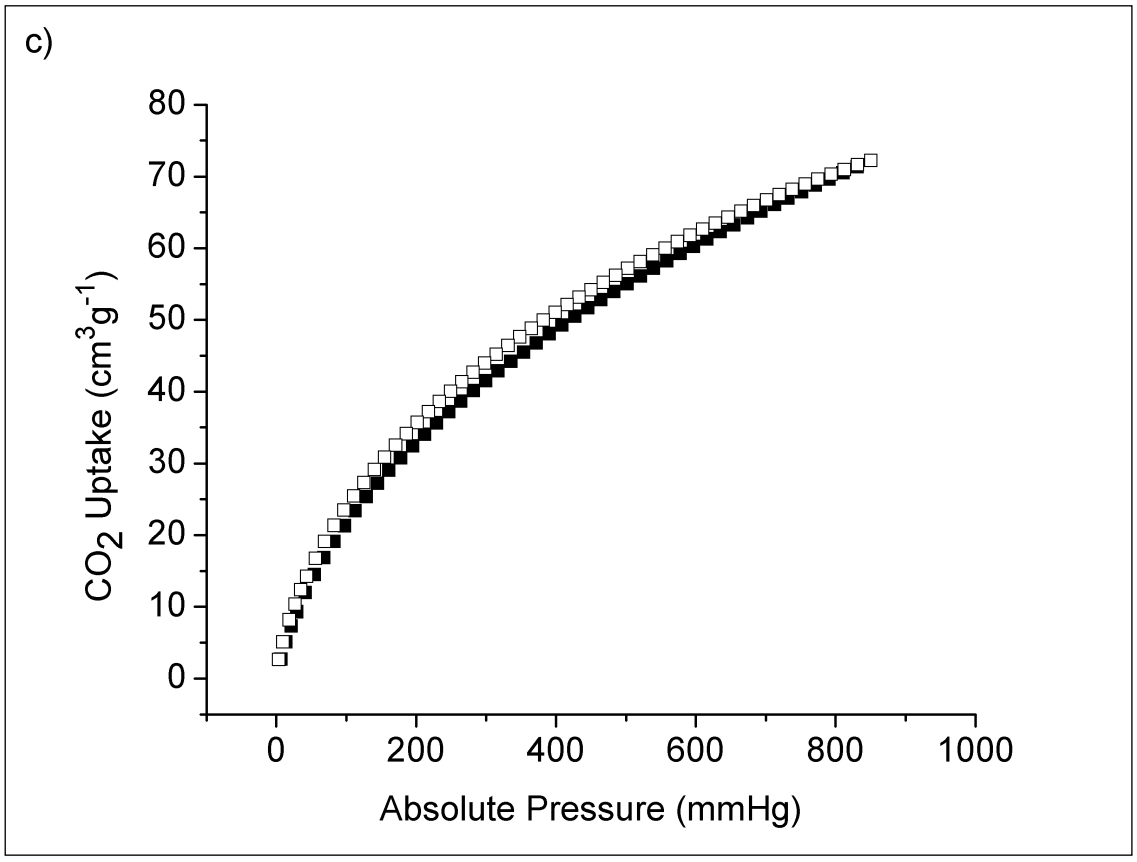

Figure 11. Nitrogen surface area measurements at 77K a), hydrogen adsorption measurements taken at 77K, plotted in w.t% at STP b), and CO_2 adsorption measurements taken at 273 K, plotted in volumetric uptake c).

Upon metallation, we expect an even greater increase in binding affinity, Qst, for CO_2 sorption, and possibly even H_2. Using our NHC complex, we can bind virtually any transition metal and also vary its counter-ion. It has been well known that open metal sites are key to increasing gas storage. However, in MOFs they traditionally have excess metal clusters, which are only present for structural support. These excess metal clusters, not only add to the overall cost of synthesis but in excess weight of the material since sorptions are measured in volumetric uptake over grams of material. Usage of an all-organic framework helps alleviate not only the chemical sensitivity of some metal-

organic bonds, but also the heavy weight of these metal atoms. Creating tunable pore electronics will employ metal centers only in the sites of need, leaving out unnecessary metal centers only there for structural support.

Mechanical grinding techniques of exfoliation were performed to produce single layer samples. This strategy has been shown to be safe, eco-friendly and energy efficient process. The process of mechanical grinding helps separate the π-π stacking of AA layers from the stable CTF layers as seen in Figure 12. The layers become thin enough where they are nearly transparent on TEM. If not for the crystal grain boundary the thin layers would be nearly indistinguishable from the carbon coated TEM grid. At the moment, the sheet size of these delaminated CTFs is only ~200 nm. Optimally we would like to produce layers at least 1 micron in length, and minimally stacked.

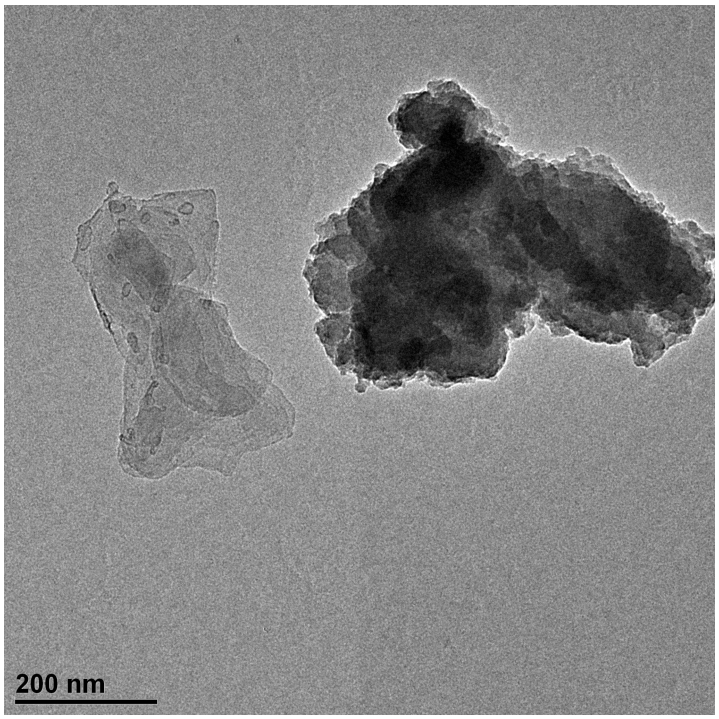

Figure 12. TEM image of mechanically ground and exfoliated NHC-CTF.

2.4 Conclusion

In conclusion, we report the synthesis of the first ionic CTF, which also contains NHC moieties throughout its structure. We show the bent monomer is susceptible to synthetic variations and are defect prone building blocks during synthesis. Yet, this is the first CTF to-date, which has been crystallized and characterized from a bent shaped starting material. Our characterization methods are unique in that the NHC-CTF is the first CTF able to be characterized by SAED. This is due to high crystallinity from careful synthesis, and employment of exfoliation techniques. Moreover, our CTF exhibits high surface area and high uptake of CO_2 and H_2 gas. These results, in conjunction with the on going efforts in exfoliations and post-synthesis modifications, are important steps toward applications that utilize CTFs in electronic devices, gas sorption, and catalysis.

Further investigations for successful formation of poly-triazine networks should be conducted. Additionally, ^{13}C and ^{15}N CP-MAS solid state NMRs utilizing isotopic labeling on the starting monomer will offer well defined peaks to evaluate bonding characteristics of NHC-CTF. TGA will help determine the overall thermal stability of this uniquely ionic CTF with specific functionalization.

A proper method of generating the NHC-Carbene needs to be developed. Some strategies include the use of adducts such as chloroform or methoxy groups[9], as well as employing harsher more sensitive reactions involving strong bases or transmetallation strategies[10]. Full characterization of the bound organometallic complex will be required. Characterization methods include CP-MAS solid state NMR and solid state UV-VIS. Upon successful metal-CTF complex formation, a difference in gas uptake volume is also expected. This effect of generating strong electric dipoles has been observed using metal

loaded variants of MOFs.[8] We expect the same type of behavior, if not better, using NHC-metal-carbene complexes. Using gas adsorption analysis a variety of adsorbants can then be tested for enhanced uptake abilities.

Exfoliation techniques need to be improved to obtain thin-layers of NHC-CTF suitable for device fabrication. Currently, these layers are ~400 nm in height. Suitable samples should be less than 100 nm for field-effect transistor measurements. Lastly, we search for adequate redox partners, which will not harm the crystal structure, yet will help promote full electron transfer.

2.5 References

1.) P. Kuhn, M. Antionetti, A. Thomas, *Angew. Chem. Int. Ed.* 2008, **47**, 3450 –3453

2.) R. Monastersky, *Nature*, 2013, **497**, 13 - 14

3.) L. Liao, Y.C. Lin, M. Q. Bao, R. Cheng, J. Bai, Y. Liu, Y. Qu, K. L. Wang, Y. Huang, and X. Duan, *Nature* 2010, **467**, 305

4.) S. Sen, N. Nair, T. Yamada, H. Kitagawa, P. Bharadwaj, *J. Am. Chem. Soc*. 2012, **134**, 19432−19437

5.) Côté AP, El-Kaderi HM, Furukawa H, Hunt JR, Yaghi OM., *J. Am. Chem. Soc*. 2007 **43**, 12914–12915.

6.) A. Bhunia , V Vasylyeva, C Janiak, *Chem. Commun.,* 2013, **49**, 3961-3963

7.) J. Roeser, K. Kailasam, A. Thomas, *ChemSusChem* 2012, **5**, 1793 – 1799

8.) E.D. Bloch, D.K. Britt, C. Lee**,** C.J. Doonan, F.J. Uribe-Romo, H. Furukawa, J.R. Long, O.M. Yaghi, *J. Am. Chem. Soc*. 2010, ***132***, 14382-14384

9.) T.M. Trnka, J.P. Morgan, M.S. Sanford, T.E. Wilhelm, M. Scholl, T. Choi, S. Ding, M.W. Day, R.H. Grubbs, *J. Am. Chem. Soc.* 2003*,* **125**, 2546-2558

10.) Z. Lu, S.A. Cramer, D.M. Jenkins, Chem. Sci., 2012, **3**, 3081–3087

11.) K. Sumida, D. Rogow, J. Mason, T. McDonald, E. Bloch, Z. Herm, T. Bae, J.R. Long, *Chem Rev.*2012, **112**, 724-781

12.) U.S. Environmental Protection Agency: http:/www.epa.gov/climatechange/emissions/co2_human.html

13.) N. Macdowell, et al. *Energy Environ. Sci*., 2010, **3**, 1645–1669

14.) H. Deng, C. J. Doonan, H. Furukawa, R. B. Ferreira, J. Towne, C. B. Knobler, B. Wang and O. M. Yaghi, *Science*, 2010, **327**, 846–850

15.) M. D. LeVan, A. I. Benin, P. Jakubczak, D. B. Lanuza, M. Galloway, J. L. Low and R. R. Willis, *J. Am. Chem. Soc*., 2009, **131**, 18198–18199.

16.) B. Wang, A. P. Cote, H. Furukawa, M. O'Keeffe and O. M. Yaghi, *Nature*, 2008, **453**, 207–212.

17.) K. S. Novoselov KS, A. K. Geim, S. V. Morozov, D. Jiang, Y. Zhang, S.V. Dubonos, I.V. Grigorieva, and A. A. Firsov, *Science,* 2004*,* **306**, 666–669

18.) K. S. Novoselov, A. K. Geim, S. V. Morozov, D. Jiang, M. I. Katsnelson, I. V.

Grigorieva, S. V. Dubonos, A. A. Firsov, *Nature,* 2005, **438**, 197–200

19.) Y. Zhang, J. W. Tan, H. L. Stormer, P. Kim, *Nature*, 2005, **438**, 201–204

20.) M. Y. Han, B. Oezyilmaz, Y. Zhang, P. Kim, *Phys. Rev. Lett.* 2007, **98**, 205-208

21.) K. I. Bolotina, K. J. Sikesb, Z. Jianga,d, M. Klimac, G. Fudenberga, J. Honec, P. Kima, H. L. Stormer, *Solid State Commun.* 2008 **146**, 351–355

22.) C. Lee, X. Wei, J.W. Kysar, J. Hone, *Science,* 2008, **321**, 385–388

23.) K.F. Mak, C. Lee, J. Hone, J. Shan and T. F. Heinz, *Phys. Rev. Lett.* 2010 **105,** 136805

24.) A. Kumar and P.K. Ahluwalia, *Eur. Phys. J.* 2012 **85**, 186

25.) H. D. Valazquez, F. Verpoort, *Chem. Soc. Rev.,* 2012, **41**, 7032-7060

26.) C. Heinemann, et al., *J. Am. Chem. Soc.,* 1996, **118**, 2023-2038

27.) R. A. Friedal, G.L. Carlson, *J. Phys. Chem*. 1971, **75**, 8-17

28.) J. S. Mattson, HB Mark Jr., *J. Col. Inter Sci*, 1969, **1**, 31-35

Chapter 3

The Exfoliation of Covalent Triazine Frameworks

3.1 Introduction

Covalent Triazine Frameworks (CTFs) are a new class of organic two-dimensional (2D) polymer materials, with regular 1-D pore channels, high surface area, and good crystallinity.[1-4] They resemble the recently discovered Covalent Organic Frameworks (COFs)[5], in which organic molecules are linked together with covalent bonds and obey reticular chemistry principles to form highly ordered structures.[6,7] However, their synthesis procedures differ in that CTFs utilize ionothermal trimerization of nitriles into triazine rings which are resistant to hydrolytic and oxidative stress. Under these synthesis conditions, the results are materials with black and shiny luster indicative of low band-gap and conductive materials. Due to their high stability, porosity, and functionality, CTFs have found many applications in areas such as catalysis[8], energy storage[9-11], and adsorption[12]. Recently, the exfoliation of 2D polymers has gained significant interests[13-17] for the advanced properties through greater access of surface area or sheet restructuring from 2D polymers[18-22]. Despite these recent advances in the solution phase exfoliation of 2D polymer materials, the exfoliation of CTFs has yet been explored. Hence, we set out to acquire synthetic strategies to obtain liquid suspensions of CTFs in their thin sheet form, similar to what has been achieved with graphite[23-25]. In this paper we developed a method (Figure 3.1) to produce Triazine Nano-sheets (TNS) as the first step into producing thin-layers of CTFs and study their electronic characteristics.

3.2 Experimental

Synthesis of CTF-1. Dicyanobenzene (2g) and Zinc Chloride (2.1g) were packed into a quartz ampoule under inert atmosphere and placed under vacuum. The ampoule was then flamed sealed and placed into a tube furnace at 400^{o}C for 40hrs.

Exfoliation Procedure. In a typical fabrication, CTF powder (5 mg) was immersed in IPA (5 mL) along with either AA or SA (3-5% by vol%). The vials were sonicated for 3 hrs and the dispersions were centrifuged at 8000 rpm for 5 mins to remove large particulates. The supernatant was collected. To remove excess sulfuric acid when present, samples were placed under dialysis against deionized water, changing fresh water twice daily for seven days.

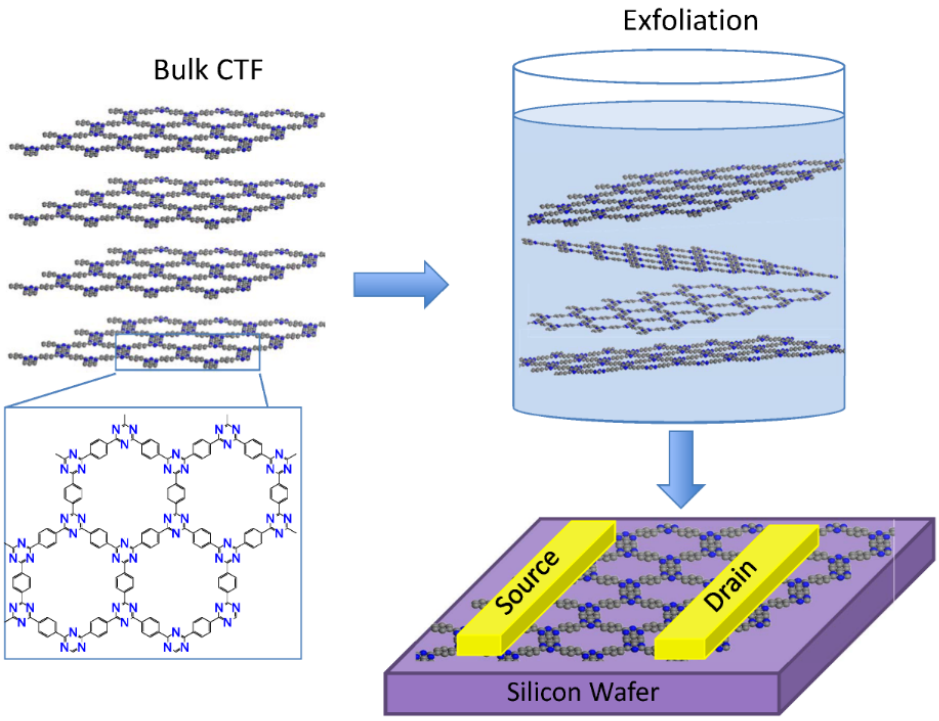

Figure 3.1. Schematic representation of the exfoliation process via chemical and the fabrication of a CTF device.

To produce TNS, we utilized sonochemical liquid exfoliation consisting of IPA with the addition of either acetic acid (AA) or sulfuric acid (SA) respectively. It has been well known that low solubility cyaphenine (2,4,6-triphenyl-1,3,5-triazine) molecules can be

dissolved in warm solutions of both acids.[26] The presence of these acids in IPA improves the solubility of cyaphenine, as seen in the absorbance spectrums of Fig 3.2. The structural similarity of cyaphenine to CTF-1 can be observed in Fig 3.1b. Taking advantage of the resemblance of cyaphenine to the extended framework CTF-1, we incorporated these reagents into our exfoliation solvent. We hypothesized the increased solubility effect would create a stronger surface binding energy, greater than the interlayer van der Waals stacking energy and help exfoliate the layers. In a typical fabrication, CTF powder (5 mg) was immersed in IPA (5 mL) along with either AA or SA (3-5% by vol%). The vials were sonicated for 3 hrs and then the dispersions were centrifuged at 8000 rpm for 5 mins to remove large particulates. Other attempts using a wide variety of neat common solvents such as: IPA, H2O, DMF, NMP, Dioxane, PhMe, DCM, ACN, and acetone were unsuccessful. Recent data has shown the incorporation of non-oxidizing Bronstead acids with graphite causes intercalation and exfoliation in graphite sheets.[27] The mechanism occurs through dipolar interactions of the acids with the polarizable carbon atoms of graphite without partial oxidation, reduction, or modification. Due to structural similarities between graphite and CTF, we suspect a similar intercalation may be occurring with SA and CTF.

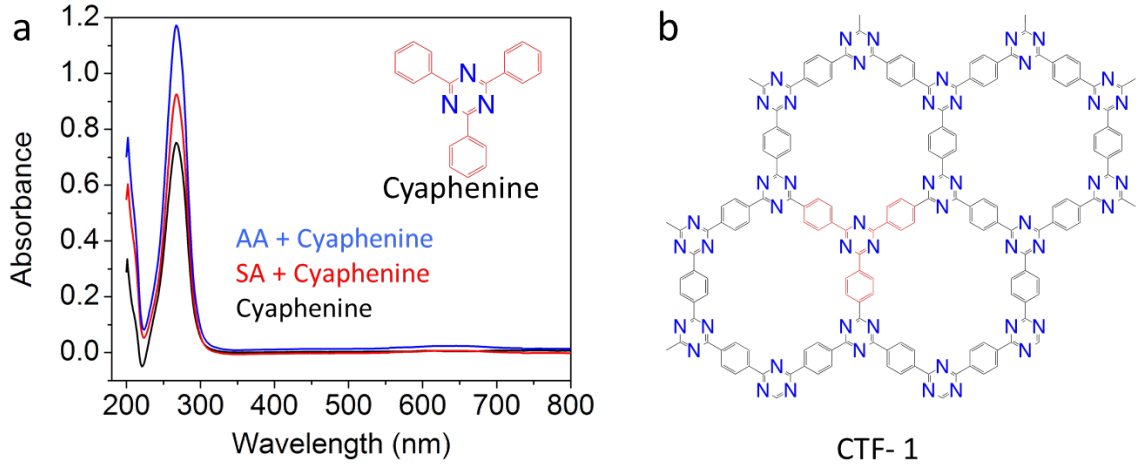

Figure 3.2. UV-Vis absorbance spectrum of Cyaphenine in IPA (a). The structure of Cyaphenine is compared to CTF-1 in (b).

3.3 Results and Discussion

The morphology and local ordering of TNS were investigated using Transmission Electron Microscopy (TEM). The suspensions were drop coated onto carbon-coated TEM grids and observed under 120 kV accelerating voltage. Our samples were stable under these conditions, with no immediate degradation observed during the imaging process. Figure 3.4 shows the influence of adding acid during exfoliations. Using neat IPA, exfoliated CTFs showed the absence of ordered sheets (as displayed in Fig. 3.4a). The addition of AA during exfoliation produced thin-sheet structured CTFs with smooth surface characteristics (Fig. 3.4b). Selected Area Electron Diffraction helped confirm the preserved local order of the thin sheets, displaying clear hexagonal spot patterns along the (001) axis and d-spacings consistent with PXRD on bulk samples. This finding indicates that the CTF thin sheets produced in AA are highly ordered up to the several hundred-nanometer range, a characteristic not previously known from bulk sample PXRD analysis (Figure 3.3). For the sulfuric acid assisted exfoliation, we observed many sheets with large lateral widths in the several micron range. Occasional scrolling of these large sheets

were observed as seen in Figure 4c. Although SAED of these large sheets resulted in polycrystalline diffraction rings, we still observed the presence of clear diffraction spots with d-spacings consistent with PXRD measurements. In both cases the overall crystallinity was maintained throughout exfoliations as observed in SAED patterns.

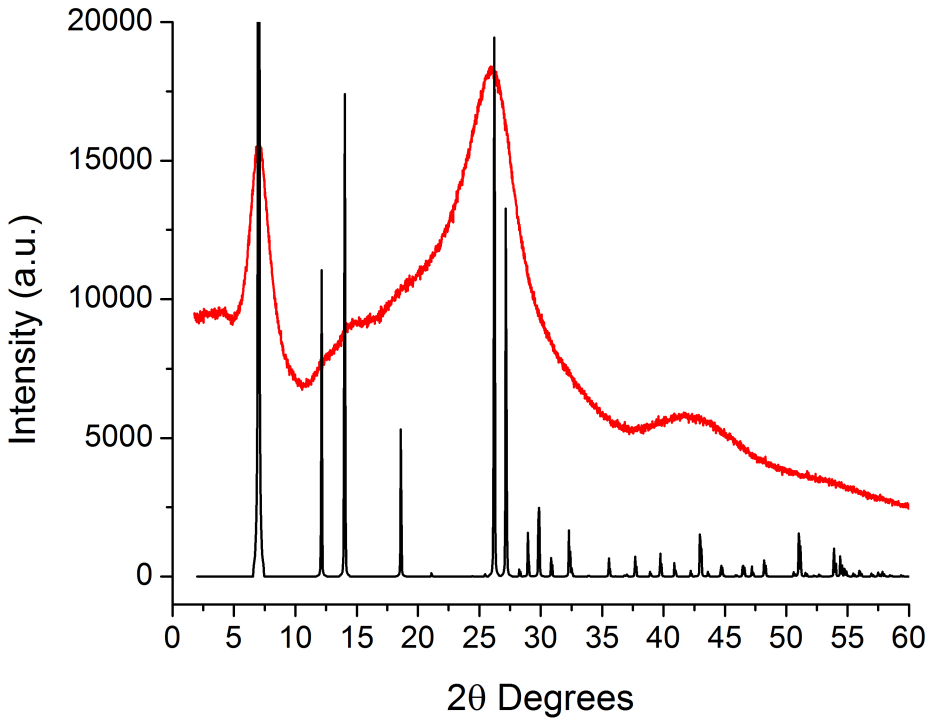

Figure 3.3. PXRD of our as synthesized CTF-1 in red, and simulation pattern in black.

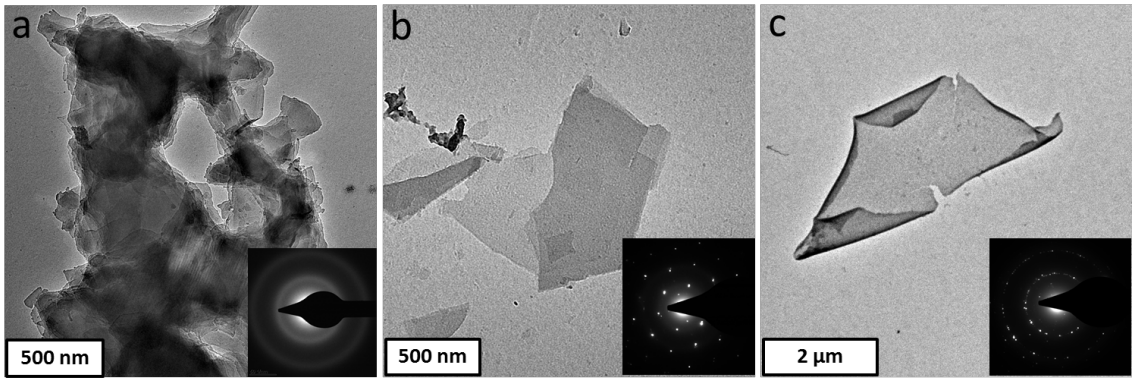

Figure 3.4. TEM images along with SAED patterns of CTF exfoliations in (a) IPA with no acid added, (b) IPA and 5% Acetic Acid and (c) IPA and 3% Sulfuric Acid

The sheet thicknesses and topology were determined using Atomic Force Microscopy (AFM) measurements. Suspensions were prepared by drop casting the TNS onto Si wafers (with 300nm SiO_2 layer on top). Figure 3.6a displays an AA exfoliated sheet with step height of 12 nm. Many sheets as thin as 4 nm were observed for AA assisted exfoliation, however with smaller lateral widths as seen in Figure 3.7. SA assisted exfoliations were able to yield CTF sheets as thin as 3 nm, as seen in Fig 3.6b. Our data exhibits the SA solution is effective at exfoliating maximum lateral sheet size with minimal sheet damage and scissoring. Large area scans were performed to obtain step height distributions and gain a broader scope of our exfoliations (Figure 3.6e & 3.6f). The structural morphology of these TNS can be observed in our scanning electron micrographs (SEMs) for both exfoliation methods. We observed the presence of distinct terraces Figure 3.8 and 3.9, clearly displaying different layers of the TNS.

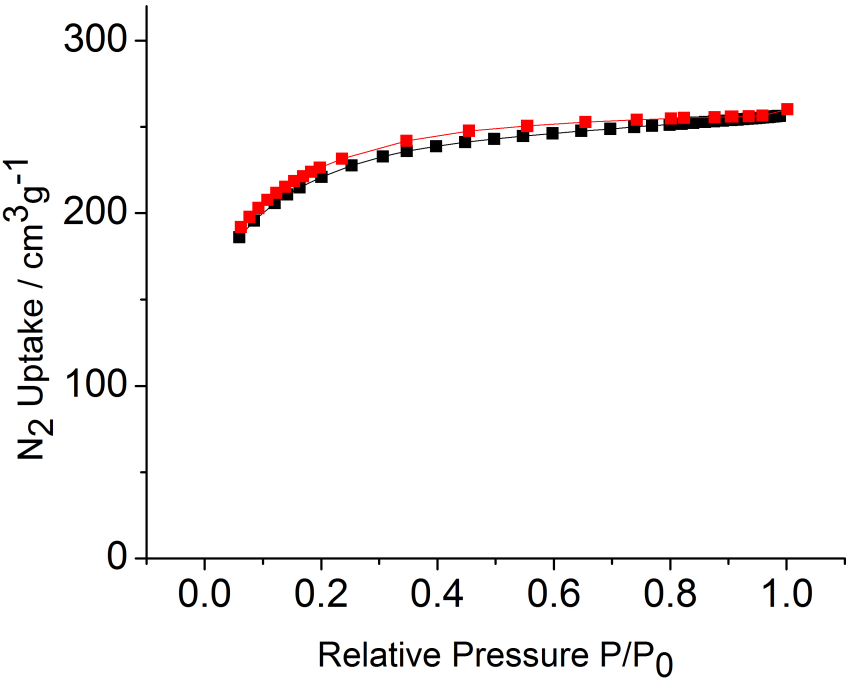

Figure 3.5. Nitrogen absorption isotherm of CTF-1, performed at 77K.

Raman spectra of the exfoliated CTF single sheet were acquired to further confirm their structure and composition, results are shown in Figure 3.10a. We observed the presence two main peaks: 1580 cm^{-1} and 1350 cm^{-1}, which overlap correspondingly to that of G and D bands of graphene. These peaks are consistent to in-plane vibrational modes of conjugated benzene rings, and a separate in-plane vibrational mode respectively.[9] The presence of the G peak confirms the 2D honeycomb pore structure of CTFs; which indicates the overall structural integrity has been preserved through the exfoliation process. The broadness of these peaks may be due to the overlap of -C=N- bond vibrations of the s-triazine rings, which occur in the same region of -C=C- at ~1580

cm^{-1}. Our Raman measurements agree well with the previous reported spectrum on bulk CTF.[28]

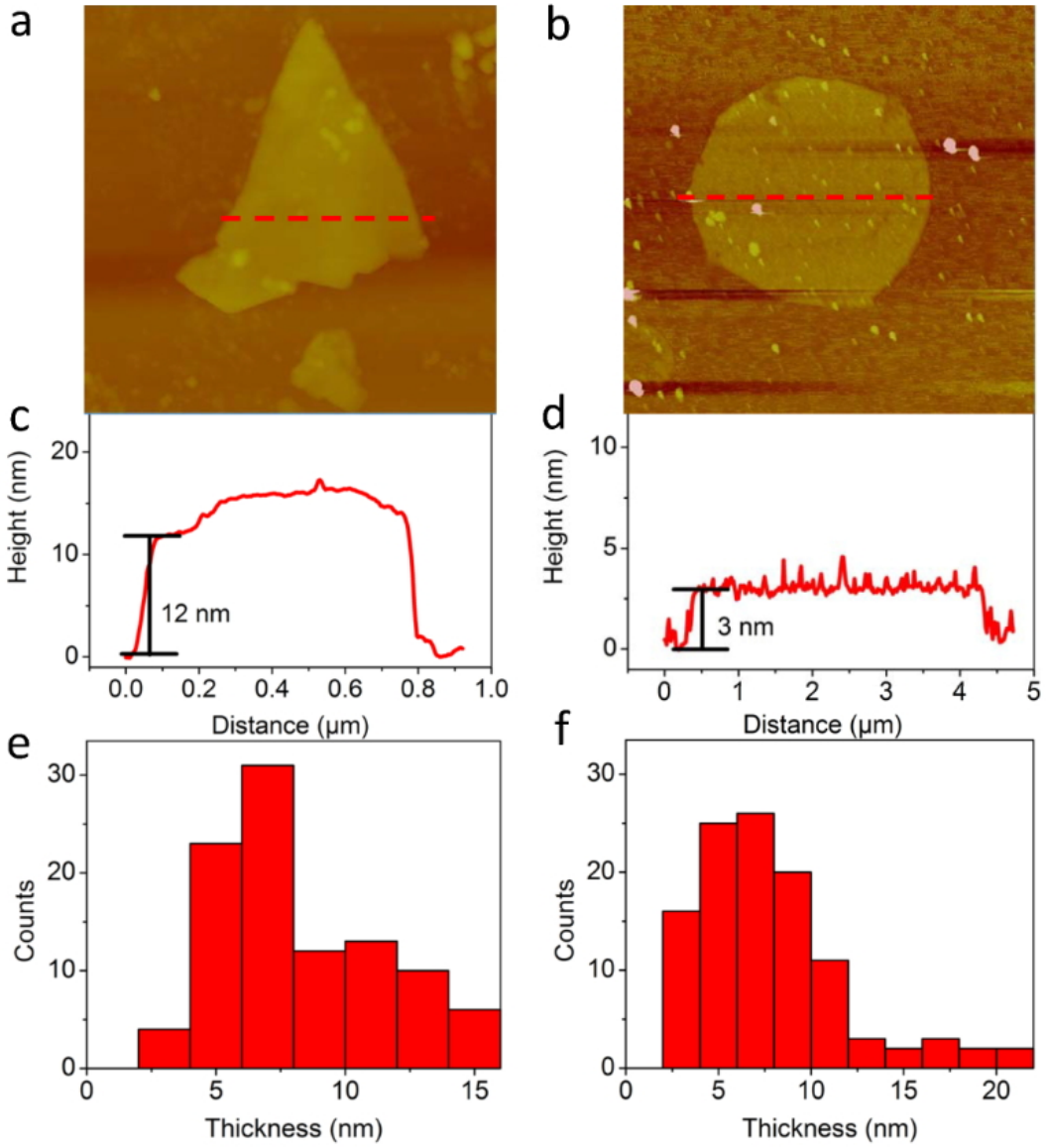

Figure 3.6. AFM height images (a,b) and along with section height profiles in (c,d). Corresponding sheet thickness count distribution graphs are displayed in (e,f).

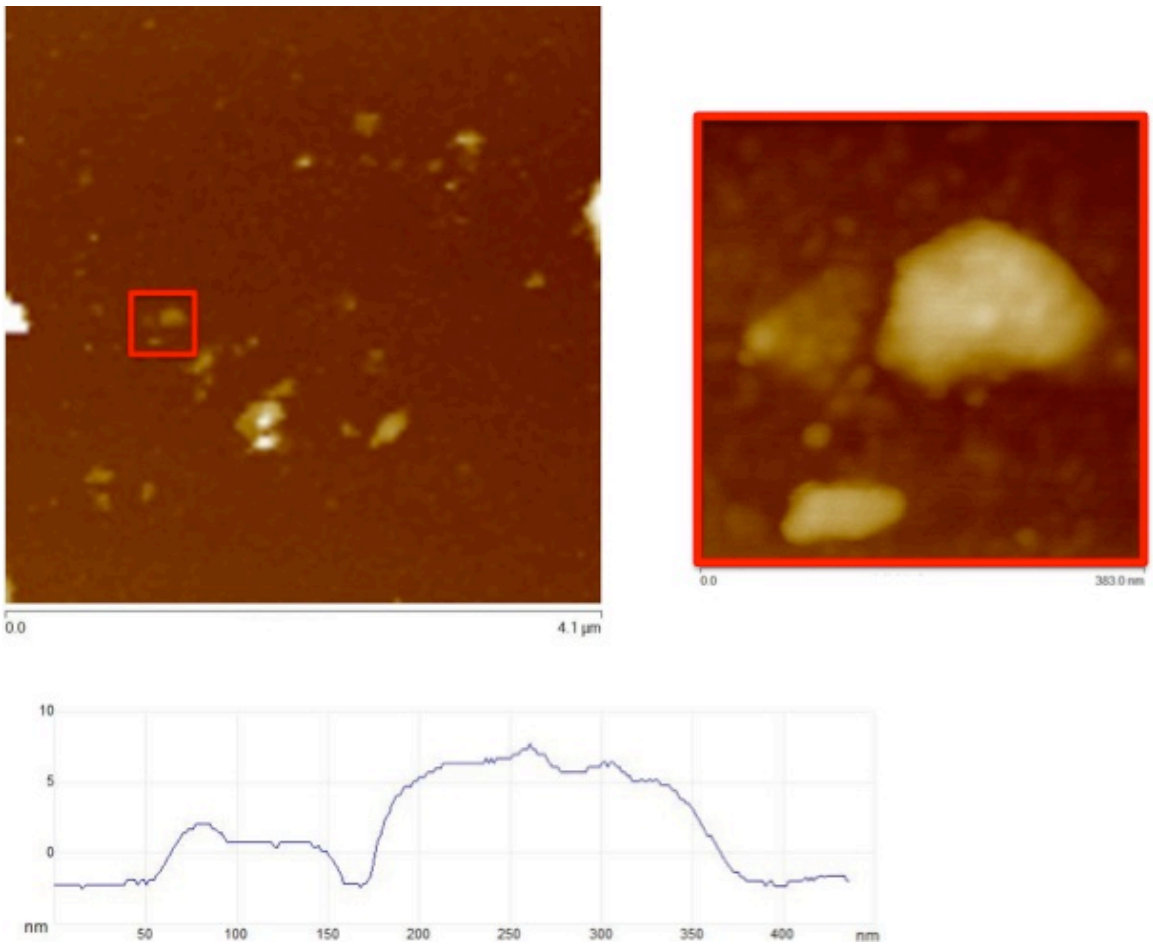

Figure 3.7. Atomic force micrographs of large area scans using AA-TNS

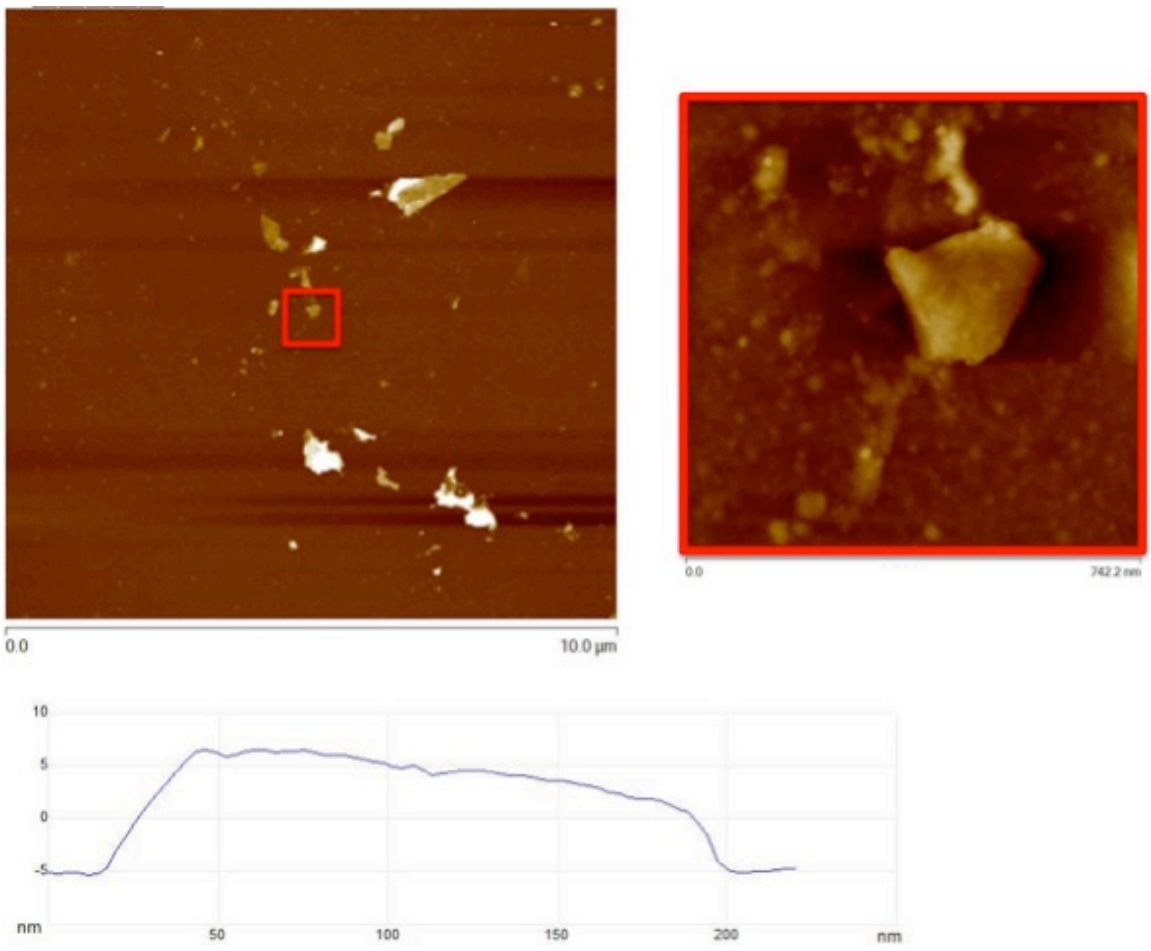

Figure 3.8. Atomic force micrographs of large area scans using SA-TNS

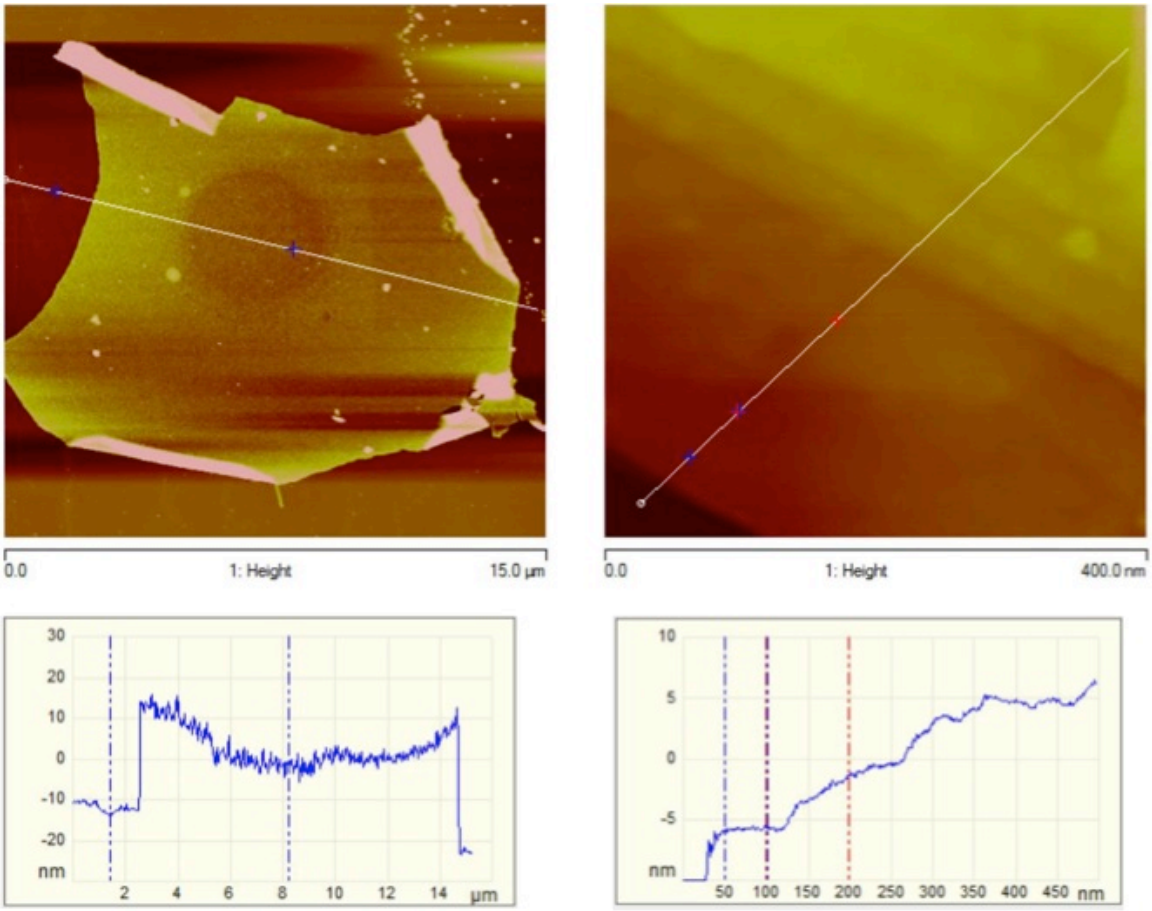

Figure 3.9. Additional atomic force micrographs of large sheets of SA exfoliated TNS on the left, and an edge micrograph displaying different layers on the right.

Further identification of CTF-NS composition was confirmed using FTIR spectroscopy. (Fig 3.10b). There is little variation observed from our bulk material in comparison with exfoliated sheets. Characteristic peaks at 1507cm^{-1}, and 1352 cm^{-1} identify the perseverance of intact triazine rings. FTIR signal stretches appeared sharper, due to the improved transmittance of thin sheets. SA exfoliations gave TNS with micron-sized lateral width making them suitable for gold electrode deposition and device measurements.

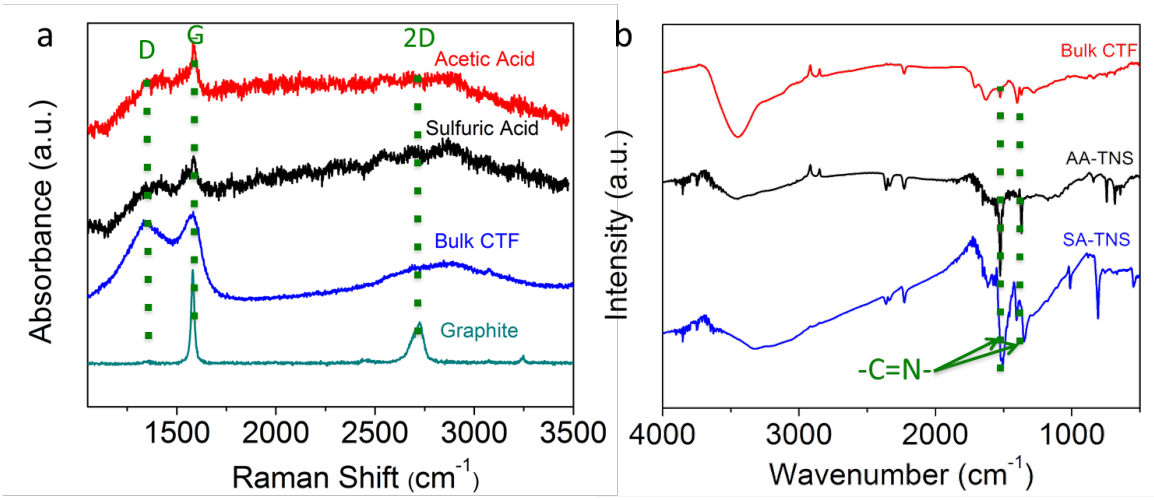

Figure 3.10. Raman spectra of different acid exfoliated CTF-1. Bulk CTF-1 was measured as a control sample, and graphite measured for comparison (a). FTIR spectra of bulk CTF along with exfoliated samples. C=N ring stetches remain well intact (b).

CTF is a conductive polymer material due to its conjugated structures along the 2D basal plane with previously reported conductivity of 4.09X10^-6 S/cm.[9] However, conductivity of a single nano-sheet of CTF has not yet been measured. Using the directly evaporated gold electrodes on the bulk piece of CTF material (Au thickness > surface roughness of CTF piece), we have measured the electrical property of bulk CTF, while the same electrical measurements were also carried out for thick layer (film) and exfoliated thin layer of CTF-NS through the fabrication of corresponding microelectronic devices. Respective results are shown in Figure 3.11. The bulk CTF appeared to be not very conductive, with a resistivity of ~1x10^{-5} S/m (I-V shown in Fig. 3.11a inset). However, after exposure to HCl vapors, the doped CTF afforded a room-temperature conductivity of ~1x10^{-3} S/m as seen in Fig. 11a. For the TNS, a relatively thick film of (from IPA exfoliation Fig 3.11b) was firstly prepared by drop-casting the suspension onto a Si wafer, and then lithographically patterned gold electrodes were evaporated onto the

film. The conductivity of such film of TNS was measured to be ~$2x10^{-5}$ S/m, with a similar increase to ~$5x10^{-5}$ S/m. More interestingly, electrical measurement of a single TNS was achieved due to our successfully developed exfoliation approach. As shown in Fig. 3.11c, the as-prepared single TNS device appeared to be insulating under ambient conditions, after HCl doping, an obvious barrier probably caused by the TNS-metal contact was observed, and a conductivity of $7x10^{-6}$ S/m was obtained at the high voltage region. We noticed a decreasing trend of conductivity from the bulk material to the exfoliated NS samples, which indicates an increasing amount of defect sites on the CTF basal plane due to the exfoliation. To the best of our knowledge, this is the first time the electrical performance of a CTF nanosheet has directly measured, with conductivities similar to other conducting polymers in their undoped state.[29] These findings provide new insight towards the potential use of CTF materials as a promising conductive material, especially the use of exfoliated TNS as an alternative 2-D layered polymer material.

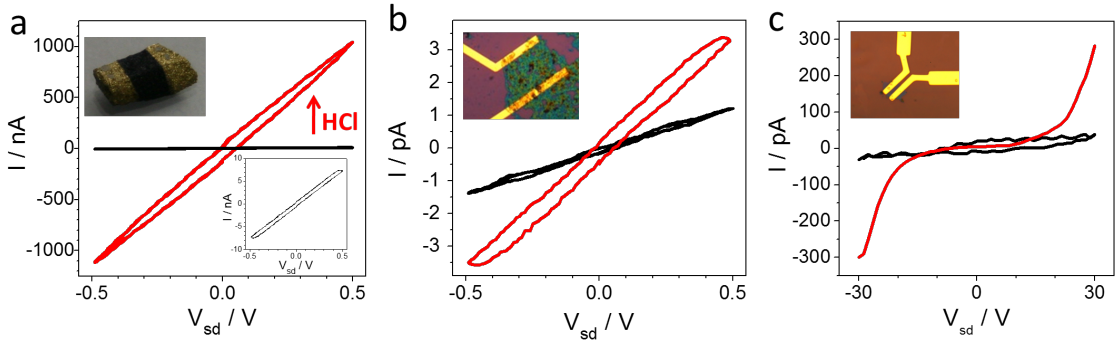

Figure 3.11. Electrical properties of CTF bulk and exfoliated nanosheet materials. (a) I-V curves of bulk CTF-1 with evaporated gold and silver paint contact. Inset depicts the photograph of the measured bulk CTF (top left) and enlarged I-V result of its undoped state. (b) I-V curves of a thick film of IPA exfoliated CTF-NS. Inset depicts an optical image of the device. (c) I-V curves of a single CTF-NS device from sulfuric acid exfoliated CTF. Inset depicts an optical image of the single sheet device. In all figures, black curves correspond to the undoped state of CTF and red curves correspond to the state of CTF doped by HCl exposure.

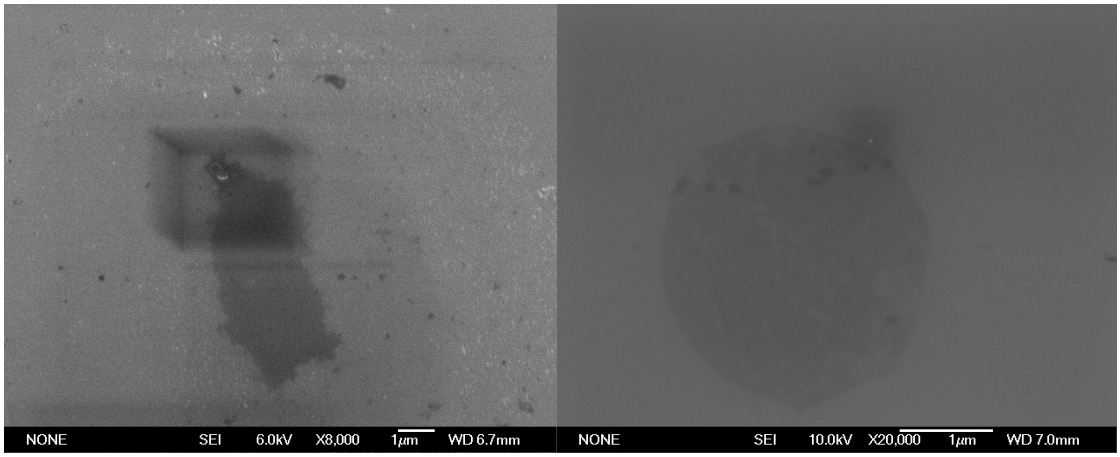

Figure 3.12. Scanning electron micrographs were obtained for our TNS with AA exfoliated on the left, and SA exfoliated on the right. The presence of dark squares are due to charge accumulation on the SiO2 wafer during sample acquisition.

3.4 Conclusion

In summary, TNS have been prepared using two simple methods, and characterized their thin-sheet attributes. We observed no loss in crystallinity and structural bonds by SAED and FTIR. The laminar morphology of these sheets were clearly observed under TEM and SEM. Our methods were able to produce stable dispersions of CTF nanosheets with large aspect ratios. These findings open a new strategy to the creation thin 2D organic polymer sheets which posses more complex chemistry in their layered state, and open CTFs to a wide range of potential applications from electronics, optics, to possible restructured 3D architectures.

3.5 References

1.) Kuhn, P., Antonietti, M., Thomas, A. *Angew. Chem. Int. Edit.* **2008**, *47*, 3450-3453.

2.) Katekomol, P., Roeser, J., Bojdys, M., Weber, J., Thomas, A. *Chem. Mat.* **2013**, *25*, 1542-1548.

3.) Bhunia, A., Vasylyeva, V., Janiak, C. *Chemical Communications* **2013**, *49*, 3961-3963.

4.) Bojdys, M. J., Jeromenok, J., Thomas, A., Antonietti, M. *Adv. Mater.* **2010**, *22*, 2202-2205.

5.) Cote, A. P., Benin, A. I., Ockwig, N. W., O'Keeffe, M., Matzger, A. J., Yaghi, O. M. *Science* **2005**, *310*, 1166-1170.

6.) Yaghi, O. M., O'Keeffe, M., Kanatzidis, M. *J. Solid State Chem.* **2000**, *152*, 1-2.

7.) Yaghi, O. M., O'Keeffe, M., Ockwig, N. W., Chae, H. K., Eddaoudi, M., Kim, J. *Nature* **2003**, *423*, 705-714.

8.) Chan-Thaw, C. E., Villa, A., Katekomol, P., Su, D. S., Thomas, A., Prati, L. *Nano Lett.* **2010**, *10*, 537-541.

9.) Sakaushi, K., Hosono, E., Nickerl, G., Gemming, T., Zhou, H. S., Kaskel, S., Eckert, J. *Nat. Commun.* **2013**, *4*, 7.

10.) Sakaushi, K., Nickerl, G., Wisser, F. M., Nishio-Hamane, D., Hosono, E., Zhou, H. S., Kaskel, S., Eckert, J. *Angew. Chem. Int. Edit.* **2012**, *51*, 7850-7854.

11.) Hao, L., Ning, J., Luo, B., Wang, B., Zhang, Y. B., Tang, Z. H., Yang, J. H., Thomas, A., Zhi, L. J. *J. Am. Chem. Soc.* **2015**, *137*, 219-225.

12.) Zhao, Y. F., Yao, K. X., Teng, B. Y., Zhang, T., Han, Y. *Energy Environ. Sci.* **2013**, *6*, 3684-3692.

13.) Geim, A. K., Novoselov, K. S. *Nat. Mater.* **2007**, *6*, 183-191.

14.) McCain, M. N., He, B., Sanati, J., Wang, Q. J., Marks, T. J. *Chem. Mat.* **2008**, *20*, 5438-5443.

15.) Bunck, D. N., Dichtel, W. R. *J. Am. Chem. Soc.* **2013**, *135*, 14952-14955.

16.) Yang, S. B., Gong, Y. J., Zhang, J. S., Zhan, L., Ma, L. L., Fang, Z. Y., Vajtai, R., Wang, X. C., Ajayan, P. M. *Adv. Mater.* **2013**, *25*, 2452-2456.

17.) Chandra, S., Kandambeth, S., Biswal, B. P., Lukose, B., Kunjir, S. M., Chaudhary, M., Babarao, R., Heine, T., Banerjee, R. *J. Am. Chem. Soc.* **2013**, *135*, 17853-17861.

18.) Xue, T. *et al. Nat. Commun.* **2014**, *5*, 6.

19.) Liao, L. *et al. Nature* **2010**, *467*, 305-308.

20.) Xu, Y. X., Lin, Z. Y., Zhong, X., Huang, X. Q., Weiss, N. O., Huang, Y., Duan, X. F. *Nat. Commun.* **2014**, *5*, 8.

21.) Xue, T. *et al. Angew. Chem. Int. Edit.* **2012**, *51*, 3822-3825.

22.) Hu, H., Zhao, Z. B., Wan, W. B., Gogotsi, Y., Qiu, J. S. *Adv. Mater.* **2013**, *25*, 2219-2223.

23.) Li, D., Muller, M. B., Gilje, S., Kaner, R. B., Wallace, G. G. *Nat. Nanotechnol.* **2008**, *3*, 101-105.

24.) Coleman, J. N. *et al. Science* **2011**, *331*, 568-571.

25.) Halim, U., Zheng, C. R., Chen, Y., Lin, Z. Y., Jiang, S., Cheng, R., Huang, Y., Duan, X. F. *Nat. Commun.* **2013**, *4*, 7.

26.) Ogata, Y., Izawa, Y., Kawashim.Y. *Bull. Chem. Soc. Jpn.* **1965**, *38*, 777-778.

27.) Kovtyukhova, N. I., Wang, Y. X., Berkdemir, A., Cruz-Silva, R., Terrones, M., Crespi, V. H., Mallouk, T. E. *Nat. Chem.* **2014**, *6*, 957-963.

28.) Sakaushi, K., Nickerl, G., Kandpal, H. C., Cano-Cortes, L., Gemming, T., Eckert, J., Kaskel, S., van den Brink, J. *J. Phys. Chem. Lett.* **2013**, *4*, 2977-2981.

29.) MacDiarmid, A. G. *Angew. Chem. Int. Edit.* **2001**, *40*, 2581-2590.

Chapter 4

Covalent Triazine Frameworks a Support Electrocatalysts

4.1 Introduction

As we move towards increasing renewable energy sources, new challenges arise on how to store the excess energy and re-harvest it back. High performance electrocatalysts may help fulfill these roles, more specifically those that perform oxygen reduction reaction (ORR) and hydrogen reduction reaction (HER). Earth abundant, low-cost, efficient, and stable are the main prerequisites to fulfilling these challenges.

In a typical regenerative fuel cell (RFC), an electrolyzer stores energy by splitting water into H_2 and O_2, and a fuel cell converts the chemical energy into electrical energy. In a unified regenerative fuel cell (URFC) a single module serves the dual purposes of electrolyser and fuel cell, where they utilize bi-functional catalysts for both electrolysis and energy conversion. This design efficiency not only saves components, but also materials, space, and costs[1].

Recently, CTFs have been shown to be novel platforms for electrocatalyts[2-3]. However, to obtain good electrochemical performance, there was a need to blend with carbon due to their inherent low conductivities. Though this was a solution, it has the added effect of lowering the number of active catalyst per area and weight. Here we synthesized CTF-Co, a cobalt-loaded CTF-derived material derived from super-acid polymerized triazine films[4]. The resultant polymer when immersed into a cobalt solution can strongly chelate the metal. After high temperature annealing, the resultant CTF-Co posses desired electrochemical properties of: intrinsic conductivity, high surface area, nitrogen doping, and transition metal binding.

The CTF and cobalt play synergistic roles for each other. Cobalt aids in the graphitization of the CTF, helping the framework achieve metallic-like conductivities, as

well as remaining an active catalyst to enhance ORR and HER. The CTF upon graphitization now acts as an ideal electro-catalytic support; aiding the cobalt with surface area, diffusion, and electron transport across the 3D framework.

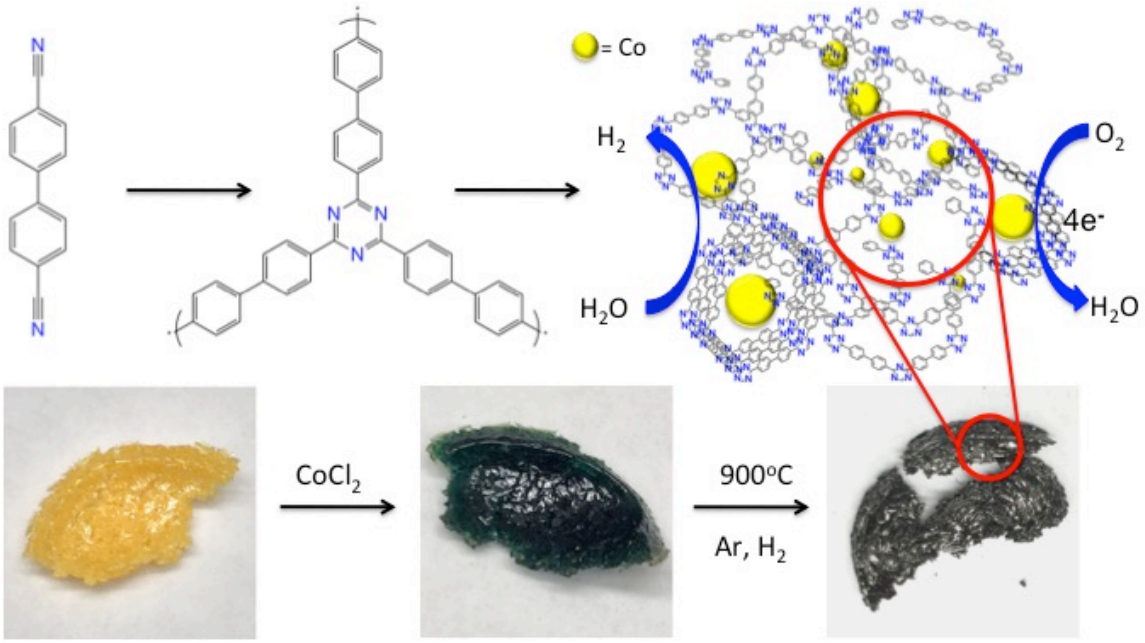

Scheme 4.1. Trimerization of BPDC into a triazine polymer. Upon metal chelation the and annealing the structure becomes disordered and contains cobalt particles. Photographs of the transition from polymer, to metallation, and finally annealing are displayed.

4.2 Experimental

CTF-Co was produced using a metal-binding followed by high-temperature treatment. Polymerized CTF was prepared under typical conditions (reference) and was immersed into a cobalt chloride and ethanol solution at 60^{o}C overnight, allowing for metal chelation. The CTF turned blue indicating metal binding. The sample was washed with ethanol to remove any excess cobalt then annealed under Ar and H_2 gas at 900^{o}C for 2 hrs. Other annealing temperatures 700, 800, 1000, were tested however 900^{o}C yielded the highest ORR performance. So for further discussion, unless stated otherwise all

samples were treated under 900°C temperature. To our knowledge, this is the first case CTFs synthesized from super acid have been shown to be able to absorb metal atoms from solution. This finding may lead to further applications of super-acid CTFs in membranes purifications.

4.3 Results and Discussion

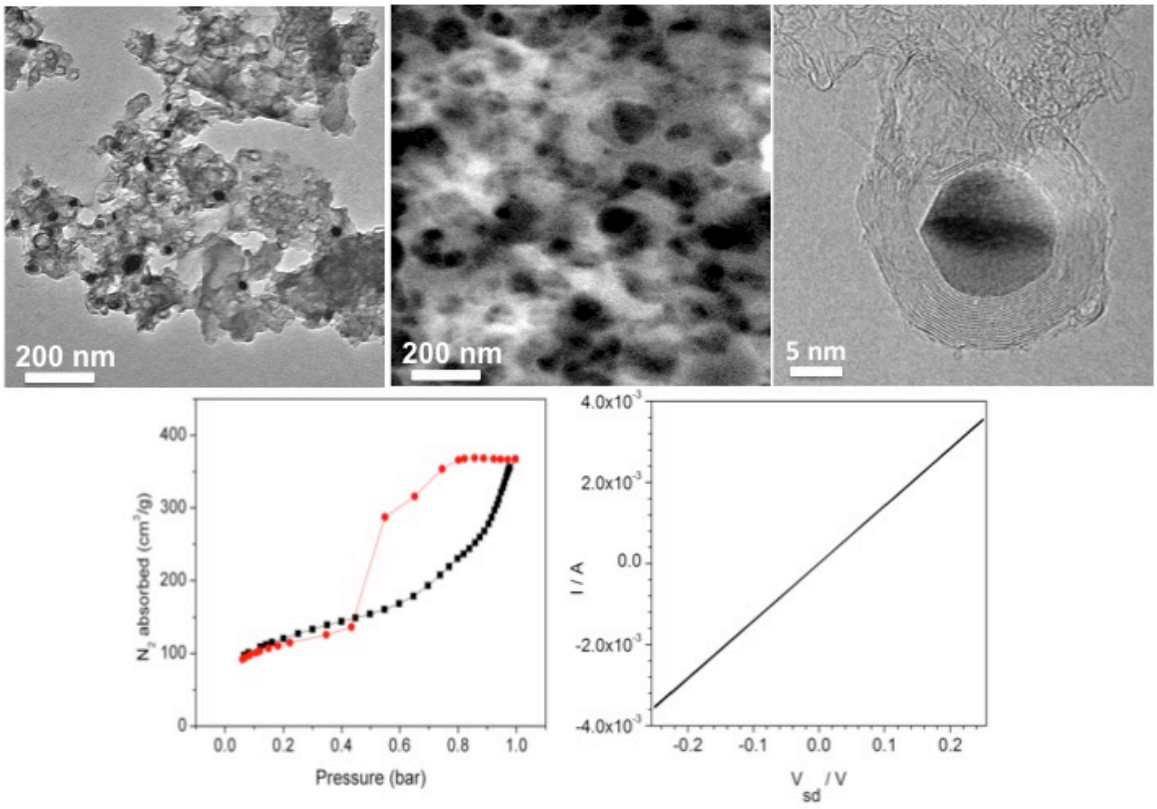

Figure 4.1. Low magnification TEM of CTF-Co (a). SEM of CTF-Co showing large cavernous pores (b). HR-TEM image of graphitically wrapped cobalt nanoparticle (c). BET nitrogen isotherm of CTF-Co (d). Black curve represents absorption, red curve represents desorption. I-V curve performed on bulk sample of CTF-Co (e).

The 3D CTF-Co structure and morphology were examined by transmission electron microscopy and scanning electron microscopy (SEM) (Figure 4.2 a and b).

Hollow mesopores are easily visible throughout the structure along with uniformly distributed cobalt nano-crystals (NC). Figure 4.2a displays a typical TEM image of the CTF-Co. The SEM images show the mesoporous channels of CTF-Co are interconnected with micron-length oligomers that continuously run throughout the structure in Figure 4.2b. High-Resolution TEM and XRD (Figure 4.2c and Figure S1) identified the cobalt to be highly crystalline fcc, with d-spacings of 2.04 Å corresponding to the (111) facet. These graphitically wrapped cobalt particles have been shown previously to dramatically improve ORR performace(). Nitrogen absorption analysis gave a specific surface area of 560 m^2/g as seen in Figure 4.2d. A typical type IV isotherm was observed, a typical characteristic of mesoporous materials. Encouraged by the evidence of 3D conjugation, we measured a bulk centimeter sized sample using vapor deposited gold electrodes. The sample can be seen in Figure S2. We obtained a conductivity of 20 S/cm at room temperature which puts CTF-Co amongst the best organic conductors(ref) including TTF*TCNQ (pellet conductivity 10 S/cm)(ref). We believe the presence of cobalt NCs aided in the graphitization and therefore conductivity enhancement(ref), since non-cobalt thermally annealed CTFs gave a lower conductivity of 1×10^{-3} S/cm. Our Raman studies help support this through comparison of honeycomb-graphitic in-plane D and G band vibrations intensities at 1350 cm^{-1} and 1580 cm^{-1} respectively in Figure S3. There is a significant signal to sample enhancement of several times when using equal amounts of CTF, loaning to enhanced graphitization of cobalt containing CTF.

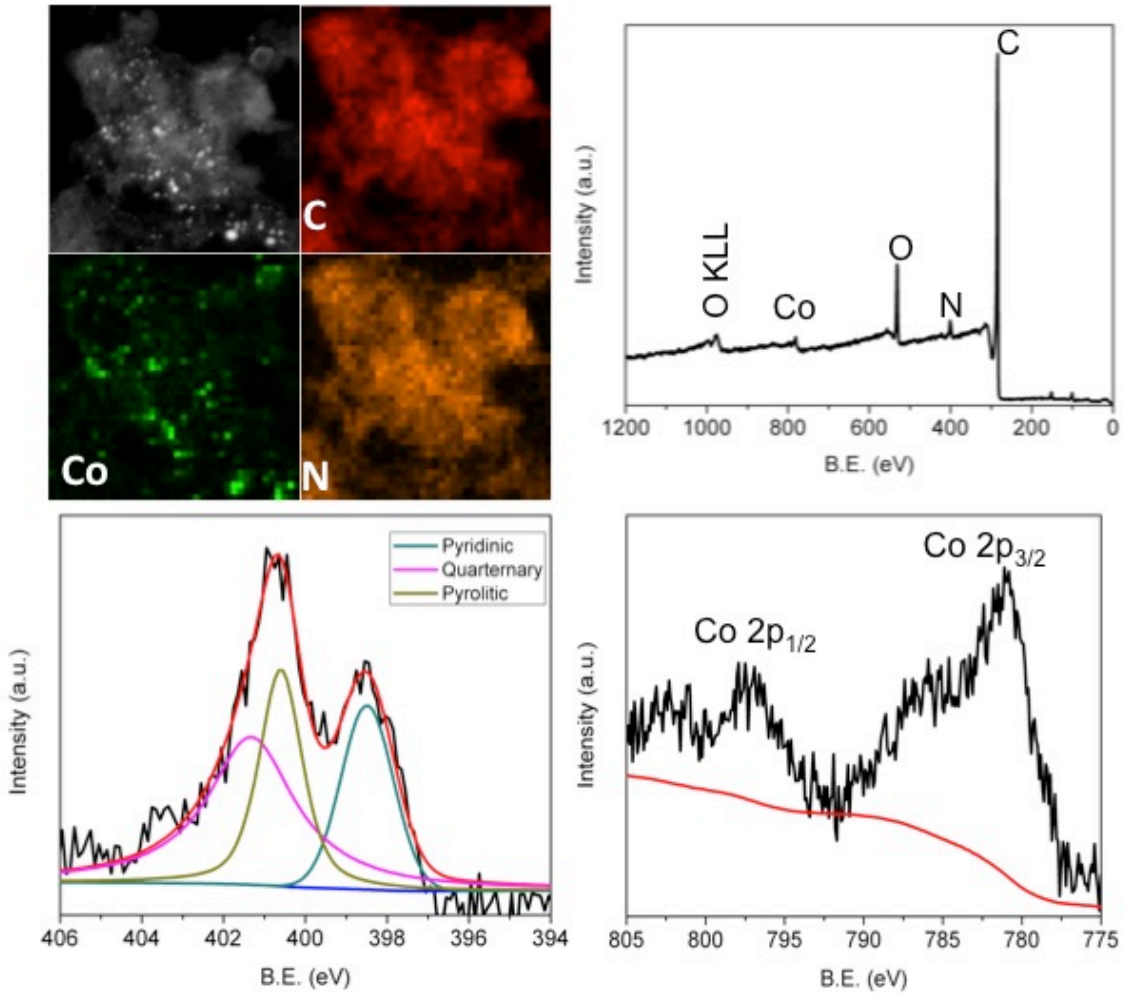

Figure 4.2. EDAX mapping of CTF-Co is displayed (a). XPS Survey spectrum of CTF-Co (b). Nitrogen 1S displays different types of nitrogen bondings (c) and Cobalt 2P spectrum displays cobalt ion peaks (d).

To investigate the elemental composition of CTF-Co, energy-dispersive X-ray spectroscopy (EDS) mappings were performed on CTF-Co. Nitrogen atoms are clearly and uniformly distributed throughout the framework giving strong signals. Cobalt NC are also seen to be well dispersed through the framework (Figure 4.3a).

X-ray photoelectron spectroscopy (XPS) not only further confirms our nitrogen and cobalt content, but also the bonding environments and oxidation states (Figure 4.3b-d). Our nitrogen N1S spectrum after annealing of CTF-Co (Figure 4.3c) can be de-

convoluted into three peaks at: 398.6, 400.5, and 401.3 eV. These peaks correspond to pyridinic, pyrrolic, and quaternary nitrogens respectively. There was some typical nitrogen loss from pyrolization, where the content decreased from theoretical 13.5% to ~11.8% analyzed using elemental analysis. Our Cobalt XPS displays peaks correlating to cobalt $^{2+/3+}$ ions. We presume this signal is due to catalytic sites of cobalt chelated in Co-N fashion to pyridinic and pyrrolic nitrogens throughout the framework, which is responsible for our bi-catalyst properties (ref). Inductive coupled plasma (ICP) analysis revealed our cobalt content to be ~11%. Our results indicate CTF-Co maintains its nitrogen group functionality throughout the annealing process, and does not require the dangers of ammonia treatment to introduce nitrogen doping which has been shown to be important for enhancing ORR performance. Furthermore, through this intrinsic nitrogen-containing framework, we are able to reach high amounts of nitrogen, not easily obtained through doping.

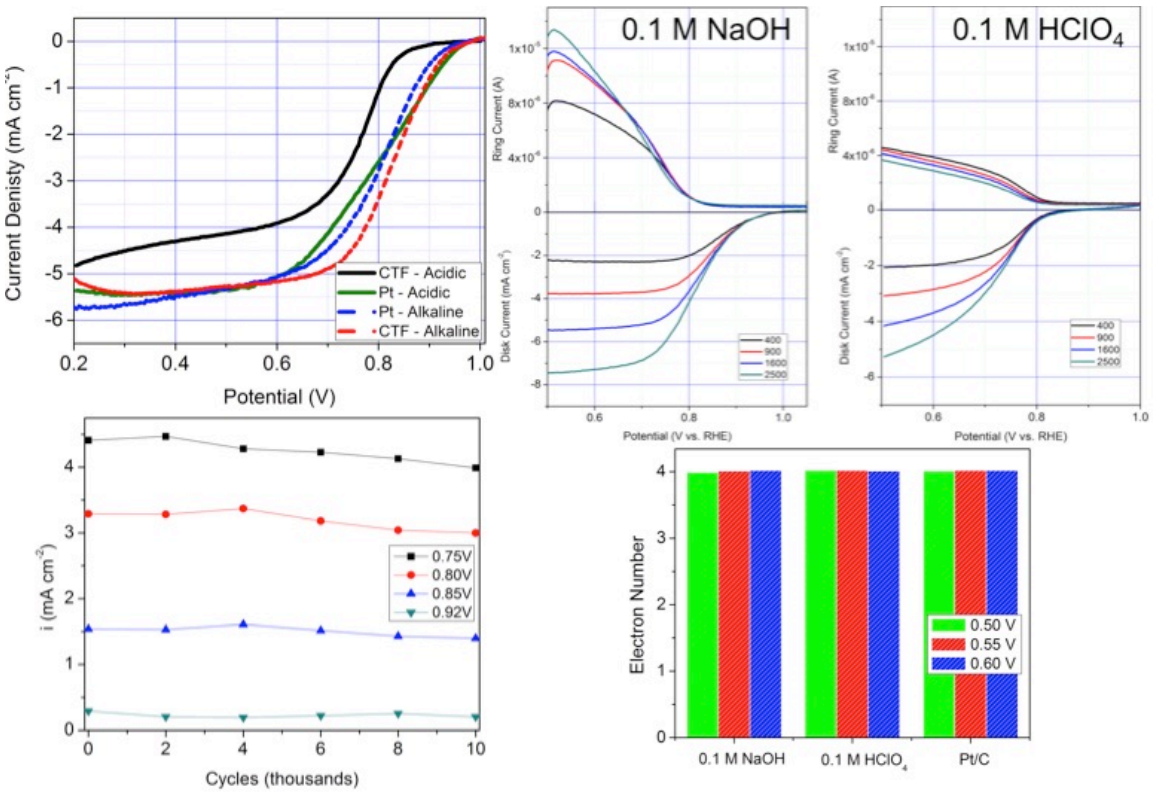

Figure 4.3. Different LSV curves of CTF-Co in both acidic and basic electrolyte, along with Pt/C as a comparison (a). RRDE in both acidic and basic electrolytes displaying LSV and peroxide currents at different rotation speeds (b). Stability measurements plotted by number of cycles along with change in current (c). Electron transfer numbers bar graph of CTF-Co in both acidic and basic electrolytes, with Pt/C as a comparison (d).

The ORR activities of CTF-Co were performed using a rotating-disk electrode (RDE) under acidic and alkaline electrolytes and rotating ring-disk electrode (RRDE) for catalytic pathway determination. LSV curves were taken at a scan rate of 10mV/s in both electrolytes with overlay comparisons to commercial 20% Platinum on Vulcan carbon (Pt/C) standards are shown in Figure 4a. In acidic conditions, CTF-Co gave an onset potential (E_{onset}) of 0.9 V vs. RHE and diffusion limiting current density of 4 mA/cm at 0.6 V. Under alkaline conditions, CTF-Co outperforms Pt/C. We measured an E_{onset} of 0.98 V and a half-wave potention ($E_{1/2}$) at 0.82V, which at this point surpasses that of

Pt/C by over 10 mV. Morevoer, CTF-Co has a near 70 mV cathodic shift when comparing at 5 mA limiting current using 0.7 V potential.

Though we do observe some ORR with non-cobalt treated CTF, it resulted in significantly larger overpotential (~200mV) in comparison CTF-Co.

RRDE measurements were performed under the same conditions with a scan rate of 10 mV/s in their appropriate electrolytes. We detected extremely low peroxide oxidation currents, in the micro-amp range, as seen in Figure 4.4b. Our calculations by equation (Figure S#) reveal the peroxide percentages to be below 0.1% throughout the limiting current. Calculating the electron transfer number (n) from these values attributes CTF-Co to near total 4e- reduction of oxygen by CTF-Co in both alkaline and acidic conditions (Figure 4d). Our catalyst durability was tested by cycling CTF-Co in O2-saturated 0.1M KOH for up 10,000 cycles. We obtained this comparing data points along the onset potential to limiting current and found only minor degradation as seen in (Figure 4.4c).

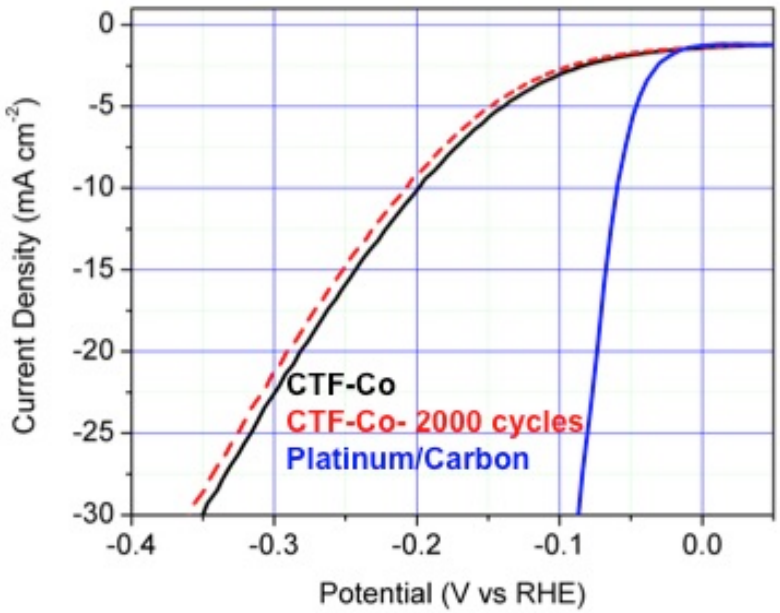

Catalyst	Electrolyte	Scan Rate	Overpotential for 10 mA cm^{-2}	Reference
CTF-Co	0.5M H_2SO_4	5 mV s^{-1}	200 mV	This work
N-CO@G	0.5M H_2SO_4	5 mV s^{-1}	265 mV	1a
C_3N_3@NG	0.5M H_2SO_4	5 mV s^{-1}	240 mV	2a
FeCo@NCNTs-NH	0.5M H_2SO_4	2 mV s^{-1}	290 mV	3a
Defect-rich MOS_2	0.5M H_2SO_4	5 mV s^{-1}	190 mV	4a
Mo_2C	1M H_2SO_4	1 mV s^{-1}	215 mV	5a

Figure 4.4. LSV of CTF-Co in black, along with stability after 2000 cycles in red. Pt/C added for comparison in blue. (a) Comparison chart of different transition metal based HER catalysts along with CTF-Co (b).

We evaluated the function of CTF-Co towards HER under the standard conditions of 0.5M H_2SO_4 and a typical three-electrode system. A standard loading mass of 285 μg cm^{-2} on glassy carbon electrode rotating at 2000 rpm was used. For comparison, commercial Pt/C @ 20 wt % was loaded on the working electrode in the same mass amount. CTF-Co begins HER at an onset potential of ~70 mV as seen in the polarization

curves of Figure 4.5a, overlaid with Pt/C standard whose onset is near zero. At 10 mA of current density, the customary comparison point for HER catalysts, CTF-Co operates at only 200 mV overpotential. This activity is comparable, and even surpasses many other non-nobel metal catalysts as shown in Table 1. To test the long-term resilience of CTF-Co for sustained HER, cyclic-voltammetry was continuously performed from 0.2 to -0.5V vs RHE in 0.5M H_2SO_4 for two-thousand cycles. Only a slight overpotential increase of ~8 mV was observed after this, as seen in Figure 4.5A. The small differences in the stability curves for both ORR and HER show CTF-Co to be a robust candidate for long term URFC catalyst.

4.4 Conclusion

In summary we have synthesized a new, very conductive 3D framework, which contains transition metal cobalt and performs two very important electro-catalytic reactions, ORR and HER with good performance. The framework, CTF-Co, contains a wide range of pores, ranging from micro to mesoporous, many are large enough to observe under SEM. This translates into highly accessible surface area, which optimizes diffusion attributing to CTF-Co's high performance. Our studies show the synergistic behavior between CTF and Cobalt in where they compliment each other in a thermal reaction to produce conductive 3D materials, whose future applications may also be utilized in sensing, devices, and batteries. Our novel bi-functional catalyst advances the applicability of CTFs as supports for water splitting and fuel cell applications.

4.5 References

1.) Cameron, D. S. *Platin. Met. Rev* **2011**, *55* (2), 108.

2.) Kamiya, K.; Kamai, R.; Hashimoto, K.; Nakanishi, S. *Nat. Commun.* **2014**, *5*, 1.

3.) Hao, L.; Zhang, S.; Liu, R.; Ning, J.; Zhang, G.; Zhi, L. *Adv. Mater.* **2015**, *27* (20), 3190.

4.) Brown, S.; Veith, G. M.; Luo, H.; Liu, H.; Dai, S. **2012**.

Chapter 5

Molecular Tuning of

Covalent Triazine Frameworks

for Pore Size Control

5.1 Introduction

Oxygen reduction reaction (ORR) is of essential importance for energy conversion technologies involving fuel cells, water splitting, and batteries[1]. Much efforts have been dedicated to the development of high performance transition-metal based catalyst as a cost-effective replacement of industrial Pt/C[2-4]. Porous frameworks have been widely applied for the suspension of transition-metal catalyst for ORR, many with performances comparable to Pt/C or even surpassing it[5-11]. Porous carbons, which are often nitrogen and metal doped, were originally employed as the support for catalysts to facilitate their ORR activities[10,12]. Recently, chemically synthesized frameworks, such as MOFs[13], carbon nanotubes (CNTs)[14], and covalent-organic frameworks (COFs)[15], have been used as precursors to serve as next generation composite of catalyst and supports. Catalysts derived from temperature treating these frameworks are very appealing since they possess intrinsically high surface area, abundant nitrogen content, and may contain a variety of metals. Covalent triazine frameworks (CTFs), a subclass of COFs initially developed by Kuhn *et al*[16], have shown a wide range of applications in gas storage[17-19], heterogeneous catalysis[20-22], and energy storage[23-25]. Recently applications of CTFs in ORR have received increasing attentions due to their ability to bind metals, high nitrogen content, and full π-conjugation[26-28]. More specifically, CTFs built from 2,6-dicyanopyridine (DCP) ligand most significantly benefit the catalytic performance since a bipyridine moiety is produced from nitrile trimerizations[29], which create an open site for metal chelation[28].

Among studies on these framework based catalyst support systems, few have considered deeply the importance of porosity details, such as pore volume, surface area, electrochemical surface area, *etc.* Here, we set out to study the principle of pore expansion and its influence on the ORR activity of suspended transition-metal catalyst. Pursuing incremental higher porosity, we synthesized two new CTFs, by adding stoichiometric amounts of either 1,4-dicyanobenzene (DCB), or 4,4-biphenyl dicyanobenzene (BPDC) to the DCP monomer (as illustrated in Scheme 1). Our facile synthetic approach overcomes multiple difficulties of producing high porosity: (i) tedious organic synthesis techniques, (ii) maintaining full conjugation (iii) ability to bind transition-metals. Tuning the pore sizes of CTFs and using them as precursors to annealing, resulted in three robust frameworks which not only maintained sequentially higher specific surface areas, but also successively increasing electrochemical surface areas. Here we study the progressive pore tuning, and report their correlation to oxygen reduction behavior in alkaline electrolyte. We found that the largest pore size electrocatalyst, Co-CTF-L, has exceptional ORR performance, with half-wave over-potential 38 mV lower than that of the commercial Pt/C.

5.2 Experimental

Synthesis of CTFs: CTF-S: 2,6 Dicyanopyridine (DCP) was mixed in a 1:1 molar ratio with anhydrous $ZnCl_2$ (~ 2 grams total weight) and flame sealed in a quartz tube. The tube was placed in a furnace at 400 ^oC for 40 hrs, where then the reaction was opened and the CTF was washed with copious amounts of 1.0 M HCl, THF, and acetone. Synthesis of CTF-M: Monomers in a 1:2 molar mixture of DCP, and 1,4 Benzenedicarbonitrile (DCB) along with equal molar amounts of anhydrous $ZnCl_2$, were flame sealed in a

quartz tube and followed the same post-synthesis procedure above. Synthesis of CTF-L: Monomers in a 1:2 molar mixture of DCP, and 4,4'-Biphenyldicarbonitrile (BPDC) along with equal molar amounts of anhydrous $ZnCl_2$, were flame sealed in a quartz tube and followed the same post-synthesis procedure above.

Synthesis of Co-CTFs. To metallate the CTFs, 40 mgs of desired CTF were immersed in 20 mL of $CoCl_2$/ethanol solution (1 mg/mL). The vial was allowed to react for 24 hrs in which an obvious decoloration occurred. The excess cobalt solution was then decanted, and the remaining CTF washed twice with ethanol then dried in air. The cobalt bound CTFs were then placed into an aluminum boat, and heated in a quartz tube furnace with a gas flow mixture of $Ar:H_2$ (90:10) gas for 2 hrs. To prepare Co-CTFs for electrochemical measurements, the materials were ground into fine powders/paste using a mortar and pestle along with a few drops of ethanol.

Materials Characterization. Transmission electron microscopy (TEM T12 Quick CryoEM) was taken to investigate the overall structure and cobalt particles. High Resolution Transmission Electron Microscopy (HRTEM) was performed using a Titan at 300 kV accelerating voltage. Scanning electron microscopy (Zeiss Supra 40VP) was used to study the morphology of the Co-CTFs. X-ray Diffraction (XRD) was carried out using a Bruker D8 X-ray Powder Diffractometer with Cu Ka radiation. BET Isotherms and pore size data were measured using a Miromeritics Tristar II 3020. X-ray photoelectron spectroscopy (Axis Ultra DLD) was used to probe nitrogen and cobalt contents of each Co-CTF. TGA was carried out to evaluate the cobalt loading amount using PerkinElmer instruments Pyris Diamond TG/DTA.

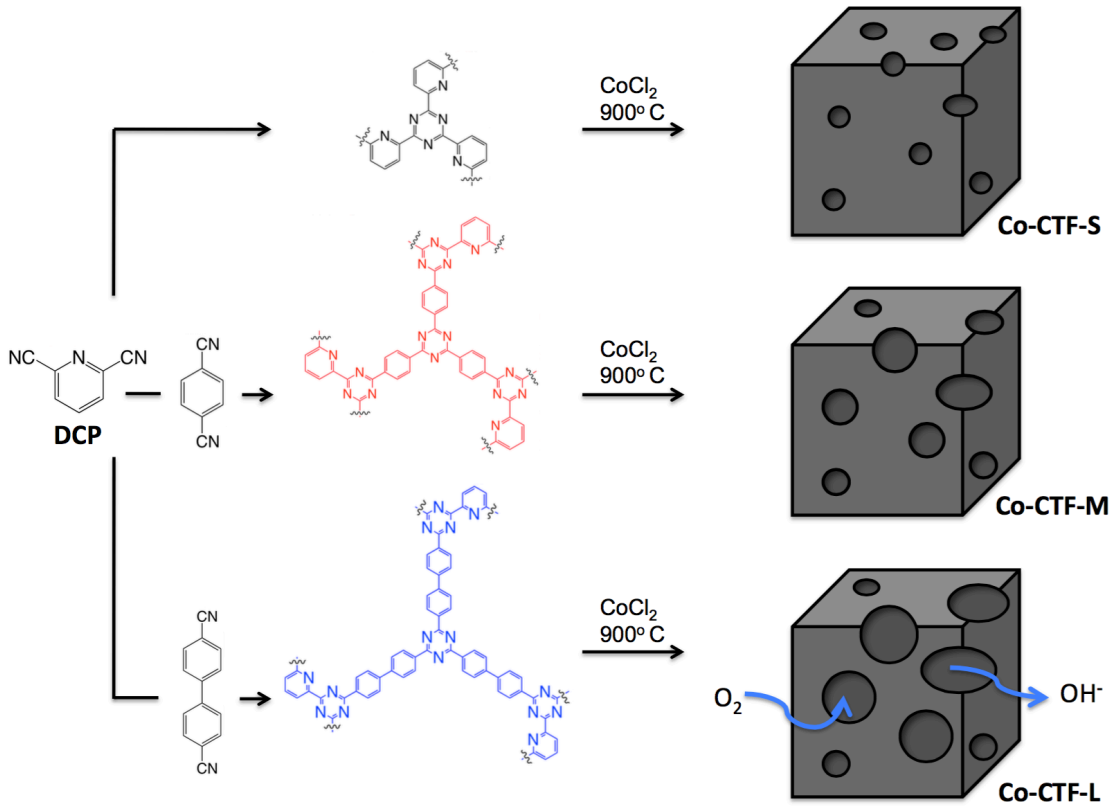

Scheme 5.1. Schematic representation of the synthesis of Co-CTFs with different pore sizes. Our strategy of creating sequentially longer trimered units from the synthesis of CTFs using a single monomer in black, and mixed monomers in red and blue are displayed. The black cubes represent different Co-CTFs and their enhanced pore size.

5.3 Results and Discussion

As shown in Scheme 5.1?, our approach consists of adding long, slim organic linkages to the DCP monomer, therefore increasing length each trimered unit and cobalt chelation sites, hence expanding the pores. We chose DCP as a starting monomer, since its CTF derivatives have shown metal chelations[29], and good electrochemical applications[27,28]. Initially, our CTFs were made through traditional $ZnCl_2$ methods proposed by Kuhn *et al*. and adding mixed monomers when necessary as outlined in Scheme 1. In the mixed ligand scenario, a DCP ratio to DCB or BPDC were mixed 1:2

respectively. After the synthesis at 400 °C, the CTFs were washed using copious amounts of 0.1 M HCl and THF. Cobalt chelation to the CTFs were performed by submerging the material in a $CoCl_2$/ethanol solution (1 mg/mL) for 24 h. A visible de-coloration of the metal solution could be observed, after which the CTFs were washed several times with ethanol to remove any excess non-chelated cobalt. To activate the electrocatalyst, aid in conductivity, and facilitate strong bond formation, the CTFs were annealed at 900 °C for 2 h in a 90:10 (volume ratio) mixture of Ar:H_2 for all samples. The pyrolized materials are noted in relation to their pore size of small (Co-CTF-S), medium (Co-CTF-M), and large (Co-CTF-L). The treatment temperature of 900 °C performs best with our material in terms of ORR, as the case of other works[12].

Pore size evaluations began with using N_2 adsorption techniques for each material. The corresponding surface areas were determined through BET analysis to be 425, 780, 1480 $m^2 g^{-1}$ for our Co-CTF-S, Co-CTF-M, and Co-CTF-L respectively (Figure 5.1a). The isotherm shapes of Co-CTF-M and Co-CTF-L are type-IV, which contains a typical hysteresis loop due to nitrogen fragility artifact during mesopore desorption.

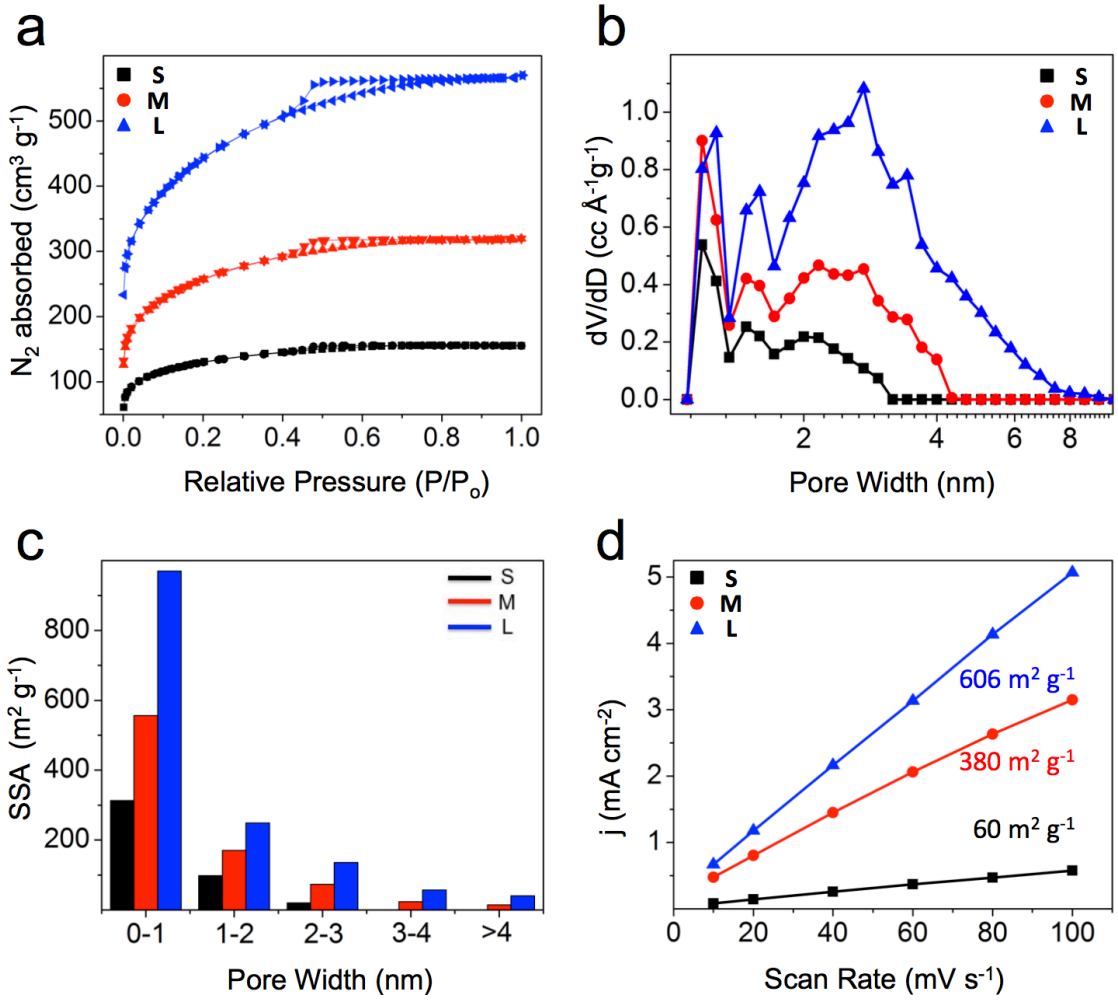

Figure 5.1. Pore size characterization. (a) N_2 BET isotherms. (b) Differential pore volume overlays of Co-CTFs. (c) Bar graph of specific surface areas corresponding to each size pore. (d) Double layer capacitance slope comparisons of Co-CTFs S, M, and L are illustrated in black, red, and blue respectively. Corresponding ECSA calculated and listed according to Co-CTFs.

Although it is important to obtain higher surface areas, expanded pore sizes are also desired and needs to be confirmed. Evidence of actual pore expansion was determined using Density Functional Theory (DFT) methods to calculate specific pore volumes and their corresponding pore widths. As expected, pore size distributions widen with mixed monomeric Co-CTFs as seen in Fig. 5.1b**,** where differential pore volumes of

Co-CTF's S, M, and L are overlaid. Pore widths enlarge from mainly 1-3 nm pores in Co-CTF-S, to ranging in 1-4.5 nm for Co-CTF-M, and finally reaching 1-8 nm distributions in Co-CTF-L. Total pore volumes also rise respectively with pore size from 0.23 $cm^3 g^{-1}$ to 0.40 $cm^3 g^{-1}$ to 0.89 $cm^3 g^{-1}$. The pore specific surface area corresponding to pore widths are displayed in the bar graph of Fig. 5.1c**.** These distributions were derived from cumulative 0ore volume graphs in Figure 5.2.

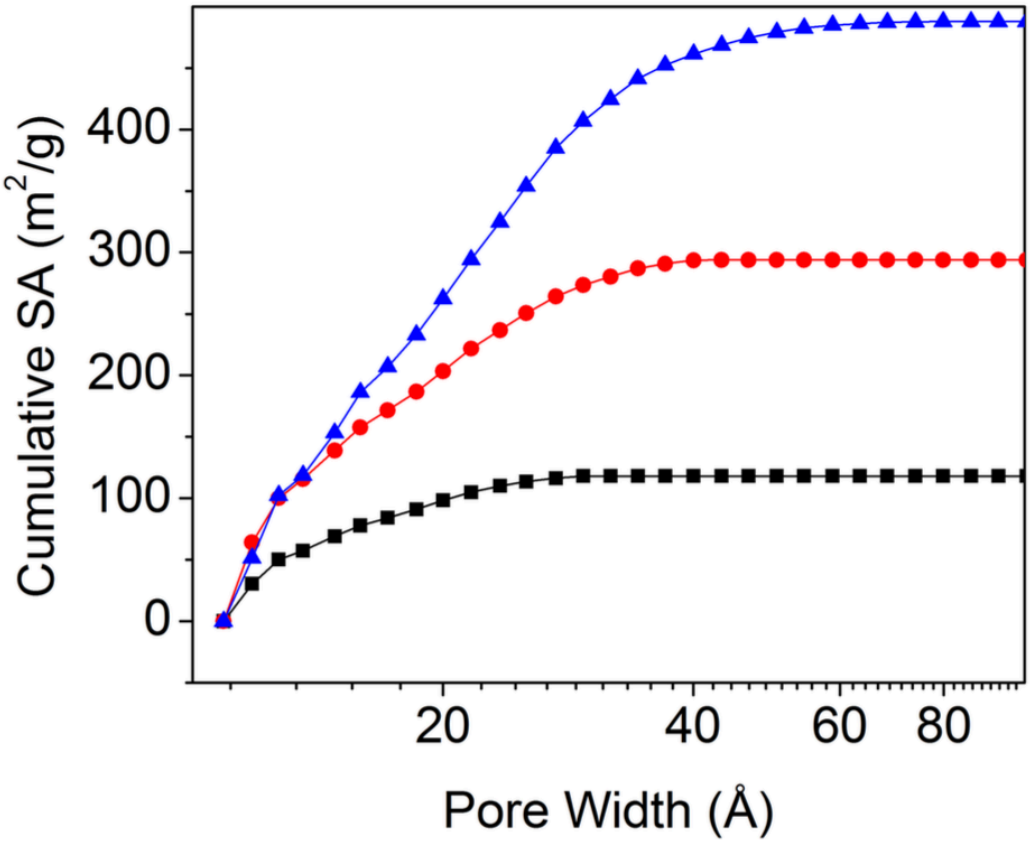

Figure 5.2. Cumulative pore volumes of Co-CTFs S, M, and L, with corresponding colors black, red, and blue respectively.

Since pore accessibility of our 0.1 M KOH electrolyte may differ from N_2 gas diffusions from BET measurements in Co-CTFs, electrochemical surface area (ECSA) calculations were derived from double-layer capacitance (C_{dl}) measurements by sweeping

CV at different rates in a region without Faradaic current (Figure 5.3). The C_{dl} capacitance from CV progress from 5.5 mF cm^{-2}, to 31 mF cm^{-2}, and finally 49 mF cm^{-2} as pores expand, a near 10-fold increase. These C_{dl} measurements translate into specific capacitances of 14 F g^{-1}, 78 F g^{-1}, and 122 F g^{-1} respectively. We can then compute C_{dl} values into ECSA's of 60 m^2 g^{-1}, to 380 m^2 g^{-1}, reaching 606 m^2 g^{-1} respectively, shown in Fig. 5.1d. Our experiments demonstrate not only does pore tuning of Co-CTFs increase surface area, but also C_{dl} and ECSA. These factors play major roles for oxygen reduction by aiding in: reactant delivery, access of surfaces for catalysis, ionic conduction, and product removal from pores.

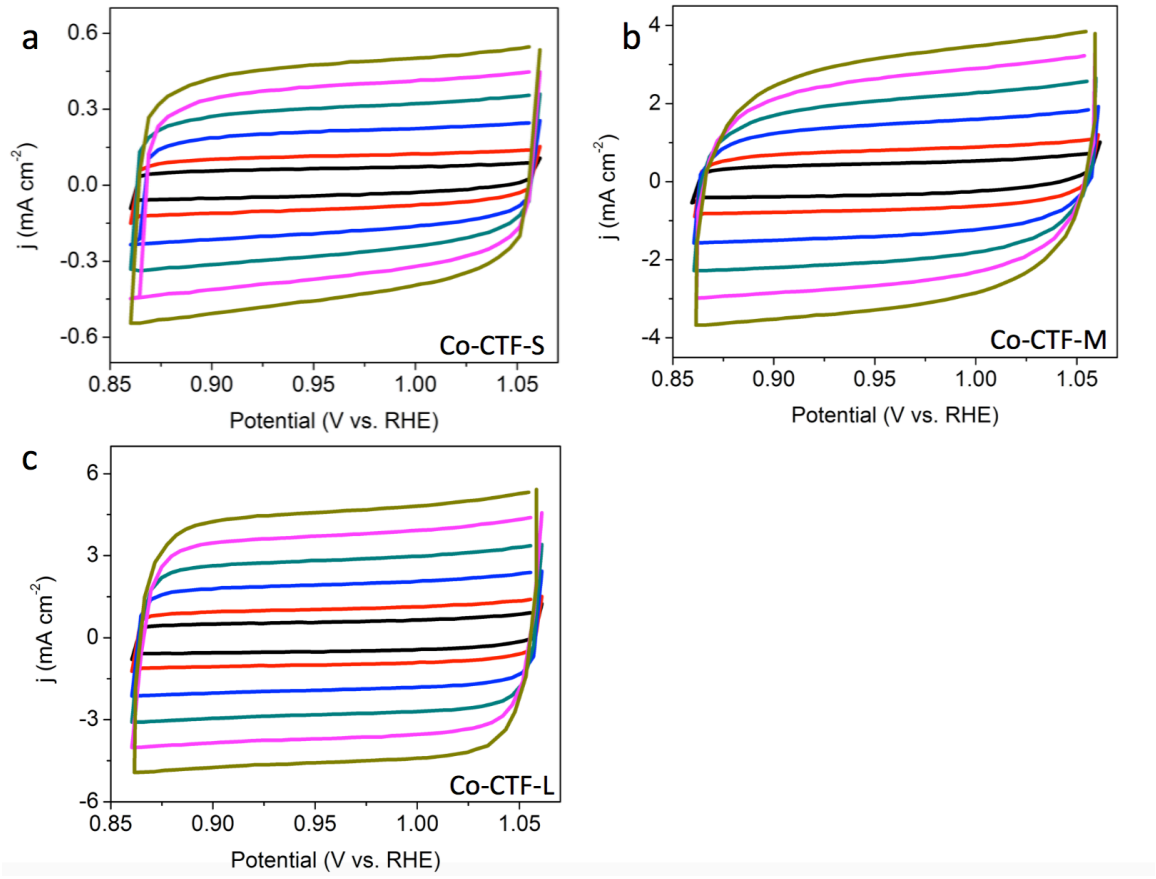

Figure 5.3. Electrochemical surface area CV curves of Co-CTFs S, M, & L in section (a), (b), and (c) respectively.

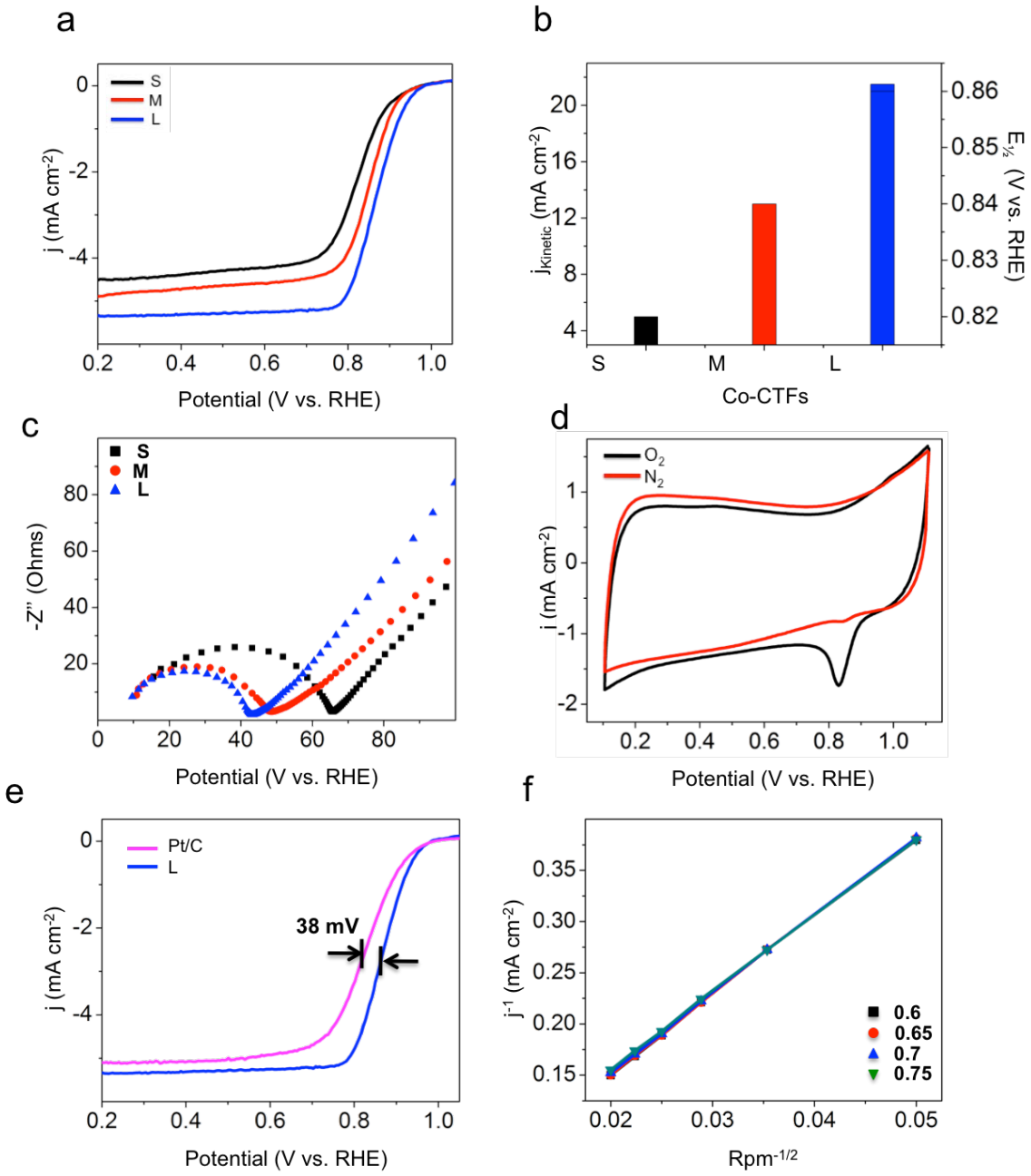

Figure 5.4. Electrochemical Performance. (a) Overlay of the different Co-CTF LSV curves measured at 1600 r.p.m. in 0.1 M KOH. Colors black red and blue indicating pores sizes small (s), medium (m) and large (l) (b) kinetic current density and $E_{1/2}$ on the y-axes, plotted against different pore sizes on the x-axis. (c) Nyquist plot overlays of Co-CTFs. Colors black, red, and blue indicating Co-CTFs of pores sizes small (s), medium (m) and large (l) (d) Representative CV curve of Co-CTF-L under saturated gases N_2 in red or O_2 in blue using 0.1 M KOH electrolyte. (e) Co-CTF-L LSV curve comparison with 20 wt.% Pt/C at 1600 r.p.m. in 0.1 M KOH (f) K-L plot of Co-CTF-L

A strong correlation between ORR activity and pore size of the CTF was observed. Fig. 5.4a overlays the linear scan voltammetry (LSV) curves of our three Co-CTF samples with different pore sizes. As pore size increases, a significant enhancement of both kinetic slope and the diffusion limiting current is achieved. Our calculated Kinetic current densities and $E_{1/2}$ wave potentials are plotted against the respected Co-CTFs in Figure 5.4b. Improving kinetic performance can be attributed to four major ways: decreasing the activation barrier, increasing the temperature, increasing the reactant concentration, and increasing the number of possible reaction sites. Our kinetic improvements can be accredited to the latter two, a greater rate of exchange between reactant and product, and also an increase in accessibility to catalytic sites, both originating from pore size engineering.

In addition to kinetic and diffusion enhancements, we observe progressive charge-transport and ion diffusion which we confirmed using impedance spectroscopy. Nyquist plots displayed in Fig. 5.4c identify the reduced charge-transfer resistance between electrode and electrolyte as pore sizes increase, observed through smaller semi-circle diameters. The improved diffusion efficiency is further confirmed in the shorter 45^{o} Warburg region incline.

A representative CV curve Co-CTF-L is displayed in Fig. 5.4d. Cyclic scans of N_2 saturated KOH solution show the absence of the characteristic ORR cathodic peak. Upon O_2 electrolyte saturation a strong peak at 0.86 V appears. The ORR activity of our Co-CTF-L sample is further compared with the industrial 20 wt% platinum catalyst (Pt/C). As shown in Fig. 5.3b, a steep kinetic slope is induced by the large pore size and results in an impressive $E_{1/2}$ of Co-CTF-L that is 38 mV less than that of Pt/C (0.87 V versus

0.83 V in Fig. 5.4e). Figure 5.4f displays Koutecky-Levich (K-L) plot of Co-CTF-L. The linearity indicates first order rate kinetics, which aligns well with our electron transfer number (n) of 3.98 measured through peroxide current on a rotating ring-disk electrode (RRDE) in Figure 5.5. This is very close in line with commercial Pt/C, which has theoretical *n* of 4.0.

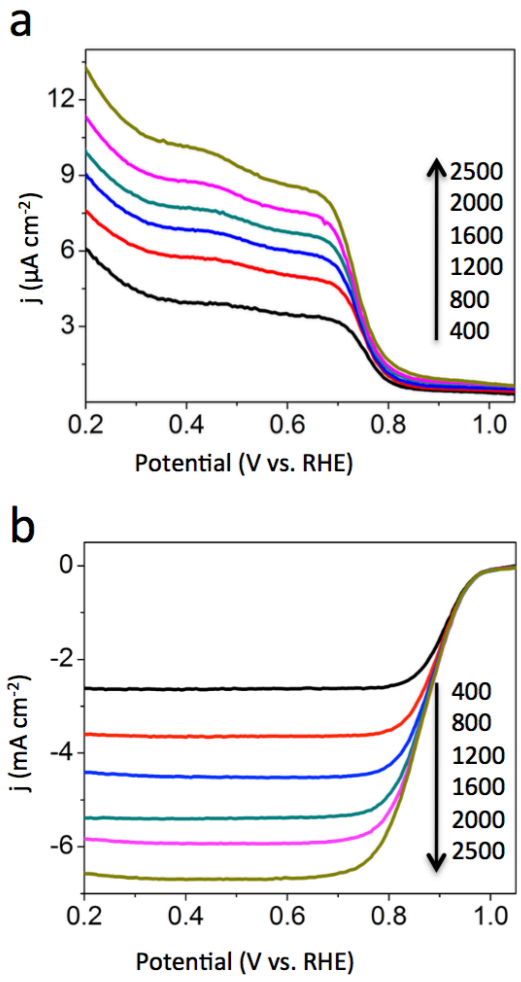

Figure 5.5. Rotating Ring Disk Electrode of Co-CTF-L

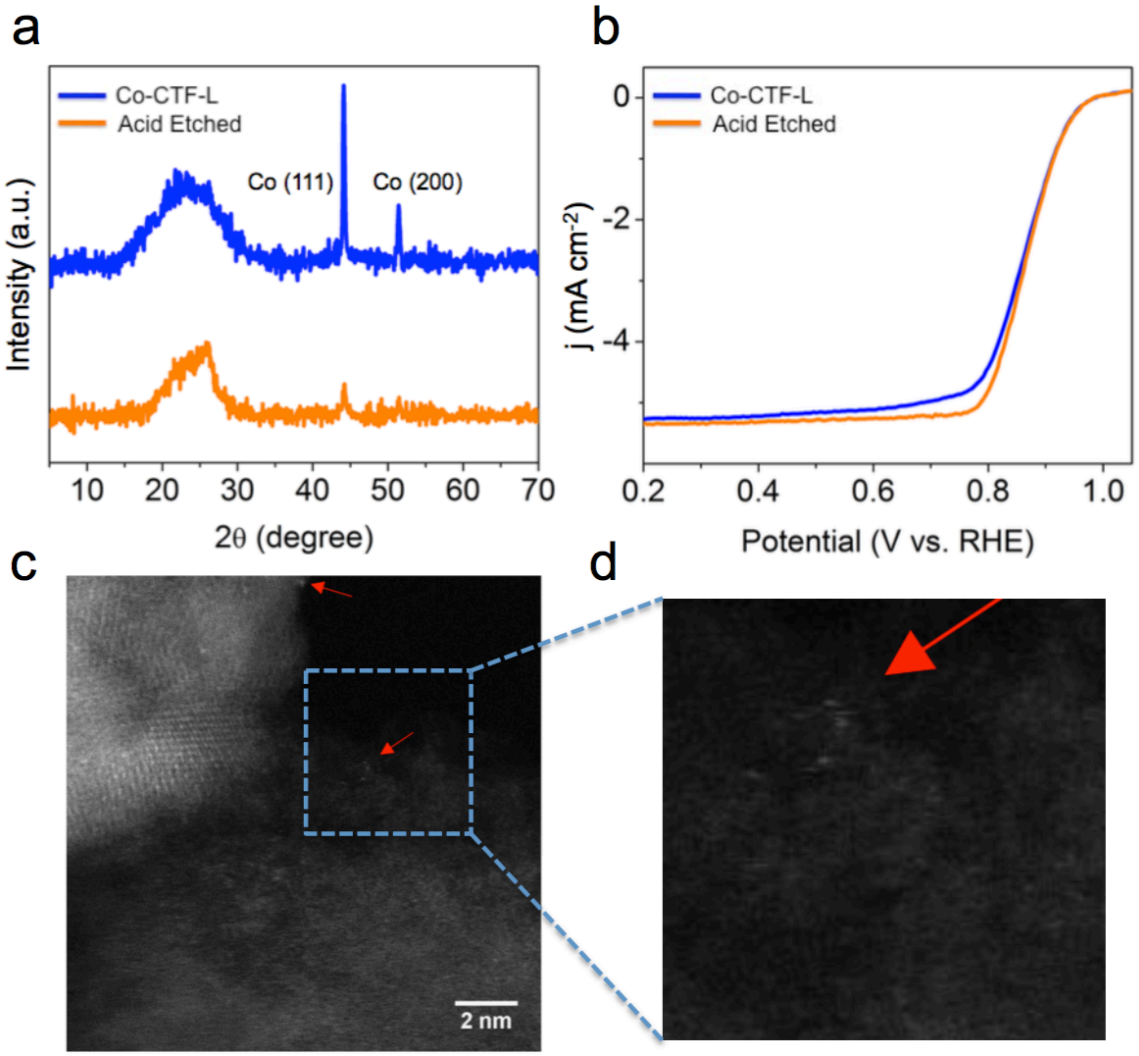

Figure 5.6. Active Catalyst Study. (a) PXRD overlay of Co-CTF-L before and after acid etching. (b) LSV overlay of Co-CTF-L before and after acid etching in 0.1 M KOH electrolyte. Graph colors blue represent Co-CTF-L, and post acid etching of Co-CTF-L in orange for Figures 5.5 (a) and (b).

All Co-CTFs used our study were treated with 0.5 M H_2SO_4 in order to dissolve away most of the large cobalt particles and unstable atoms. Comparing the post acid treated material with PXRD in Fig. 5.6a reveals most of the cobalt has been removed; yet the ORR performance improves. The weak signal signifies the significantly reduced content, and the peak broadness is indicative of small particles. LSV curves measured for the post acid treatment gave a slight improvement in overall performance, resulting in

higher diffusion limiting current especially at ~0.76 V in Fig. 5.3b. These results lead us to believe the active ORR species in our Co-CTFs are not the large particles but likely small clusters and possibly atomic cobalt species similar to what Liang et al[31] found in their acid leaching of cobalt.

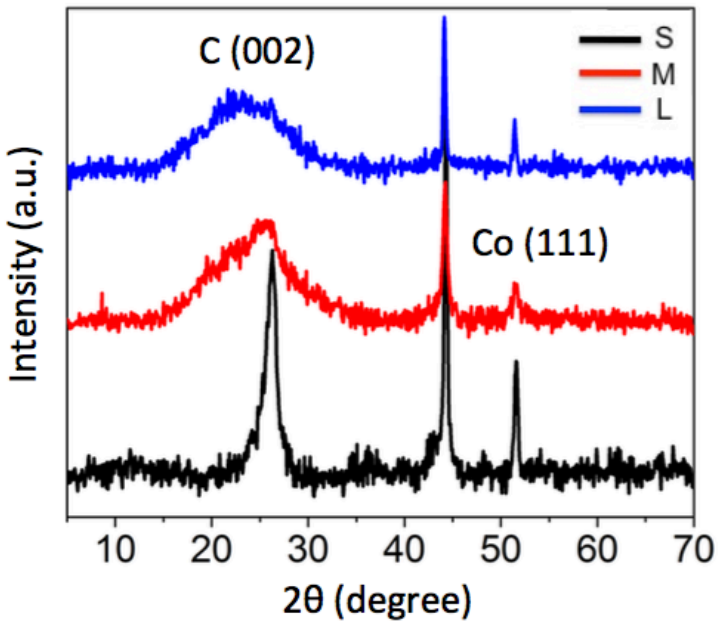

Figure 5.7. – XRD of pre-etched Co-CTFs S, M, & L

Catalyst uniformity throughout our Co-CTFs were confirmed using PXRD and XPS spectroscopy. Figure 5.7 displays the overlapping Co 111 and Co 200 at peak positions at 44.3° and 51.5° from pre-etched Co-CTFs samples. Nitrogen XPS spectroscopy (Figure 5.8) displays only pyridinic (398.6 eV) and pyrrolyic (400.5 eV) bands throughout all three Co-CTFs, which are the two types of ORR active nitrogens[30].

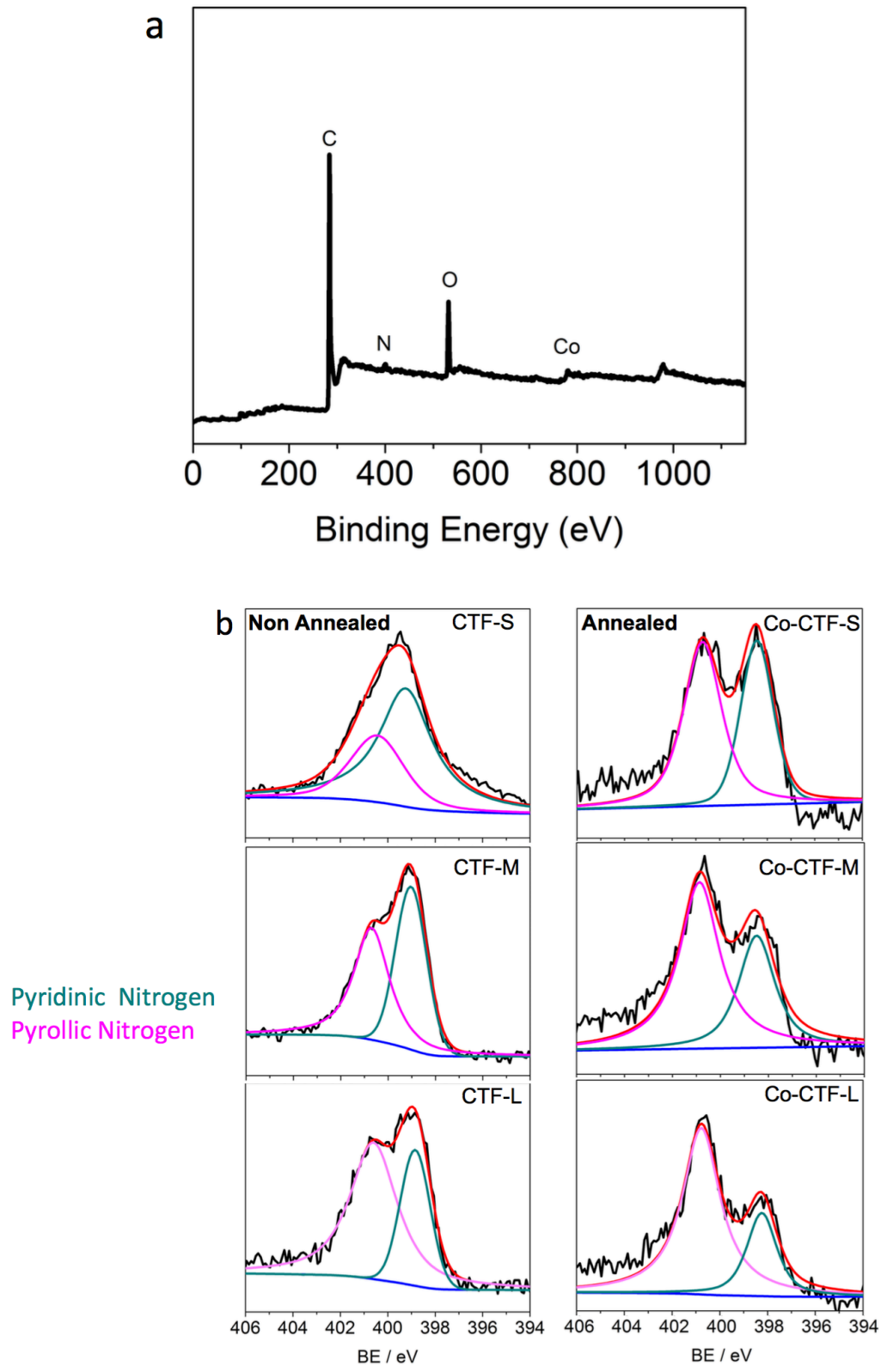

Figure 5.8. – XPS Data of Survey (a), and Nitrogen N1s of Co-CTF-L in (b).

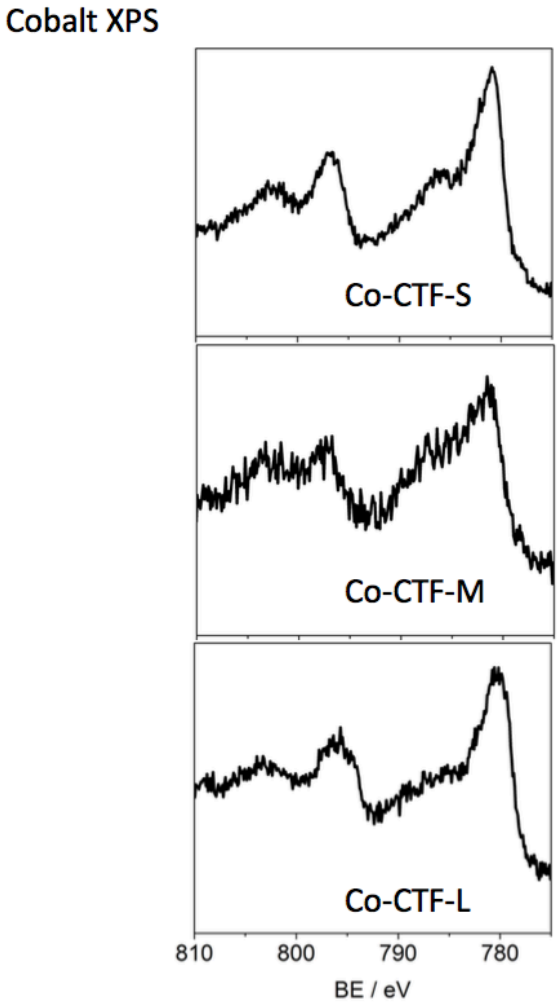

Figure 5.9 – XPS Spectrum of Cobalt 2P of Co-CTF-L

Cobalt 2p spectrums in Figure 5.9. designate uniform bands at 781.1 and 796.2 eV corresponding to Co $2p_{3/2}$ and Co $2p_{1/2}$, for all three Co-CTFs. The 15.1 eV separation, along with satellite peaks indicates the presences of cobalt ion species[32]. The non-observance of cobalt metal may be attributed to the limiting sampling depth of XPS. At the moment, the specific form of cobalt in ORR catalyst is unknown, whether its large particles, small clusters, or single atoms. Though many speculate that in transition-metal-

nitrogen-carbon systems the main contribution in electrochemistry comes from small clusters and single atoms, which is the case for iron-nitrogen-carbon ORR catalysts[33].

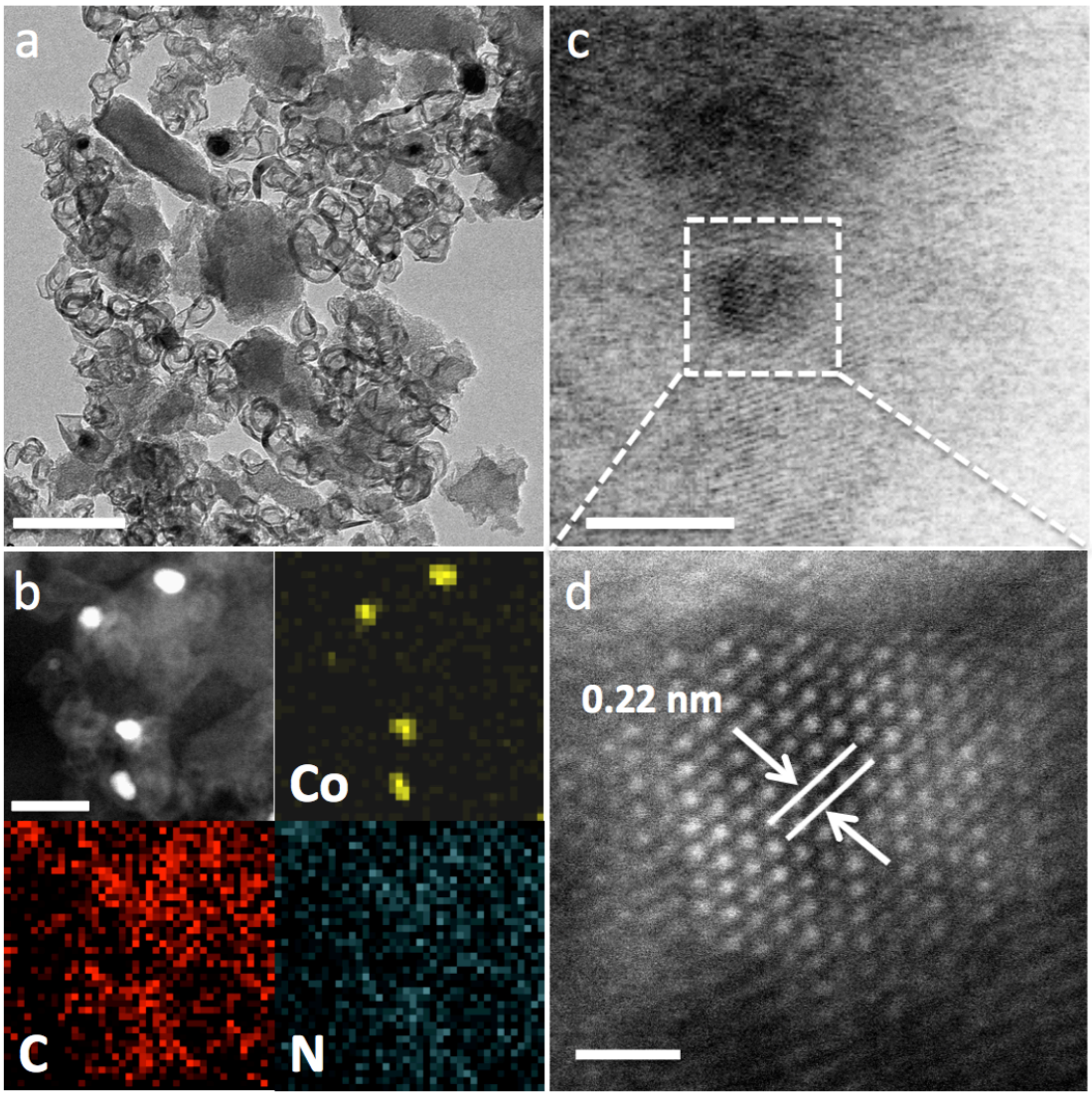

Figure 5.10. Electron imaging of Co-CTF-L. (a) Low magnification TEM. (b) EDX mapping of Co-CTF-L. (c) HAADF-STEM low magnification of Co-CTF-L. (d) HAADF-STEM high magnification of Co-CTF-L. Scale bars are 200 nm (a), 100 nm (b), 5 nm (c), 1 nm (d).

Low magnification transmission electron microscopy (TEM) in Figure 5.10 displays the presence of graphitic ribbons, amongst the CTF, along with remaining cobalt particles that were not etched away. Elemental maps of carbon, nitrogen, and cobalt were

obtained through energy dispersive X-ray (EDS) technique under HRTEM, shown in Supplementary Fig. 5.7b. To investigate the presence of smaller clusters and possible single atoms we employed an aberration corrected High Angle Annular Dark Field Scanning Transmission Electron Microscopy (HAADF-STEM) under dark field imaging. We captured an atomic resolution image of a sub 5 nm cobalt particle in Figure 10. The highly crystalline Co^0 particles are confirmed by (111) facet with d-spacing of 2.2 Å, which correlates well with our PXRD in Fig. 5.2d. It should be noted that a low accelerating voltage of 80 kV was used avoid electro-beam induced damage of the CTF and clusters[33,35].

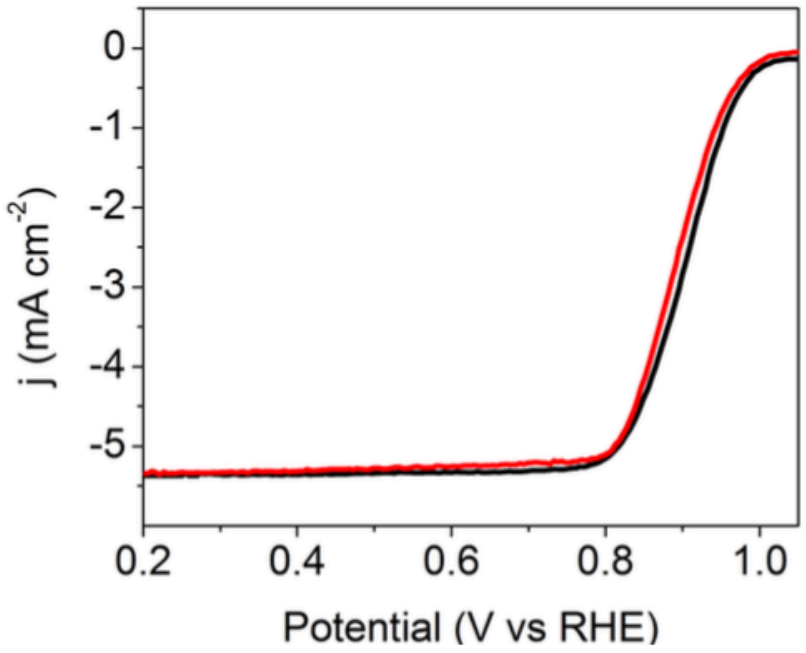

Figure 5.11. Stability LSV of Co-CTF-L with initial sweet in black, and post 10,000 cycles in red.

The durability of Co-CTF-L was tested by using CV cycling tests for 10,000 cycles in ranges 0.4-1.2 V. LSV curves of initial and post 10,000 cycles show only slight

decay of ~ 12 mVs at $E_{½}$ wave in Figure 5.11. Through this, the kinetic slope in the post 10,000 cycles LSV curve remains unchanged.

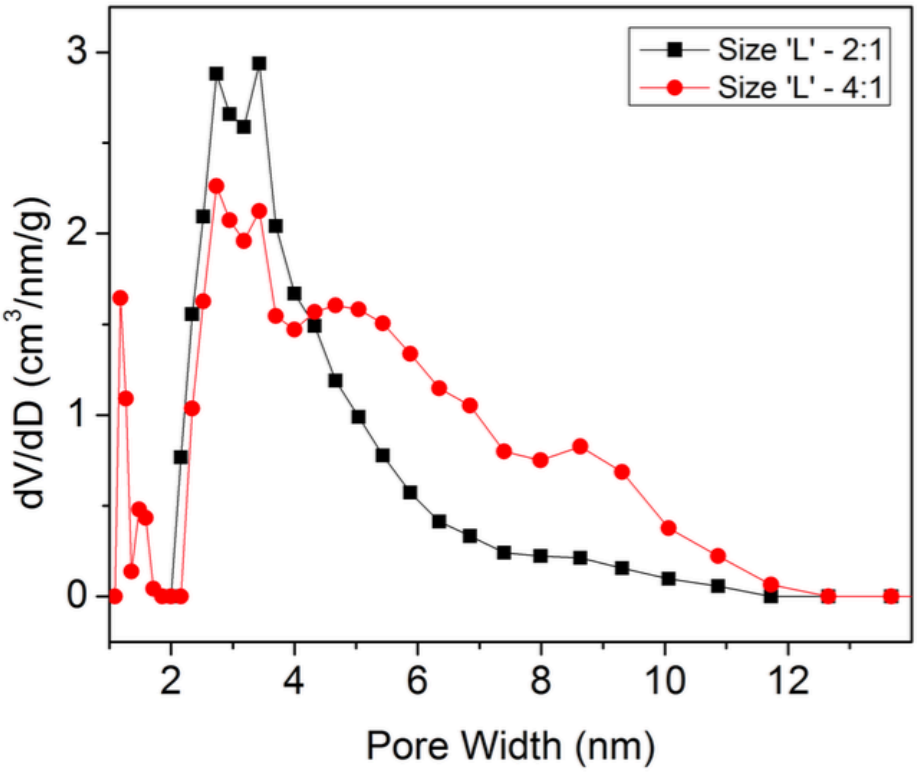

Figure 5.12. Measuring the DFT calculated differential pore volume of varied stoichiometric ratios between CTF-L starting monomers.

We investigate our molecular tuning strategy by changing the ratios of blended monomers. Here, we observed that increasing the amount of BPDC, a longer linker than DCP, results in the pore stretching. The cavity opening is mainly prevelant in the 5-12 nm range as observed from the differential volume graph of Figure 5.12. A slight reduction in pore volume between 2 to 5 nm is also measured. These observations are congruent with our previous claims.

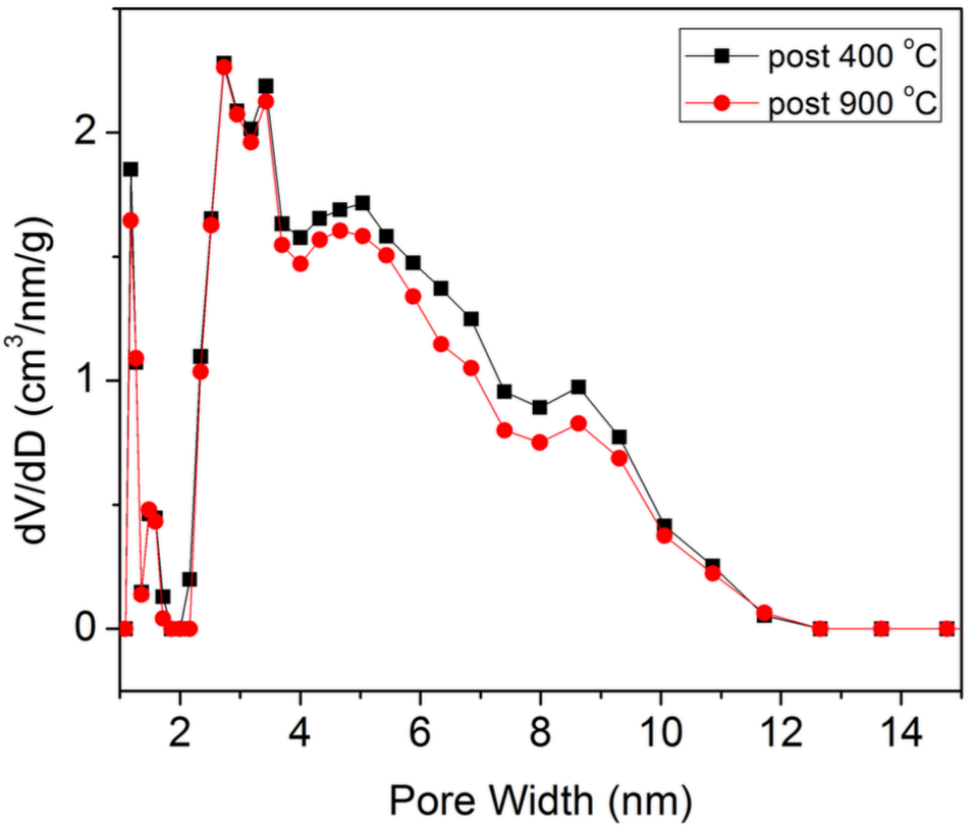

Figure 5.13 DFT Differential pore volume measurements of the same sample, CTF-L, after 400 °C sublimation, and 900 °C annealing.

To further confirm the high temperature stability and structural integrity of CTFs under thermal annealing, we measured differential volumes of CTF-L at both 400 °C sublimation, and 900 °C annealing, as shown in Figure 5.13. Near no changes were observed between the two samples. The very slight variation is most likely attributed to the normal float that is present in BET sample measurement. Here we can confirm that thermal annealing even at temperatures as high as 900 °C does not change the structure of CTFs.

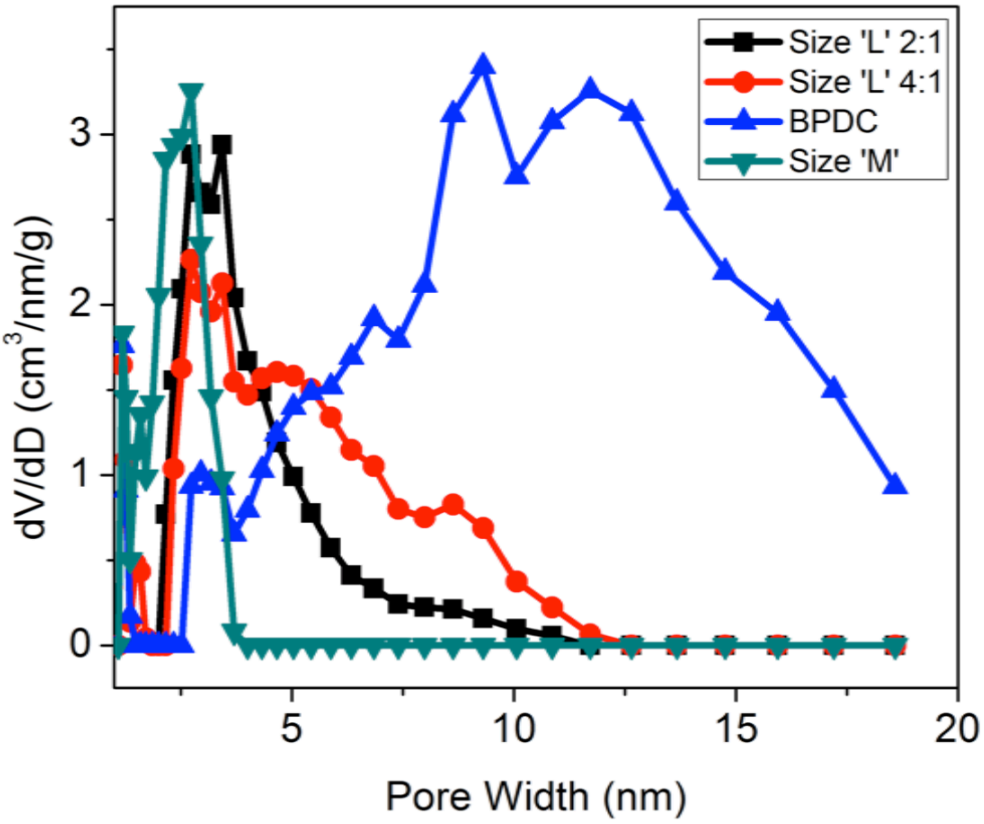

Figure 5.14 Additional molecular tuning pore size measurements using DFT calculations from BET measurements.

As we move towards a full series of expansions, we see our theory hold true for several more materials. Figure 5.14 displays the DFT differential pore volume distributions of 4 different CTFs, from size 'M', along with varied stoichiometric ratios of size 'L' and lastly BPDC. The incremental pore expansion holds true for all 4 compounds. BPDC being the longest monomer, and when solely as the starting material, produces a highly mesoporous CTF.

5.4 Conclusion

The effects of pore size tuning and pore volume on electrochemical performances of using cobalt-containing CTFs as precursors have been systematically investigated in this work. Increased surface area, larger pore volumes, and higher ECSAs improve reactivity and diffusion for oxygen-saturated electrolytes. Moreover, increased charge-transfer and enhanced diffusion are achieved. To summarize, we developed a concept to help maximize the efficiency our Co-CTF catalyst. We believe our pore expansion concept may be applicable to many future electrocatalyst designs.

5.5 References

1. Sawin, Janet. J., Sverrisson, F., Rickerson, W. Renewables global status report (REN21 2015).
2. Bertuccioli, L. *et al.* Development of water electrolysis in the european union. 1–160 (2014).
3. Jasinski, R. A new fuel cell cathode catalyst. *Nature* **201,** 1212–1213 (1964).
4. Jasinski, R. Cobalt phthalocyanine as a fuel cell cathode. *J. Electrochem. Soc.* **112,** 526 (1965).
5. Liang, Y. *et al.* Oxygen reduction electrocatalyst based on strongly coupled cobalt oxide nanocrystals and carbon nanotubes. *J. Am. Chem. Soc.* **134,** 15849-15857 (2012).
6. He, Q. *et al.* High-loading cobalt oxide coupled with nitrogen-doped graphene for oxygen reduction in anion-exchange-membrane alkaline fuel cells. *J. Phys. Chem. C* **117,** 8697–8707 (2013).
7. Guo, S., Zhang, S., Wu, L. & Sun, S. Co/CoO nanoparticles assembled on graphene for electrochemical reduction of oxygen. *Angew. Chem. Int. Ed.* **51,** 11770–11773 (2012).
8. Mao, S., Wen, Z., Huang, T., Hou, Y. & Chen, J. High-performance bi-functional electrocatalysts of 3D crumpled graphene-cobalt oxide nanohybrids for oxygen reduction and evolution reactions. *Energy Environ. Sci.* **7,** 609–616 (2014).
9. Fan, X. *et al.* M3C (M : Fe , Co , Ni) Nanocrystals encased in graphene nanoribbons : An active and stable bifunctional electrocatalyst for oxygen reduction and hydrogen evolution reactions. *ACS Nano* **9,** 7407–7418 (2015).
10. Wu, G., More, K. L., Johnston, C. M. & Zelenay, P. High performance electrocatalysts. *Science* **332,** 443-448 (2011).
11. Liang, Y. *et al.* Co3O4 Nanocrystals on graphene as a synergistic catalyst for oxygen reduction reaction. *Nat. Mater.* **10,** 780-786 (2011).
12. Fei, H. *et al.* Cobalt nanoparticles embedded in nitrogen-doped carbon for the hydrogen evolution reaction. *ACS Appl. Mater. Interfaces* **7,** 8083-8087 (2015).
13. Xia, B. Y. *et al.* A metal–organic framework-derived bifunctional oxygen electrocatalyst. *Nat. Energy* **1,** 15006 (2016).
14. Zhuang, Z. *et al.* Nickel supported on nitrogen-doped carbon nanotubes as hydrogen oxidation reaction catalyst in alkaline electrolyte. *Nat. Commun.* **7,** 10141 (2016).
15. Strickland, K. *et al.* Highly active oxygen reduction non-platinum group metal electrocatalyst without direct metal–nitrogen coordination. *Nat. Commun.* **6,** 7343 (2015).
16. Kuhn, P., Antonietti, M. & Thomas, A. Porous, covalent triazine-based frameworks prepared by ionothermal synthesis. *Angew. Chem. Int. Ed.* **47,** 3450–3453 (2008).

17. Ren, S. *et al.* Porous, fluorescent, covalent triazine-based frameworks via room-temperature and microwave-assisted synthesis. *Adv. Mater.* **24,** 2357–2361 (2012).

18. Bhunia, A., Vasylyeva, V. & Janiak, C. From a supramolecular tetranitrile to a porous covalent triazine-based framework with high gas uptake capacities. *Chem. Commun.* **49,** 3961–3 (2013)

19. Zhao, Y., Yao, K. X., Teng, B., Zhang, T. & Han, Y. A perfluorinated covalent triazine-based framework for highly selective and water–tolerant CO2 capture. *Energy Environ. Sci.* **6,** 3684 (2013).

20. Chan-Thaw, C. E. *et al.* Covalent triazine framework as catalytic support for liquid phase reaction. *Nano Lett.* **10,** 537–541 (2010).

21. Roeser, J., Kailasam, K. & Thomas, A. Covalent triazine frameworks as heterogeneous catalysts for the synthesis of cyclic and linear carbonates from carbon dioxide and epoxides. *ChemSusChem* **5,** 1793–1799 (2012).

22. Chan-Thaw, C. E., Villa, A., Prati, L. & Thomas, A. Triazine-based polymers as nanostructured supports for the liquid-phase oxidation of alcohols. *Chem. Eur. J.* **17,** 1052–1057 (2011).

23. Sakaushi, K. *et al.* An energy storage principle using bipolar porous polymeric frameworks. *Angew. Chemie - Int. Ed.* **51,** 7850–7854 (2012).

24. Liao, H., Ding, H., Li, B., Ai, X. & Wang, C. Covalent-organic frameworks: potential host materials for sulfur impregnation in lithium–sulfur batteries. *J. Mater. Chem.* **2,** 8854-8858 (2014).

25. Sakaushi, K. *et al.* Aromatic porous-honeycomb electrodes for a sodium-organic energy storage device. *Nat. Commun.* **4,** 1485 (2013).

26. Hao, L. *et al.* Bottom-up construction of triazine-based frameworks as metal-free electrocatalysts for oxygen reduction reaction. *Adv. Mater.* **27,** 3190–3195 (2015).

27. Iwase, K., Yoshioka, T., Nakanishi, S., Hashimoto, K. & Kamiya, K. Copper-modified covalent triazine frameworks as non-noble metal electrocatalysts for oxygen oeduction. *Angew. Chem. Int. Ed.* **54,** 11068–11072 (2015).

28. Kamiya, K., Kamai, R., Hashimoto, K. & Nakanishi, S. Platinum-modified covalent triazine frameworks hybridized with carbon nanoparticles as methanol-tolerant oxygen reduction electrocatalysts. *Nat. Commun.* **5,** 5040 (2014).

29. Palkovits, R., Antonietti, M., Kuhn, P., Thomas, A. & Schuth, F. Solid catalysts for the selective low-temperature oxidation of methane to methanol. *Angew. Chem. Int. Ed.* **48,** 6909–6912 (2009).

30. Ding, W. *et al.* Space-confinement-induced synthesis of pyridinic- and pyrrolic-nitrogen- doped graphene for the catalysis of oxygen reduction. *Angew. Chem. Int. Ed.* **52,** 11755–11759 (2013).

31. Liang, H. W. *et al.* Molecular metal–N_x centres in porous carbon for electrocatalytic hydrogen evolution. *Nat. Commun.* **6,** 7992 (2015)

32. Andreiadis, E. S. *et al.* Molecular engineering of a cobalt-based under fully aqueous conditions. *Nat. Chem.* **5,** 48 (2013).

33. Zitolo, A. *et al.* Identification of catalytic sites for oxygen reduction in iron- and nitrogen-doped graphene materials. *Nat. Mater.* **14,** 937–42 (2015).

34. Krivanek, O. L. *et al.* Atom-by-atom structural and chemical analysis by annular dark-field electron microscopy. *Nature* **464,** 571–574 (2010).

35. Zhang, X. *et al.* Catalytically active single-atom niobium in graphitic layers. *Nat. Commun.* **4,** 1924 (2013).

Concluding Remarks

Porous materials have a number of practical applications in a variety of fields. Activated carbons are present in all types of filtration processes, extractions, metal purifications, gas masks, and fuel cells. Zeolites are present in many household products such as detergents. MOFs and COFs have brought a whole new degree of order to porous materials. These benefits can be exploited greatly with separations, which account for a large cost of many industrial chemicals. The ability to tune these materials allows a great degree of control to tailor for applications such as those mentioned in this dissertation and beyond. The work here with CTFs was meant to bring scientific advancement of these interesting materials as well as explore potential applications.

The work with N-Heterocyclic Carbene CTFs shows how important and reactive ligands for organometallic chemistry can be built into solid frameworks. This is powerful in the sense of creating heterogenous catalysts. Moreover, the ionic solids were applied to CO_2 capture. We build a stronger foundation and information onto how to better advance and progress through creating organic solids to fit the needs of applications in gas capture and catalyst immobilization. Showing we can tune the reactive sites on CTFs is something not easily performed on activated carbons or zeolites, especially if you at trying tune with particular ligands.

We are not far from seeing an explosion of new porous, crystalline, conducting MOF or COF crystals. Right now only a few exist, and clever chemists are working each day into producing many more of these remarkable gems. Exfoliation of the 2D CTFs helped explore the future possibilities and bring light into how create materials suitable for devices.

Electrocatalysis is becoming ever more important to clean energy. Water splitting and water recombination being one of the cleanest and easiest ways for energy storage due to the recyclability and ubiquity of water. Moreover if we could someday split ocean water with low overpotentials, the recombination of H_2 gas would produce potable water, a 2-for-1 as you could say. CTFs prove to be a very advanced material for these applications. The major upsides being how robust they are to the thermal, reducing, and oxidizing atmospheres at which this catalysis takes place. I have shown how tunable they are, with the NHC-Carbene as well. The most interesting factor as I discovered late in my graduate career, is how well they uphold their structures at high temperatures. The ability to finely control the pore size of activated carbons has been elusive to this day. This approach brings a certain amount of order to materials, which are traditionally disordered.

The influence of pore size on electrochemistry is very significant. We are beginning to see that it is not the catalyst that is possibly slow, but delivery of reactants to the catalyst to be a major limiting factor as well. Many catalyst such at the cobalt based ones present in this work, can be significantly enhanced so long as ample mass transfer is available. I'd like to see this key parameter be further exploited in the future. Our understanding of this technology is still in the early stages and it would be great to see this aid industry of fuel cell technology. Hopefully pore control is not limited to fuel cells. Super capacitors are heavily reliant on optimal pore size, surface area, surface volume, and conductivity. I hope to see this work extend into finding the optimal pore confirmation for a vast variety of applications.